SEDIMENT SHEAR Q FROM HORIZONTAL COMPONENT AIRGUN OBS DATA

A DISSERTATION SUBMITTED TO THE GRADUATE DIVISION OF THE UNIVERSITY OF HAWAII IN PARTIAL FULFILLMENT OF THE REQUIREMENTS FOR THE DEGREE OF

DOCTOR OF PHILOSOPHY

IN

GEOLOGY AND GEOPHYSICS

DECEMBER 1993

By

Peter D. Bromirski

Dissertation Committee:

L. Neil Frazer, Chairperson
Eduard Berg
Frederick K. Duennebier
Roy H. Wilkens
Eric Firing

We certify that we have read this dissertation and that, in our opinion, it is satisfactory in scope and quality as a dissertation for the degree of Doctor of Philosophy in Geology and Geophysics.

DISSERTATION COMMITTEE

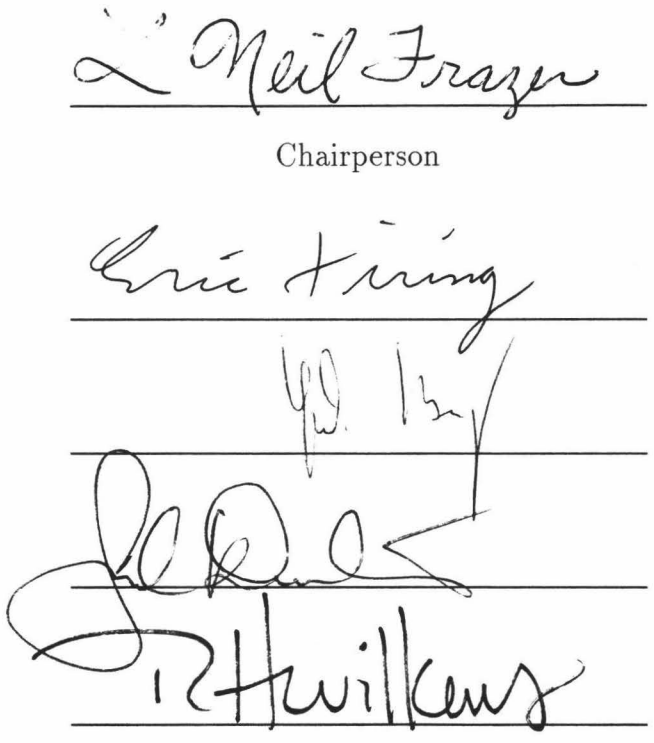

Chairperson

ACKNOWLEDGMENTS

My committee chairman, Neil Frazer, was always ready to to help with useful advice, explanations, and suggestions, and Neil taught me to be thorough in all my analyses. The work that resulted is strongly influenced by his theoretical perspective.

Fred Duennebier collected the OBS data that motivated much of this work, and also helped significantly with information and entertaining discussions about the data.

Ed Berg gave me the basics of seismology in great detail, serving as a solid basis from which to expand my understanding.

Discussions with Roy Wilkins improved my general understanding of marine sediments.

Eric Firing provided an oceanographic perspective.

I thank my committee members for all their help and advice.

Subhashis Mallick let me use his computer program for seismic modeling and helped me get started in the wonderful world of synthetic seismogram computing. Joe Dellinger was always there after dark when help was needed with arcane computerese.

Thanks also go to Gerard Fryer for helpful discussions on crustal structure.

And thanks to the many people in the SOEST community that either helped or made my time here a little more interesting, especially the other Seismology grad students and associates.

And last but definitely not least, I want to thank Ursula who put up

with the madness that goes along with getting a Ph.D., especially the last few weeks when the insanity from finishing a paper and defending reached new heights.

ABSTRACT

In this dissertation, I estimate the effective sediment shear-wave quality factor, Q_β, from *PS* and *PSSS* basement converted shear-wave reflections. I use airgun horizontal component ocean bottom seismometer (OBS) data collected over 356 m of primarily high-porosity biosiliceous clay in 5467 m of water in the northwest Pacific at $43°55.44'N$, $159°47.84'E$ (DSDP Site 581) (Duennebier et al., 1987) to estimate Q_β.

Direct measurement of the sediment shear-wave quality factor, Q_β, has been hindered by the lack of an effective shear-wave source. I show that if a satisfactory horizontal component OBS is available, then sediment Q_β can be determined directly by using spectral ratios of converted shear-wave reflections. Spectral ratios are formed with the *PS* reflection from the sediment/basement interface and the *PSSS* multi-bounce sediment shear-wave reflection. As a check, I also computed Q_β from the peak amplitudes of *PS* and *PSSS*.

To evaluate the reliability of the Q_β estimate, I tested the spectral ratio method on synthetic seismograms that model the OBS data. Core logs from a nearby borehole were used to constrain the sediment thickness and density, while the OBS data constrains the sediment and basement velocity structure for the models used to generate the synthetic seismograms. Tests show that the spectral ratio method is reliable in the presence of moderate amounts of noise, signal clipping, and scattering from cyclic layering. Effective Q_β for the sediment column was found to be 97 ± 11 ($\alpha = 0.281 \pm 0.032$ dB/λ) in the frequency band 3-18 Hz.

To increase confidence in a Q estimate, more than one method should be applied to the same arrivals. A new method to estimate Q from two arrivals of the same signal, called the Q–gram method, is presented. In

this application of the Q–gram method, I use a new definition of pulse width applicable to oscillatory arrivals to measure the propagation loss. The propagation loss is defined as the change in the pulse width divided by the difference in traveltime between the arrivals. An average of either the instantaneous frequency or instantaneous pulse width over the duration of the arrival is used as the definition of pulse width. The *PS* arrival serves as the reference wavelet. The Q–gram method is based on propagating the reference wavelet with a plane-wave Q–propagator for various values of Q^{-1}. The Q–propagator includes a dispersion relation and the measured difference in traveltime between the data arrivals. The plot of synthetic propagation loss between the reference and propagated wavelets, versus Q^{-1}, is called a Q–gram. The Q-gram, together with the measured propagation loss of the data, gives the Q of the data.

The Q–gram method is found to be robust in the presence of moderate amounts of noise and signal clipping by tests on synthetic seismograms that model the OBS data. The OBS data indicate that effective sediment Q_β is 75 ± 15. Application of the spectral ratio method using shortened windows that exclude interfering arrivals identified by means of the instantaneous frequency gives a similar estimate of sediment Q_β.

TABLE OF CONTENTS

TABLE OF CONTENTS

TABLE OF CONTENTS

LIST OF TABLES

LIST OF FIGURES

LIST OF FIGURES

LIST OF FIGURES

Chapter 1

SHEAR-WAVE ATTENUATION IN MARINE SEDIMENTS: AN INTRODUCTION

1.1 ATTENUATION OF SEISMIC WAVES IN MARINE SEDIMENTS

Anelasticity in earth materials results in the attenuation and dispersion of seismic waves. Attenuation, characterized by the dimensionless intrinsic quality factor Q, causes a propagating wavelet to broaden and decrease in amplitude. When corrected for geometric spreading and reflection coefficients, seismic waves decay in amplitude like $e^{-\alpha x}$ in which x is the source-receiver distance and α is the attenuation. Attenuation is thus an intrinsic property of the material through which the waves propagate. Attenuation measured from field data, however, includes both intrinsic losses due to anelasticity and apparent losses resulting from scattering.

The determination of the attenuation characteristics of seismic waves in marine sediments has been the focus of numerous studies (e.g. Hamilton, 1976a, 1976b; Jacobson et al., 1981; Jensen and Schmidt, 1986). Stratification within the sediments may result in significant scattered energy and associated interference of seismic signals that can make attenuation measurements extremely difficult.

The effect of sediment shear-wave parameters on acoustic propagation loss in the ocean has been examined by Vidmar (1980a,b), Harrison and Cousins (1985), and Hughes et al. (1990). Sediment attenuation can be useful in identifying sediment type (Hamilton, 1980), and changes in attenuation with depth can indicate the degree of lithification (Hamilton, 1976a; Jacobson et al., 1981). Reflectivity modeling of the oceanic crust can give erroneous results for crustal shear-wave Q if incorrect assumptions are made about Q_β, the effective shear-wave Q of the sediments.

Although the shear-wave properties of ocean sediments can be determined using Scholte-waves (Jensen and Schmidt, 1986), numerical modeling shows that Scholte-waves propagate only in the topmost portion of the sediments. For shallow water sediments, Jensen and Schmidt found a relatively steep gradient in both shear-wave velocity, c_β, and Q_β between the sea floor and 60 m depth.

Direct measurement of sediment Q_β has been limited by the absence of high quality sediment shear-wave data. This is due largely to the lack of satisfactory ocean bottom S-wave sources, but is also related to problems in ocean bottom seismometer (OBS) design (Sutton and Duennebier, 1987). In this dissertation, the source problem is circumvented by analyzing converted shear-wave reflections from the top of the crust (basement) recorded by an OBS. The airgun horizontal component OBS data were collected over 356 m of primarily high-porosity biosiliceous clay in 5467 m of water in the northwest Pacific at $43°55.44'N$, $159°47.84'E$ (DSDP Site 581) (Duennebier et al., 1987). The detection and identification of multiply-reflected basement-converted shear-waves allows the first direct measurement of effective Q_β for the entire sediment column at a deep water site.

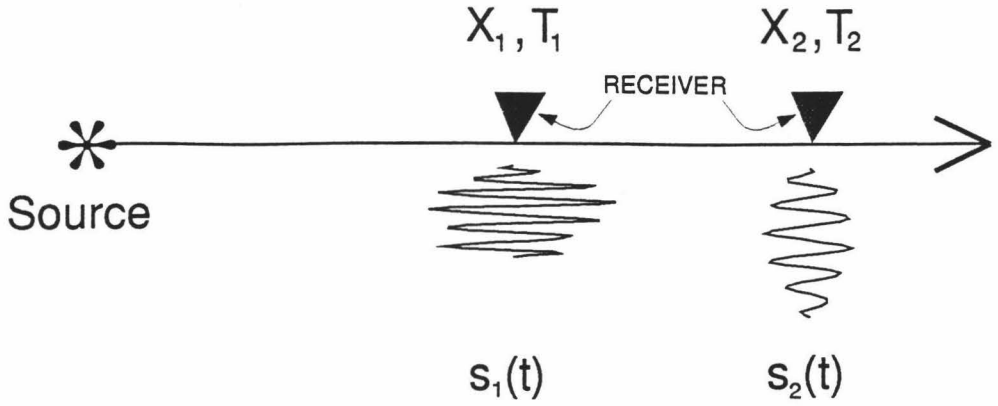

Figure 1.1: Schematic showing plane wave source–receiver relationship. The change in the signal between X_1 and X_2 is used to estimate Q.

1.2 MEASURING ATTENUATION: ESTIMATING Q

To estimate Q from data, a change in amplitude, spectral content, or pulse width must be measured between two arrivals of the same seismic signal. The magnitudes of the change in these signal attributes depend on traveltime, path characteristics (including scattering), and intrinsic Q. As Q increases, the change in a signal attribute for a particular path decreases. To estimate Q, definitions of the traveltime and the signal attribute to measure the propagation loss must be chosen.

As Fig. 1.1 shows schematically, a signal propagating away from a source is recorded by receivers at locations X_1 and X_2 with associated arrival times T_1 and T_2, respectively. In the frequency domain, the signal at X_2, $s_2(t)$, can be represented in terms of the signal at X_1, $s_1(t)$, by

$$S_2(\omega) \;=\; e^{i\omega\Delta X/c}\; e^{-\alpha\Delta X}\; S_1(\omega) \qquad (1)$$

where $\Delta X = X_2 - X_1$, c is the seismic wave speed, and $S_1(\omega)$ and $S_2(\omega)$ are the spectra of s_1 and s_2, respectively, with ω the radian frequency. The attenuation α

is given by $\alpha = \omega/2cQ$. Note that $\alpha \propto Q^{-1}$. The first term on the r.h.s. of (1) represents the time delay while the second term is the attenuation. Substituting for α in equation (1) gives

$$S_2(\omega) \quad = \quad e^{i\omega\Delta T} \quad e^{-\omega\Delta T/2Q} \; S_1(\omega) \tag{2}$$

where $\Delta T = T_2 - T_1$. Note that the r.h.s. of equation (2) is independent of both X and c, suggesting that Q can be estimated using the change in spectral content and the traveltime difference between s_1 and s_2. Here the signal spectrum is the signal attribute used to estimate Q. In the time domain, signal attributes used to estimate Q include the signal amplitude and the pulse width.

The signal amplitude depends on other factors as well as on Q. These include amplitude losses due to geometrical spreading, reflection coefficients, and the focusing and defocusing of seismic rays by curved interfaces. In addition, the instrument response and coupling may be different if two receivers are used. Corrections for these factors need to be applied to estimate Q from the change in signal amplitude. Since some of these factors are difficult to estimate accurately, signal amplitudes are generally the least reliable signal attibute to use to obtain an accurate Q estimate.

1.3 SEDIMENT SHEAR Q

In Chapter 2, sediment Q_β is estimated from *PS* and *PSSS* basement converted shear-wave reflections. *PS* and *PSSS* correspond to s_1 and s_2 given above. Estimates of Q_β are obtained from both the change in spectral content using the spectral ratio method (SR), and the ratio of the peak amplitudes (PAR) of the arrivals. To evaluate the reliability of the Q_β estimate for the OBS data, these methods are first tested on synthetic seismograms that model the data. The synthetics were computed using the reflectivity code of Mallick and Frazer (1987). Potential error in the Q_β estimate due

to noise, signal clipping from limited instrument dynamic range, and scattering from cyclic layering is investigated. The PAR method gave unreliable results. Effective sediment Q_β from spectral ratios is found to be 97 ± 11 in the frequency band 3–18 Hz. This chapter is a slightly modified version of "Sediment shear Q from airgun OBS data", P. D. Bromirski, L. N. Frazer, and F. K. Duennebier, *Geophys. J. Int.*, 1992, **110**, 465–485.

To increase confidence in a Q estimate, more than one method should be applied to the same arrivals. Accurate Q_β estimates could not be obtained for synthetic seismograms using the conventional rise time pulse width method. Consequently, a new method to estimate Q from two arrivals of the same signal, called the Q–gram method, was developed. The Q–gram method is presented in Chapter 3. In the Q–gram method, the first of the data arrivals is used as the reference signal. The method is based on propagating the reference signal for a time equal to the traveltime difference between the data arrivals using a plane wave Q–propagator. A reference curve, called a Q–gram, is generated by plotting the propagation loss between the unpropagated reference signal and the propagated wavelet vs Q^{-1}. The propagation loss is measured using a signal attribute obtained from the instantaneous phase. The Q–gram, together with the propagation loss from the data, gives the Q^{-1} of the data.

The reliability of the Q–gram method in the presence of noise and signal clipping is tested on synthetic seismograms that model the OBS data. The OBS data indicate that effective sediment Q_β is 75 ± 15. Application of the spectral ratio method using shortened windows that exclude interfering arrivals identified by means of the instantaneous frequency gives a similar estimate of sediment Q_β. This chapter is a slightly modified version of "The Q–gram method: Q from instantaneous phase", P. D. Bromirski, L. N. Frazer, and F. K. Duennebier, submitted to *Geophys. J. Int.*, Nov. 1993.

1.4 REFERENCES

Duennebier, F.K., Lienert, B., Cessaro, R., Anderson, P., and Mallick, S., 1987. Controlled-source seismic experiment at Hole 581-C, in *Init. Repts. DSDP,* **88**, pp 105-125, eds. Duennebier, F.K., Stephen, R., Gettrust, J.F., et al., Washington (U.S. Govt. Printing Office).

Hamilton, E.L., 1976a. Sound attenuation as a function of depth in the sea floor, *J. Acoust. Soc. Am.,* **59**, 528-535.

Hamilton, E.L., 1976b. Attenuation of shear waves in marine sediments, *J. Acoust. Soc. Am.,* **60**, 334-338.

Hamilton, E.L., 1980. Geoacoustic modeling of the sea floor, *J. Acoust. Soc. Am.,* **68**, 1313-1340.

Harrison, C.H. and Cousins, P.L., 1985. A study of propagation loss dependence on sediment layer thickness using the Fast Field Program, in *Ocean Seismo-Acoustics: Low Frequency Underwater Acoustics*, pp 139-148, eds. Akal, T. & Berkson, J.M., Plenum Press, New York.

Hughes, S.J., Ellis, D.D., Chapman, D.M.F., and Staal, P.R., 1990. Low frequency acoustic propagation loss in shallow water over hard-rock seabeds covered by a thin layer of elastic-solid sediment, *J. Acoust. Soc. Am.,* **88**, 283-297.

Jacobson, R.S., Shor, G.G., Jr., and Dorman, L.M., 1981. Linear inversion of body wave data - Part II: Attenuation versus depth using spectral ratios, *Geophysics,* **46**, 152-162.

Jensen, F.B. and Schmidt, H., 1986. Shear properties of ocean sediments determined from numerical modeling of Scholte-wave data, in *Ocean Seismo-Acoustics: Low*

Frequency Underwater Acoustics, pp 683-692, eds. Akal, T. & Berkson, J.M., Plenum Press, New York.

Mallick, S. and Frazer, L. N., 1987. Practical aspects of reflectivity modeling, *Geophysics,* **52**, 1355-1364.

Sutton, G.H. and Duennebier, F.K., 1987. Optimum design of ocean bottom seismometers, *Mar. Geophys. Res.* **9**, 47-65.

Vidmar, P.J., 1980a. The effect of sediment rigidity on bottom reflection loss in a typical deep sea sediment, *J. Acoust. Soc. Am.,* **68**, 634-638.

Vidmar, P.J., 1980b. Ray path analysis of sediment shear wave effects on bottom reflection loss, *J. Acoust. Soc. Am.,* **68**, 639-648.

Chapter 2

SEDIMENT SHEAR Q FROM SPECTRAL RATIOS

2.1 SUMMARY

Direct measurement of the sediment shear-wave quality factor, Q_β, has been hindered by the lack of an effective shear-wave source. We show that if a satisfactory horizontal component ocean bottom seismometer (OBS) is available, then sediment Q_β can be determined directly by using spectral ratios of converted shear-wave reflections. Spectral ratios are formed with the *PS* reflection from the sediment/basement interface and the *PSSS* multi-bounce sediment shear-wave reflection. As a check, we also computed Q_β from the peak amplitudes of *PS* and *PSSS*.

We applied the spectral ratio method to airgun OBS data collected over 356 m of primarily high-porosity biosiliceous clay in 5467 m of water in the northwest Pacific at $43°55.44'N$, $159°47.84'E$ (DSDP Site 581). An average sediment shear-wave velocity of about 0.2 km/s was obtained from the *PS* travel-time. Effective Q_β for the sediment column was found to be 97 ± 11 ($\alpha = 0.281 \pm 0.032$ dB/λ) in the frequency band 3-18 Hz.

We tested the methods by applying them to reflectivity synthetic seismograms computed for various velocity profiles with both frequency-dependent Q and frequency-independent Q. The Q_β estimate obtained from synthetic seismograms

was within 15% of the true Q_β for each velocity profile. Q_β estimates within 25% of the true Q were obtained with the addition of up to 6.5% signal-generated noise, whereas the addition of only 3% signal-generated noise energy makes estimates of the frequency dependence of Q unreliable using spectral ratios. We conclude that the 2-octave band of the data is not wide enough to determine the frequency dependence of Q_β.

Tests on synthetic seismograms, computed from models containing alternating layers of high impedance contrast with realistic velocities, indicated that apparent attenuation due to intrabed multiples does not significantly affect the spectral ratio Q_β estimates, although a shift in spectral content to higher frequencies for *PS* and *PSSS* phases and a delay in the apparent arrival time of *PSSS* were observed. However, the alternative peak amplitude ratio method gave Q_β estimates more than 25% lower than the true Q for multi-layer sediment models. We also tested the methods on synthetic data subjected to hard and soft clipping. Spectral ratio estimates of Q_β, from synthetic data with *PS* clipped up to 50%, were within 25% of the true Q_β.

Key words: sediment attenuation, spectral ratios, converted shear-wave reflections, horizontal geophone OBS data

2.1.1 Introduction

When corrected for geometric spreading, seismic body waves decay in amplitude like $e^{-\alpha x}$, where x is the source-receiver distance and α is the attenuation. Attenuation is thus a property of the material through which the waves propagate. In discussions of rock properties or of propagation loss, it is sometimes more convenient to speak of the quality factor Q, given by $Q = \pi f/c\alpha$, where f is frequency and c is the seis-

mic velocity. Attenuation includes both intrinsic losses due to anelastic heating and apparent losses resulting from scattering. Although neither the mechanism nor the exact mathematical description of attenuation is precisely known, most *in-situ* measurements imply that Q is frequency independent (Hamilton, 1976a; Kanamori and Anderson, 1977), whereas most theories suggest some form of frequency dependence (e.g. Strick, 1967).

The determination of the attenuation characteristics of seismic waves in marine sediments has been the focus of numerous studies (e.g. Hamilton, 1976a, 1976b; Jacobson et al., 1981; Jensen and Schmidt, 1986). Stratification within the sediments may result in significant scattered energy and associated interference of seismic signals that can make attenuation measurements extremely difficult. Attempts to separate effective compressional-wave attenuation into its components and to determine its frequency dependence (e.g. Jacobson, 1987) have not been conclusive. There is still no conclusive evidence of the frequency dependence of Q within the seismic band between 1 and 100 Hz, although some studies (e.g. Stoll, 1985; Jensen and Schmidt, 1986) have presented evidence that suggests that α varies as f^B, with B between 1 and 2.

The effect of sediment shear-wave parameters on acoustic propagation loss in the ocean has been examined by Vidmar (1980a,b), Harrison and Cousins (1985), and Hughes et al. (1990). Sediment attenuation can be useful in identifying sediment type (Hamilton, 1980), and changes in attenuation with depth can indicate the degree of lithification (Hamilton, 1976a; Jacobson et al., 1981). Reflectivity modeling of the oceanic crust can give erroneous results for crustal Q_β if incorrect assumptions are made about sediment Q_β.

Ocean bottom sediment compressional-wave properties can be measured directly due to the ease of generating and detecting compressional signals (e.g. Hamilton,

1976a; Jacobson et al., 1981). Although the shear-wave properties of ocean sediments can be determined using Scholte-waves (Jensen and Schmidt, 1986), numerical modeling shows that Scholte-waves propagate only in the topmost portion of the sediments. For shallow water sediments, Jensen and Schmidt found a relatively steep gradient in both shear-wave velocity, c_β, and Q_β between the sea floor and 60 m depth.

Direct measurement of sediment Q_β has been limited by the absence of high quality sediment shear-wave data. This is due largely to the lack of satisfactory ocean bottom S-wave sources, but is also related to problems in ocean bottom seismometer (OBS) design (Sutton and Duennebier, 1987). Here we circumvent the source problem by analyzing converted shear-wave reflections from the top of the crust (basement) recorded by an OBS. The detection and identification of multiply-reflected basement-converted shear-waves allows us to make the first direct measurement of effective Q_β for the entire sediment column at a deep water site.

We first present the OBS data that motivated the shear-wave analysis and discuss the key phases. We briefly review propagation parameters and alternative descriptions of attenuation. Then, using synthetic seismograms, we show that spectral ratios and peak amplitude ratios can be used to determine Q_β from converted S-wave reflections. A variety of velocity profiles are tested, with and without clipping, with and without added noise, and with the use of a realistic multi-pulse source function. Finally, we apply our methods to horizontal-component OBS data.

2.2 DATA

The OBS data used in this study were obtained in conjunction with the Ocean Subbottom Seismometer IV Experiment on DSDP Leg 88 (Duennebier et al., 1987).

The experiment site (Hole 581C) is located in $\sim$ 110 Ma crust about 40 km south of the Hokkaido Trough in the northwest Pacific basin at $43°55.44'N$, $159°47.84'E$. Typical water depth in the area is 5500 m. Single-channel reflection data show pelagic sediments roughly 350 m thick, smoothly draped over basaltic crust. Holes drilled at Site 581 on Legs 86 and 88 encountered continuous pelagic siliceous clays; chert bands beginning about 70 m above basement become numerous near the base of the sediments. Core data indicate a low velocity zone at a depth of about 200 m below sea bottom.

The data used in this study were recorded by a Hawaii Institute of Geophysics isolated sensor ocean bottom seismometer, OBS Y-220, (Byrne et al., 1983) from a 30-liter airgun towed across the site in an approximately north-south direction by Soviet research vessel Dimitri Mendeleev (Duennebier et al., 1987). The airgun was towed at a depth of 20 m and operated at a pressure of about 2000 psi with a repetition rate of 1 minute. More than 300 shots were recorded at horizontal ranges between 0 and 55 km, with nominal spacing of about 0.17 km. The analog data were digitized at 80 samples/s. Navigation, gain, and $R^{0.66}$ spreading corrections were applied.

2.2.1 Data Analysis

Figure 2.1 shows the unfiltered OBS horizontal geophone (2.1a) and hydrophone (2.1b) record sections. Horizontal geophones are sensitive to motion along their axis in the horizontal plane; this motion can be due to either non-vertical compressional-waves, to shear-waves, or, sometimes, to tilting of the instrument package. In contrast, pressure sensors detect only compressional-wave energy and are insensitive to shear-wave energy and tilt. Comparing the pressure data with the horizontal data, we see that only the direct water wave is common to both; thus the phases observed on the horizontal component must be near-vertical traveling shear-waves.

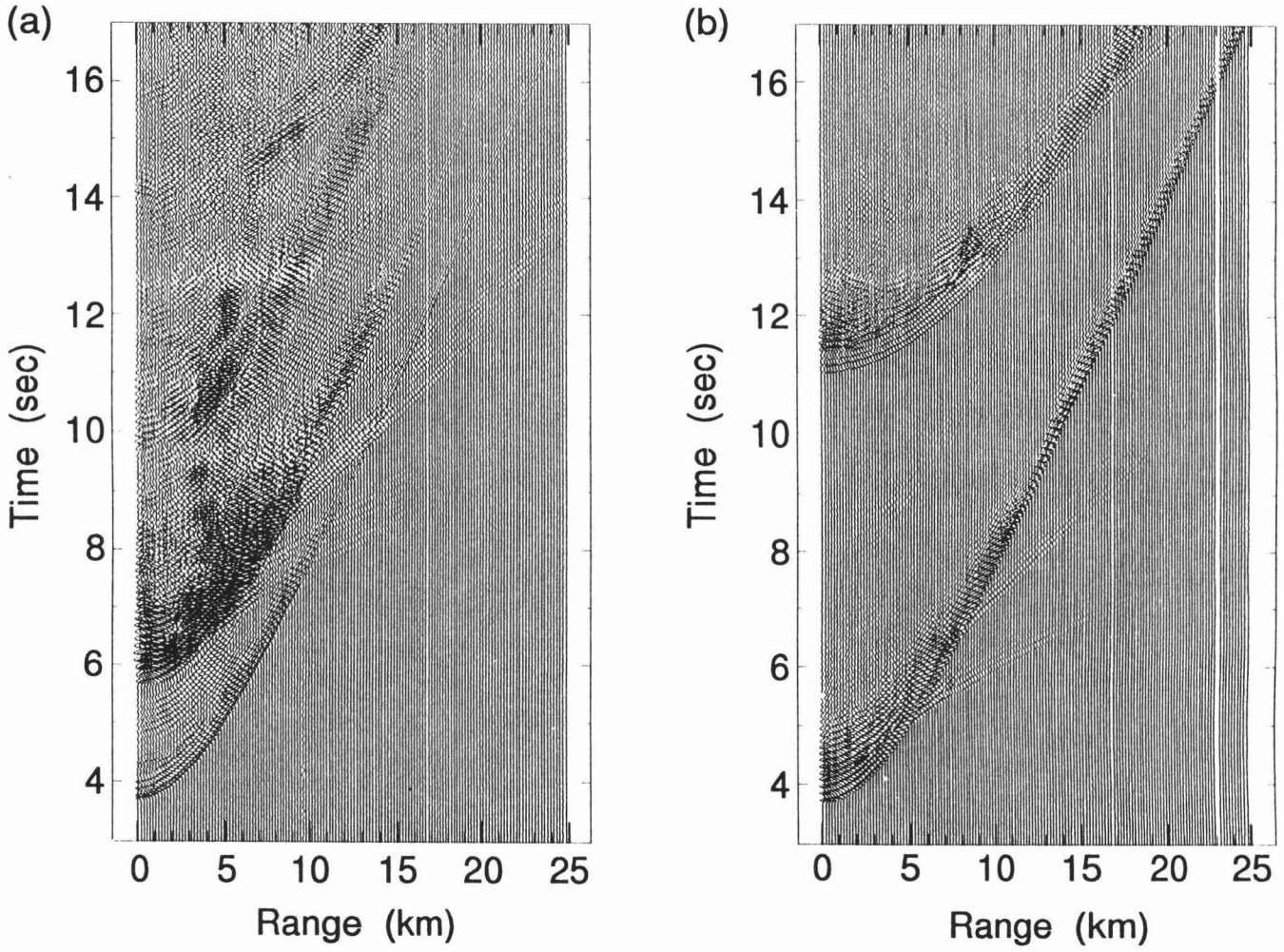

Figure 2.1: (a) Unfiltered horizontal OBS refraction data. (b) Unfiltered OBS pressure record section. Amplitudes in each record section are scaled relative to the maximum amplitude in the nearest trace.

Using the 2.00 $\pm$ 0.02 s $P+S$ travel-time from the horizontal geophone data and the sediment thickness of 356 m from drilling, we estimate an average sediment shear-wave velocity, $\bar{c}_\beta$, between 0.195 and 0.204 km/s, assuming the average sediment compressional-wave velocity, $\bar{c}_\alpha$, is between 1.8 and 1.5 km/s. Basement compressional and shear-wave velocities of 2.45 and 4.35 km/s, respectively, were obtained from the slopes of the *PSS* and *PPS* refraction branches, in general agreement with other studies (e.g. Spudich and Orcutt, 1980; White and Stephen, 1980; Duennebier et al., 1987). As it is difficult to locate precisely where these phases emerge from the converted basement reflection, or to determine their slope at that point, the actual velocities at the top of the crust may be somewhat lower than these measurements. The limited dynamic range of the instrument, which clipped some high amplitude signals, precludes amplitude versus offset analysis to identify the critical distances for the refraction phases and thereby constrain the uppermost crustal velocities.

This paper will focus on the first 12 seconds of the horizontal data (Fig. 2.2). A reduction velocity of 2.25 km/s was applied in order to separate phases and to facilitate identification of the sediment shear-wave reflections. The travel-time curves shown in Fig. 2.2 were generated by tracing rays for converted and multiply-reflected S phases using a one-layer sediment model with $c_\alpha = 1.55$ km/s, $c_\beta = 0.198$ km/s, and a sediment thickness of 356 m. The *PS* phase travels down through the sediment column as P and converts to S at the sediment/basement interface. The *PSSS* phase transits the sediment column four times, once as P and three times as S. The *PSSS* multiple shear-wave reflection from basement was the motivation for the sediment Q_β analysis in this paper.

Figure 2.3 shows the horizontal component data from selected traces at less than 2 km horizontal range, with each trace normalized to the same maximum amplitude. The water wave, *WW*, an intra-sediment reflection *IPS*, and the *PS* and

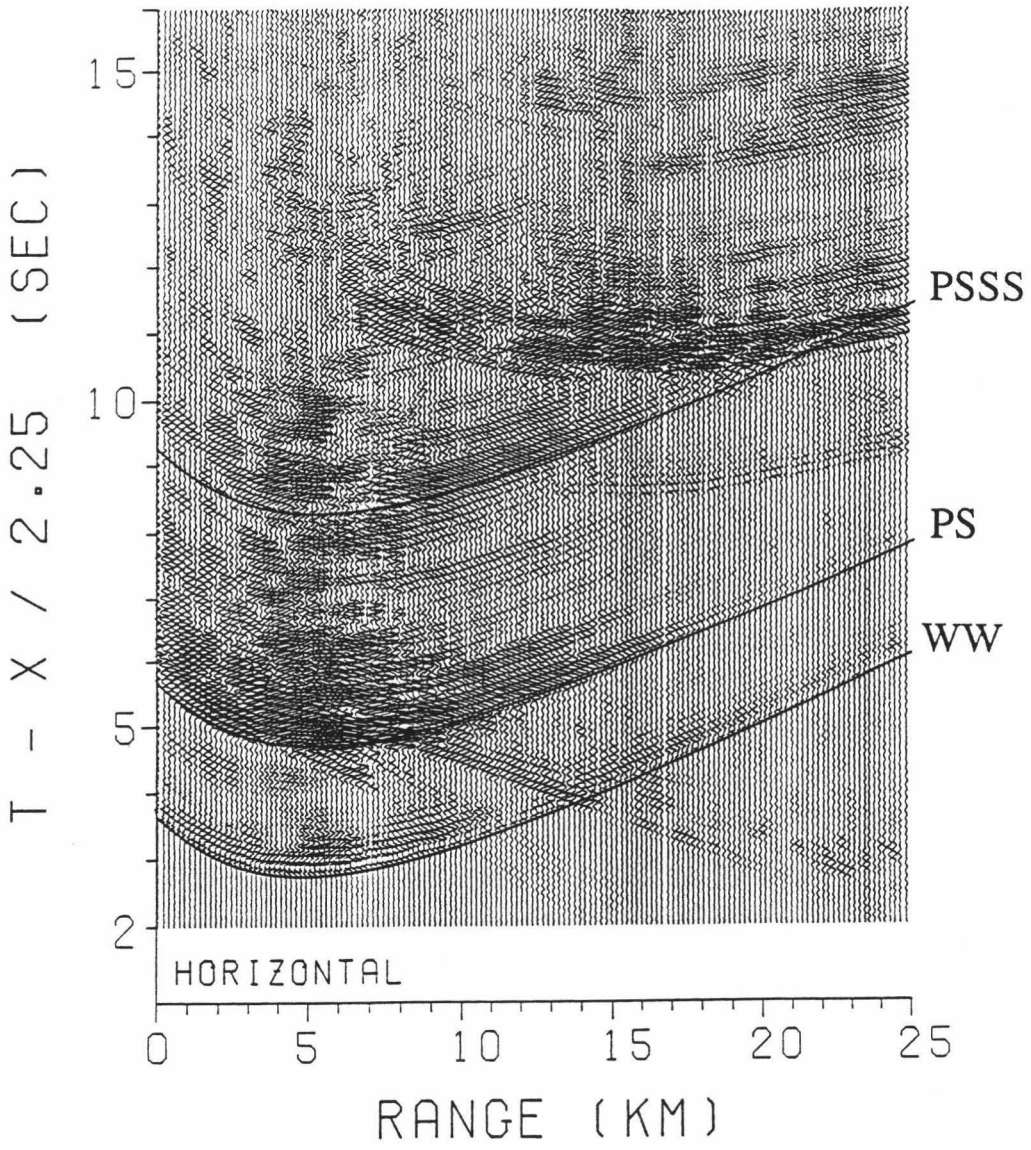

Figure 2.2: Part of the horizontal data in Fig. 2.1a reduced to 2.25 km/s with travel-time curves identifying the key converted shear reflections.

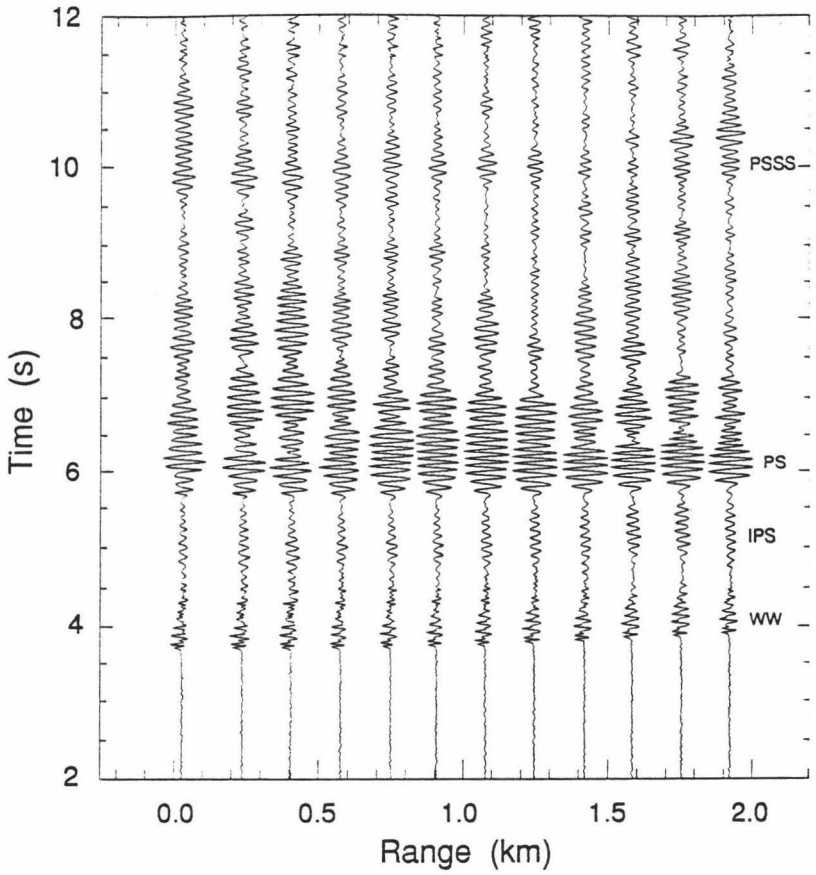

Figure 2.3: Selected trace-normalized horizontal data at distances to 2 km. The water wave, *WW*, intra-sediment converted reflection, *IPS*, and the *PS* and *PSSS* converted basement (crustal) reflections are identified. (Same data as portion of Fig. 2.2.)

PSSS converted basement reflections are identified. The phase *IPS* is identified as a converted S-wave reflection from within the sediment column by its arrival time between the *WW* and *PS* phases and by the similarity of its coda to that of the other S-wave reflections. Phases appearing between *PS* and *PSSS* that have approximately the same moveout are the result of multipathing within the sediment column.

Figure 2.4 shows the spectra of 2 s of OBS "noise" prior to the first arrival and of 2 s of "signal," starting at 5.67 s, that includes the *PS* reflection for the trace at 0.41 km in Fig. 2.3. Noise levels are a combination of background noise and signal generated noise from earlier shots. The amplitude spectrum (solid line in Fig. 2.4)

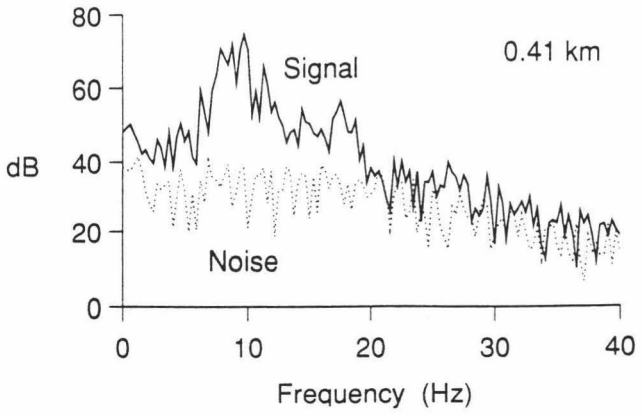

Figure 2.4: Amplitude spectra of 2 s of noise (dotted) and signal (solid) data starting at 1.5 and 5.67 s, respectively, for the trace at 0.41 km in Fig. 2.3.

of the horizontal data has a dominant frequency of about 9 Hz. The signal level is generally at least 10 dB above the noise level between 5 and 18 Hz. Spectral estimates in this paper are referenced to 1 $(digital\ unit)/\sqrt{Hz}$.

The 9 Hz dominant frequency gives a shear wavelength in the sediments of about 22 m, compared to about 190 m for compressional waves. This difference results in a finer sampling of the sediment structure using shear waves than is possible with compressional waves for this source. The sensitivity of short wavelength shear-waves to fine scale structure may explain some of the reverberation observed in the horizontal data.

2.2.2 Path Differences

Snell's Law shows that the shear legs for *PS* and *PSSS* reflections are near vertical for an average sediment shear-wave velocity $\bar{c}_\beta = 0.2$ km/s and for any reasonable choice of sediment $\bar{c}_\alpha$. The extreme case, where the incident P-wave is horizontal at the sediment/basement boundary, and $\bar{c}_\alpha = 1.5$ km/s, gives a shear-wave incident angle at the receiver of $\theta_\beta = 7.7°$. As Fig. 2.5 shows schematically, the *PS* arrival, S_1,

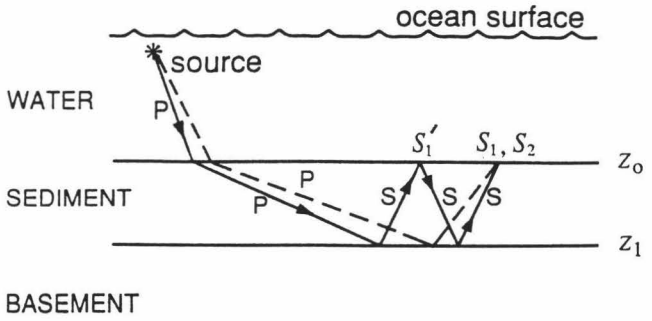

Figure 2.5: Schematic of the $S_1 = PS$ (dashed) and $S_2 = PSSS$ (solid) raypaths for a uniform sediment layer over basement.

and the PS branch of the $PSSS$ reflection, S_1', have different paths and consequently different ray parameters. In order to estimate Q_β, we compare the amplitudes and the spectra of S_1 and S_2, assuming that S_1' and S_1 are the same. The amplitudes of S_1' and S_1 depend in part on phase conversion at the sediment/basement interface and the downward path-length, with associated compressional losses, which are both angle dependent. We need to show that S_1' samples the same portion of the sediment column as S_1. As all S-paths are nearly vertical, and as S_1 and S_2 have the same source and receiver, this will be true if the downward P-paths for S_1 and S_1' at range X are approximately the same, i.e. if their ray parameters, p, are not very different.

Assuming horizontal layers, the total horizontal distance X_T between source and receiver can be expressed as

$$X_T(p) \;=\; X_W(p) \;+\; X_\alpha(p) \;+\; N_\beta\, X_\beta(p) \qquad (1)$$

where X_W is the horizontal water distance, N_β is the number of sediment shear paths, and X_α and X_β are the horizontal sediment compressional and shear-wave distances, respectively. For a stratified medium with homogeneous sediment layers, (1) may be

written in the form

$$X_T(p) = H_W \left(\frac{p\, c_w}{\sqrt{1 - p^2 c_W^2}} \right) + H_{sed} \left(\frac{p\, c_\alpha}{\sqrt{1 - p^2 c_\alpha^2}} + N_\beta \frac{p\, c_\beta}{\sqrt{1 - p^2 c_\beta^2}} \right) \qquad (2)$$

where H_W is the thickness of the water column between the source and the ocean bottom, H_{sed} is the sediment thickness, c_w is the water velocity, and c_α and c_β are the sediment compressional and shear-wave velocities. We choose a real reference distance X_T corresponding to the OBS range of interest and solve (2) for complex p_1 (*PS* phase with $N_\beta = 1$) and complex p_2 (*PSSS* phase with $N_\beta = 3$). We find that the real parts of p_1 and p_2 differ by less than 2% with $H_W = 5.467$ km and $H_{sed} = 0.356$ km, and that the sediment path-length and the travel-time of $PS(p_1)$ differ from those of $PS(p_2)$ by less than one meter and 0.01 s, respectively. Thus the P-paths and associated losses, as well as the incident angles at the basement and associated P-to-S conversion, are effectively identical for *PS* and *PSSS*.

2.3 PROPAGATION PARAMETERS

In a homogeneous medium, seismic wave propagation is determined by the phase velocity c and the specific quality factor Q, which is a dimensionless measure of the internal friction or anelasticity of the medium. Johnston and Toksöz (1981) present various definitions of Q and their inter-relationships. A definition that relates Q to wave amplitude A is given by

$$\frac{1}{Q} = \frac{1}{\pi} \frac{\Delta A}{A} \qquad (3)$$

in which ΔA is the amplitude loss per cycle. From (3) the amplitude decay due to attenuation is given by

$$A(X) = A_o \, exp\left[- \frac{\omega X}{2cQ} \right] \qquad (4)$$

where A_o is the initial amplitude, X is the path length in the attenuating medium,

c is the phase velocity, and ω is the angular frequency. The attenuation factor α is given in terms of ω or frequency f by

$$\alpha = \omega/2cQ \qquad \text{or} \qquad \alpha(f) = \frac{\pi f}{c(f)\,Q(f)} \quad . \tag{5}$$

Attenuation can also be expressed by the power-law relation

$$\alpha(f) = k_o f^B \tag{6}$$

where $0 < B < 1$ and k_o is the attenuation coefficient (Strick, 1967). In order to satisfy the Paley-Weiner causality condition, a precisely linear frequency dependence ($B = 1$) is not possible (Papoulis, 1962). Combining the expressions for $\alpha(f)$ in (5) and (6) gives

$$Q(f) = \frac{f}{f^B}\,\frac{\pi}{k_o c(f)} \quad . \tag{7}$$

It can be seen that if k_o and Q are constant and $B \neq 1$, then the velocity of propagation must be dependent on frequency. To accurately model seismic data it is important to know the frequency dependence of Q and c. We investigate the dispersion relations of Strick (1967,1970), Liu et al. (1976), and Kjartansson (1979) in a later section.

2.3.1 Effective Attenuation

Attenuation measured from field data is termed effective attenuation (α_E) as it includes contributions from both intrinsic (α_I) and apparent (α_A) attenuation. This can be expressed in terms of α or Q as

$$\alpha_E = \alpha_I + \alpha_A \qquad \text{or} \qquad Q_E^{-1} = Q_I^{-1} + Q_A^{-1} \quad . \tag{8}$$

Both Q_I and Q_A may be frequency-dependent, although in-situ measurements indicate that Q_E is effectively frequency-independent in the seismic band (Kanamori and Anderson, 1977).

Some mechanisms to account for intrinsic α_I losses are presented in Toksöz and Johnston (1981). Included are friction and frame anelasticity (Walsh, 1966), pore fluid movement between cracks (Mavko and Nur, 1979; O'Connell and Budiansky, 1978), and fluid flow relative to the mineral matrix (Biot, 1956). Stoll and Bryan (1970) and Stoll (1974) predict a nonlinear frequency dependence of the attenuation factor α for propagation of acoustic waves in saturated sediments, known as the Biot-Stoll model. Several studies suggest that Q increases with depth in sediments and may follow a power law (f^B) (Hamilton, 1980; Stoll, 1985; Jensen and Schmidt, 1986).

Apparent attenuation is the amplitude decay of a seismic pulse resulting from the scattering of energy by heterogeneities such as microbeds (O'Doherty and Anstey, 1971; Schoenberger and Levin, 1974, 1978; Spencer et al., 1977, 1982; Richards and Menke, 1983; Menke, 1983; Banik et al., 1985; Menke and Dubendorf, 1985; Lerche and Menke, 1986). In apparent attenuation, energy is redistributed to other parts of the coda, unlike intrinsic attenuation where energy is removed from the coda. However, its affect on spectral content is difficult to distinguish from intrinsic losses. Note that Q_A^{-1} includes all non-intrinsic losses.

2.4 METHODS TO ESTIMATE Q

2.4.1 Spectral Ratios

The spectral ratio (SR) method uses the ratio of the amplitude spectra of different arrivals to estimate Q. Variations of the spectral ratio method have been used by Jannsen et al. (1985) and Jacobson (1987) to determine compressional Q_α in marine sediments. We chose the spectral ratio method since the *PS* and *PSSS* reflections are observed for the same source and receiver, and the shear-wave raypaths are virtually the same.

We use the *PS* reflection (the dashed raypath in Fig. 2.5) at the reference depth, z_o, as our reference signal, with associated amplitude spectrum $S_1(\omega)$. The amplitude spectrum $S_2(\omega)$ of the *PSSS* phase (solid raypath in Fig. 2.5) is related to $|S_1(\omega)|$ by

$$|S_2(\omega)| \;=\; |S_1(\omega)\mathcal{G}\mathcal{R}|\; exp[-2\alpha(z_1 - z_o)] \tag{9}$$

where $\mathcal{G}$ is a ratio of geometrical spreading terms and $\mathcal{R}$ contains reflection and transmission coefficients, assumed independent of frequency. Here z_o is the depth at the water/sediment interface and z_1 is the depth at the sediment basement interface. Taking the natural log of the ratio of the two spectra gives

$$ln\; SR(\omega) \;=\; ln\left|\frac{S_2(\omega)}{S_1(\omega)}\right| \;=\; ln|\mathcal{G}\mathcal{R}| \;-\; 2\alpha(z_1 - z_o) \tag{10}$$

Letting $2(z_1 - z_o) = T\bar{c}_\beta$ where T is the travel time difference between successive shear multiples and $\bar{c}_\beta$ is the average shear-wave velocity in the sediments, and substituting for α with (5) we have

$$ln\; SR(\omega) \;=\; const \;-\; (\frac{T}{2}Q^{-1})\,\omega \tag{11}$$

in which *const* is a term independent of ω that includes spreading and transmission/conversion losses. This last expression differs from the expression obtained by Jannsen et al. (1985) only in the constant term. Note that if Q is independent of ω, then equation (11) describes a straight line with slope $a_1 = -\frac{T}{2}Q^{-1}$. Below we determine the value of a_1 by a least-squares fit to the spectral ratios. From this slope we obtain an effective frequency-independent Q^{-1}.

A similar procedure is used if Q is frequency-dependent. Then we expand $Q^{-1}(\omega)$ in a Taylor series about a reference frequency ω_o

$$Q^{-1}(\omega) \;\approx\; Q^{-1}(\omega_o) \;+\; (\omega - \omega_o)\frac{dQ}{d\omega} \quad . \tag{12}$$

Substituting (12) into (11) we get

$$ln\ SR(\omega) \approx const - \frac{T}{2}\left[Q^{-1}(\omega_o) - \omega_o \frac{dQ}{d\omega}\right]\omega - \frac{T}{2}\left(\frac{dQ}{d\omega}\right)\omega^2 \qquad (13)$$

which is quadratic in ω. This gives a frequency-dependent Q^{-1} at ω_o as

$$Q^{-1}(\omega_o) = -\frac{2}{T}(a_1 + \omega_o a_2) \qquad (14)$$

where a_1 and a_2 are the coefficients of ω and ω^2, respectively. The coefficients a_1 and a_2 are estimated by a least-squares quadratic fit to the spectral ratios. It can be seen that when $a_2 = 0$, equation (14) reduces to the constant Q estimate obtained from equation (11).

The *PS* and *PSSS* reflections in the OBS data contain noise. If the noise power is constant, and S_1 and S_2 are the noise free signal spectra and S_n is the noise spectrum, then

$$\frac{S_2 + S_n}{S_1 + S_n} > \frac{S_2}{S_1},$$

since S_2 is less than S_1. In general, the magnitude of this inequality will increase with frequency since S_2 decreases with frequency faster than S_1. This reduces the slope of the SR curve, giving a Q estimate that is larger than the true Q. Consequently, we subtracted the noise power from both *PS* and *PSSS* prior to taking the ratios as

$$|S(\omega)| = \left(S^2_{s+n}(\omega) - S^2_n(\omega)\right)^{\frac{1}{2}}$$

where $S_{s+n}(\omega)$ is the wavelet spectrum that includes noise. We used a portion of the data prior to the first arrival, with the same length as the signal window, for the noise estimate.

It is important to note that the Q estimated from data in this manner is an effective Q, which includes intrinsic attenuation, apparent attenuation due to scattering and intrabed multiples, interference and leakage to other paths. The relative

importance of these mechanisms will vary with sediment type and the complexity of the velocity structure in the sediment column.

As we are comparing phases for the same source and receiver, source and receiver directivity factors will not affect the relative amplitudes. From equation (10) we see that the slope of the SR plot is independent of the reflection/transmission factor $\mathcal{R}$ and of the spreading term $\mathcal{G}$. The intercept, I_{SR}, of the least-squares fit to the SR plot gives an estimate of $ln|\mathcal{GR}|$. Below we use synthetic data to examine how closely I_{SR} matches the true value of $ln|\mathcal{GR}|$.

2.4.2 Peak Amplitude Ratios

Sediment Q_β can also be estimated from the ratio of the time domain amplitude, s_1, of *PS* to the amplitude, s_2, of *PSSS* (Fig. 2.5). In order to estimate Q_β in this fashion, we need to correct s_1 and s_2 for losses due to transmission and phase conversion. For a perfectly elastic medium,

$$s_1 = G_1 R_1 \, s_o \qquad \text{and} \qquad s_2 = G_2 R_2 \, s_o$$

in which s_o is the source amplitude, and R and G are the reflection/transmission coefficient and spreading terms, with subscripts 1 and 2 referring to the *PS* and *PSSS* phases, respectively. As we have shown above that the difference between the ray parameters p_1 and p_2 for *PS* and *PSSS*, respectively, is negligible, the water-paths are nearly identical and can be neglected. Then R_2, corresponding to the *PSSS* reflection in Fig. 2.5, has the form

$$R_2 = T^d_{PP} \, R^d_{PS} \, R^u_{SS} \, R^d_{SS} \tag{15}$$

where T^d_{PP} and R^u_{SS} are the transmission and reflection coefficients at the water/sediment interface, and R^d_{PS} and R^d_{SS} are the reflection coefficients at the sediment/basement interface. The superscripts refer to the direction of propagation,

whereas the left subscript denotes the incident phase and the right subscript denotes the resultant phase.

The amplitudes, s_1 and s_2, are the maxima of the envelope functions for the *PS* and *PSSS* wavelets. The envelope function is computed by taking the square root of the sum of the squared time series and its squared Hilbert Transform. Since only the last leg is constrained to be *S*, *PSSS* also includes contributions from the *SPSS* and *SSPS* phases. This gives the ratio of the peak amplitudes of the sediment shear reflections for nearly vertical P and S raypaths as

$$\frac{s_2}{s_1} = \left|\frac{G_2}{G_1}\right| \left|\frac{(R_2 + R_3 + R_4)}{R_1}\right| \frac{e^{-(\alpha'_{\rm P} + 3\alpha'_{\rm S})}}{e^{-(\alpha_{\rm P} + \alpha_{\rm S})}} \tag{16}$$

where the subscripts P and S refer to P and S-waves, R_1, R_2, R_3 and R_4 correspond to the reflection/transmission coefficients for the *PS*, *PSSS*, *SPSS* and *SSPS* phases, respectively, and the α terms are the attenuation factors where those terms associated with s_2 are identified by primes. Note that the left hand side of (16) is a ratio of time domain amplitudes whereas the right hand side has terms in $\alpha_{\rm P}$, $\alpha_{\rm S}$ etc. which depend on frequency. We give meaning to (16) by specifying that the frequency to be used in evaluating $\alpha_{\rm P}$ and $\alpha_{\rm S}$ is f_1, the centroid of the spectrum of *PS*, and that the frequency to be used in evaluating $\alpha'_{\rm P}$ and $\alpha'_{\rm S}$ is f_2, the centroid of the spectrum of *PSSS*. Substituting for α using (5) and rearranging gives

$$\frac{1}{Q_{\rm S}} = \frac{1}{\pi f_3 \Delta T/2} ln\left|\frac{s_2}{\mathcal{G}\mathcal{R}_{\rm r}\, s_1}\right| + \left(\frac{f_2 - f_1}{f_3}\right)\left(\frac{\bar{c}_{\rm S}}{\bar{c}_{\rm P} Q_{\rm P}}\right) \tag{17}$$

where ΔT is the travel-time difference $t_{PSSS} - t_{PS}$, $f_3 = f_1 - 3f_2$, $\mathcal{R}_r = (R_2 + R_3 + R_4)/R_1$, $\mathcal{G} = G_2/G_1$ and $\bar{c}_{\rm S}$ and $\bar{c}_{\rm P}$ are the average S-wave and P-wave velocities in the sediments. Note that $ln|\mathcal{G}\mathcal{R}_{\rm r}|$ corresponds to the intercept in (11). For synthetic traces, we use model parameters to compute the frequency-dependent velocities with the dispersion relation used in reflectivity computations. The ray parameters, p, for

the *PS* and *PSSS* phases are determined from (2). To compute $\mathcal{R}_r$, we obtain the reflection/transmission coefficients from equations (5.39) of Aki and Richards (1980). $\mathcal{G}$ is obtained from the the ratio of $\cos\theta(p)\,(dA/d\Omega\,)^{-\frac{1}{2}}$ for the two phases, in which the horizontal sensor directivity term, $\cos\theta(p)$, associated with the shear-wave velocity, β, at the receiver is given by $\cos\theta(p) = \sqrt{1-p^2\beta^2}$, dA is the cross-sectional area of the ray-tube at the receiver, and $d\Omega$ is the solid angle of the ray-tube at the source. We compute $dA/d\Omega$ as

$$dA/d\Omega \;=\; \frac{X(dX/dp)}{pc_w^2}\sqrt{1-p^2c_w^2}\,\sqrt{1-p^2\beta^2}$$

where X is the horizontal range, and c_w is the water velocity at the source. For a multi-layered model, dX/dp is given by

$$\frac{dX}{dp} = \sum_{j=1}^{n} \frac{h_j c_j}{(1-p^2c_j^2)^{\frac{3}{2}}}$$

with h_j and c_j the thickness and phase velocity in the j^{th} sediment layer. The directivity terms $\cos\theta(p)$ have negligible effect since the rays are nearly vertical and $p_1 \approx p_2$. If the sediment shear-wave velocity is significantly less than the compressional-wave velocity and f_2 is not too different from f_1, the second term on the right hand side of (17) is small and can be neglected in a first order approximation of Q. These formulas are used below.

2.5 DISPERSION RELATIONS

Anelasticity in earth materials results in the dispersion of seismic waves. Attenuation, characterized by the intrinsic quality factor Q, causes a wavelet to broaden and flatten during propagation. In reflectivity modeling, attenuation is introduced by making the seismic velocities complex. Depending on the dispersion relation, the specification of a reference velocity and a reference Q, as well as additional parameters, are generally

required. However, improper selection of the additional parameters can cause either $c(\omega)$ or $Q(\omega)$ as calculated for synthetic seismograms to be significantly different from the reference values away from the reference frequency. In order to make synthetics for testing a method of extracting Q from data, we need to first examine the variation of c and Q with ω.

Based on a variety of assumptions, methods, and approximations, several investigators have derived nearly identical dispersion relations for band-limited nearly constant Q using a standard linear solid for their viscoelastic model (e.g., Futterman, 1962; Liu et al., 1976; Kanamori and Anderson, 1977). In a different approach, Strick (1967, 1970) used the power law (6) to obtain an expression for $c(\omega)$ that does not require bandwidth specification. Both the band-limited and the Strick relations require the selection of parameters that affect the frequency dependence of c and of Q, and the resulting waveforms.

In contrast to these nearly-constant Q models, Kjartansson (1979) gives a linear description of attenuation with Q exactly independent of frequency; attenuation is completely specified by c_o, the phase velocity at a reference frequency f_o, and by Q. Kjartansson's model requires the phase velocity to be slightly dependent on frequency.

We review several dispersion relations to examine their potential differences and the influence of parameter selection. Here it is useful to have Q defined in terms of complex seismic phase velocity, $c(\omega)$, by

$$Q(\omega) \;=\; 0.5\,\frac{Re\,[1/c(\omega)]}{Im\,[1/c(\omega)]} \quad . \tag{18}$$

This definition, from O'Connell and Budiansky (1978), is nearly equivalent to definition (3) for body waves, but it is more convenient than (3) because neither the change in amplitude nor the cycle length needs to be determined.

- Absorption Band (ABQ) rule (Liu et al., 1976), modified from Mallick and Frazer

(1987):

$$c(\omega) \;=\; c_{\mathrm{o}} \left\{ \; 1 \; + \; \frac{1}{\pi Q_{\mathrm{m}}} \, ln \left[\frac{\omega_2(\omega_1 - i\omega)}{\omega_1(\omega_2 - i\omega)} \right] \right\} \tag{19}$$

Here ω_1, ω_2, c_{o}, and Q_{m} are input parameters. The radian frequencies ω_1 and ω_2 are intended to be chosen so that $\omega_1 \ll \omega \ll \omega_2$ in the band of interest. The reference velocity c_{o} is the velocity of the medium both at $\omega = 0$ and $\omega \rightarrow \infty$. Note that the $Q(\omega)$ given by this rule is not equal to the parameter Q_{m}: $Q(\omega) > Q_{\mathrm{m}}$ for all ω, but $Q(\omega)$ is only slightly greater than Q_{m} for $\omega_1 \ll \omega \ll \omega_2$. Notice that $Q(\omega) \rightarrow \infty$ both in the limit $\omega \rightarrow 0$ and in the limit $\omega \rightarrow \infty$.

- Power Law (PLQ) rule (Strick, 1967,1970), a modified version of Strick's Power Law as presented in Mallick and Frazer (1987):

$$\frac{1}{c(\omega)} \;=\; \frac{1}{c_\infty} + \frac{k_{\mathrm{o}}}{\sin(\frac{\sigma\pi}{2})} \frac{1}{(\varepsilon - i\omega)^\sigma} \tag{20}$$

Here c_∞, k_{o}, ε, and σ are the input parameters. However, it is usually more convenient to define k_{o} by the relation $k_{\mathrm{o}} \equiv |\omega_{\mathrm{o}}|^\sigma / 2c_\infty Q_{\mathrm{m}}$ and then to regard c_∞, ω_{o}, Q_{m}, ε, and σ as input parameters. In consequence of the above definition of k_{o}, equation (20) implies that for $\omega \gg \varepsilon$

$$Q(\omega) \approx \left| \frac{\omega}{\omega_{\mathrm{o}}} \right|^\sigma Q_{\mathrm{m}} \; + \; \frac{1}{2} \cot(\sigma\pi/2) \; .$$

Notice that $Q(\omega)$ is greater than Q_{m} whenever $\omega > \omega_{\mathrm{o}}$. Substituting the expression for k_{o} into (20) gives

$$\frac{1}{c(\omega)} \;=\; \frac{1}{c_\infty} \left\{ \; 1 \; + \; \frac{1}{2Q_{\mathrm{m}}} \frac{|\omega_{\mathrm{o}}|^\sigma}{\sin(\frac{\sigma\pi}{2})(\varepsilon - i\omega)^\sigma} \right\} \; .$$

It can be seen that c_∞ is the seismic velocity in the limit as $\omega \rightarrow \infty$.

The parameter ε was introduced by Mallick and Frazer (1987) to remove the velocity singularity at $\omega = 0$; for body waves, ε should be chosen so that $\varepsilon \ll \omega$ in the band of interest; we use $\varepsilon = 0.001$.

- Constant Q (CQ) rule (Kjartansson, 1979):

$$c(\omega) = c_o \left(\frac{i\omega}{\omega_o}\right)^{\gamma} \tag{21}$$

Here c_o, ω_o and γ are the input parameters. However, it is often more convenient to define γ by $\gamma = \frac{1}{\pi}\tan^{-1}\left(\frac{1}{Q_m}\right)$ and c_o by $c_o = c_m/\cos\left(\frac{\pi\gamma}{2}\right)$ so that c_m, ω_o and Q_m are the input parameters. With this dispersion relation it is easy to see that Q is independent of ω. However, like the ABQ rule and the PLQ rule, the CQ rule gives a seismic velocity that increases with frequency.

For testing our procedures, we require synthetic seismograms computed both with a frequency-independent Q and with a frequency-dependent Q. We chose $f_o = 1$ Hz for the reference frequency, with $\omega_o = 2\pi f_o$. Figure 2.6 shows $c(\omega)$ and $Q(\omega)$ for three dispersion relations. Clearly the Q and c given by these relations differ significantly from the input parameter Q_m away from the reference frequency. In selecting values for the parameters ω_1 and ω_2 in the ABQ, and σ in the PLQ relations, there is a trade-off between constant Q and $c(\omega)$. Keeping Q nearly constant away from ω_o causes $c(\omega)$ to diverge more from the reference phase velocity, and vice versa. Although the shapes of the phase velocity curves in Fig. 2.6a are similar, we found that improper selection of the other input parameters can cause the PLQ and ABQ curves to differ significantly from the CQ curve. For the ABQ it was necessary to increase the bandwidth to $\omega_1 = 0.01$ and $\omega_2 = 10000$ (the dashed curves in Fig. 2.6) in order for $Q(\omega)$ to be effectively constant over the frequency band 3 to 18 Hz (Fig. 2.6b) and maintain $c(\omega)$ relatively constant, compared with $\omega_1 = 0.1$ and $\omega_2 = 1000$ (dotted). For the ABQ relation, as ω_1 decreases, $c(\omega)$ increases. Examination of (19) and Fig. 2.6a indicates that ABQ increases the propagation velocity of a pulse, whereas PLQ gives the delay generally expected in a dispersive medium. However, we see in

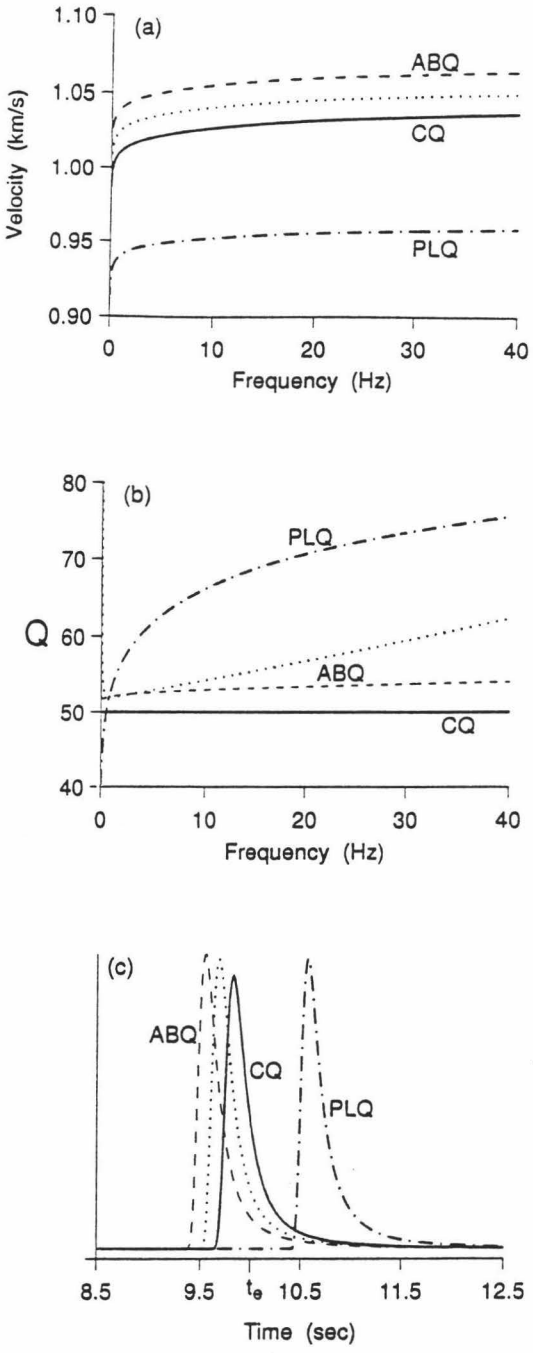

Figure 2.6: Results from various dispersion relations: (a) Velocity; (b) $Q(\omega)$ calculated using (18); (c) Impulse response for plane wave propagation through 10 km of medium at a reference velocity of 1 km/s and a reference Q of 50. t_e is the expected arrival time. The curves in each plot were computed using Constant Q (solid), Power Law Q (dot-dash) with $\sigma = 0.1$ and $\varepsilon = 0.001$, and Absorption Band Q (dotted) with $\omega_1 = 0.1$, $\omega_2 = 1000$ and (dashed) with $\omega_1 = 0.01$, $\omega_2 = 10000$. For all computations, $f_o = 1$ Hz.

Fig. 2.6b, obtained from $c(\omega)$ using equation (18), that PLQ gives $Q(\omega)$ considerably greater than Q_{m} for $\omega > \omega_{\mathrm{o}}$.

To see the differences in the resulting waveforms, we computed the plane wave solutions for the reference model using $c_{\mathrm{o}} = c_{\infty} = c_{\mathrm{m}} = 1.0$ km/s and $Q_{\mathrm{m}} = 50$ at $x = 10$ km. As Fig. 2.6c shows, the waveforms are similar in shape although the arrival times differ from the 10 s time expected for the model parameters. The differences become more pronounced as Q_{m} decreases. As Q_{m} increases, the waveforms approach the same amplitude and their arrival times approach x/c. Note that the input velocity and Q_{m} can be adjusted so that the three dispersion relations give similar results in a given frequency range. And it may be possible to choose k_{o} in the PLQ model and Q_{m} in the ABQ model such that the $Q(\omega)$ and $c(\omega)$ curves are closer together. However, it is unclear what values of k_{o} and Q_{m} to use for unconsolidated sediments and whether these parameters should vary with material type. Since the modeling of seismic data involves the matching of travel times and amplitudes, it is clear that different dispersion relations can require distinctly different input models to obtain similar synthetic seismograms. The differences in the $Q(\omega)$ and $c(\omega)$ curves emphasize the importance, in modeling studies, of explicitly stating the dispersion relation and its input parameter values.

2.6 NUMERICAL TESTS ON SYNTHETIC DATA

Reflectivity synthetic seismograms were computed using both the CQ and PLQ dispersion relations. We used $f_{\mathrm{o}} = 1$ Hz as the reference frequency for both relations. For the PLQ computations, we used $\sigma = 0.1$ and $\epsilon = 0.001$, with c_{∞} and Q_{m} the reflectivity model velocity and model Q, respectively. For the CQ computations, c_{m} and Q_{m} are the reflectivity model parameters. The code used to generate the syn-

thetic seismograms was developed by Mallick and Frazer (1987, 1988). In this study, a variety of sediment models were used to test the accuracy of the spectral ratio (SR) and peak amplitude ratio (PAR) methods for Q_β estimation. SR and PAR give effective Q_β, equation (8), as the reflectivity synthetics include all multiples and converted phases.

From single-channel reflection data and core logs from drilling (Duennebier et al., 1987), it is certain that the actual sediment column at Hole 581C has vertical heterogeneity. Hence we require a definition of intrinsic Q for an n-layer sediment profile. A natural definition is obtained by considering the effect of the intrinsic Q of each layer on a vertically traveling seismic wave. The amplitude loss of the wave in layer j due to intrinsic attenuation can be expressed as $exp[-\omega h_j/2c_jQ_j]$, in which h_j, c_j, and Q_j are the thickness, phase velocity, and Q in layer j, and ω is the angular frequency. The loss for a stack of n layers, L_n is then

$$L_n = exp\left[-\omega\left(\frac{h_1}{2c_1Q_1} + \frac{h_2}{2c_2Q_2} + \cdots + \frac{h_n}{2c_nQ_n}\right)\right] \tag{22}$$

Next, we define $\bar{c}$ to be the total thickness of the stack, $H_T = \sum_{j=1}^{n} h_j$, divided by the total travel time; thus

$$\bar{c} = H_T \left[\sum_{j=1}^{n} \frac{h_j}{c_j}\right]^{-1} \tag{23}$$

Finally, we define Q_I, the effective intrinsic Q of the stack, by writing

$$L_n = exp\left[-\frac{\omega H_T}{2\bar{c}\,Q_I}\right] \tag{24}$$

Solving equations (22) and (24) for Q_I then yields

$$Q_I = \frac{H_T}{\bar{c}} \left[\sum_{j=1}^{n} \frac{h_j}{c_jQ_j}\right]^{-1} \tag{25}$$

In these equations the c_j, and Q_j are frequency-dependent quantities computed using the dispersion relation for the j^{th} layer. For the multi-layer sediment models in

this study, we refer to Q_I in equation (25) as the true Q. In discussing our tests on synthetic data, we will say that a method gave the correct result if the Q recovered by the method was equal to Q_I given by (25).

2.6.1 Synthetic Data

Here we discuss the synthetic record sections used to develop and test our SR and PAR methods for extracting Q_β. Recall that in the SR method we must first estimate the spectrum of *PS* and the spectrum of *PSSS*; Q_β is then obtained from the slope of the ratio of these two spectra. The synthetic traces were computed with a Nyquist frequency of 40 Hz, consistent with the OBS data sampling interval of 0.0125 s. We used 55-point windows for *PS* and *PSSS* in order to match the length of the *PS* coda in the OBS data at 0.41 km (Fig. 2.3). Prior to transforming to the frequency domain, the mean was removed and a 10% Hanning taper was applied to the windowed phases. Tests showed that 256 point windows padded with zeros gave the best results. Although tapering the window is unnecessary for synthetic data from simple models free of noise, we include the taper in our tests since the OBS data may contain other phases and noise arriving close to the *PS* and *PSSS* wavelets.

The airgun source function and the theoretical instrument response were included in our modeling to facilitate direct comparison of synthetics to the OBS data. At first glance it might be surmised that the source and the instrument functions should be self-canceling in both the SR and PAR methods. In theory they are not exactly self-canceling in the SR method because a long source-instrument wavelet may cause the tails of the *PS* and *PSSS* arrivals to be outside their respective windows; they are not exactly self-canceling in the PAR method because of the possible interference of other phases with *PS* and *PSSS*. Accordingly, in the synthetic seismograms used below to test our methods for estimating Q_β, we included a source

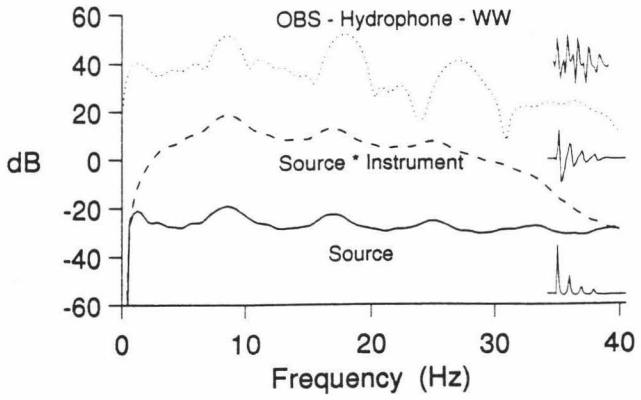

Figure 2.7: Amplitude spectra for the source wavelet, source convolved with the instrument response, and water wave from the OBS hydrophone data at about 13 km. The wavelets giving these spectra are shown at the right.

and instrument response similar to those of the data. However, we also tested our SR and PAR methods with a variety of other source-instrument wavelets, including the unit (delta function) wavelet. We found that both methods were relatively insensitive to the source-instrument wavelet; the other factors discussed below such as noise, clipping, and interference had much larger effects.

The HIG OBS horizontal component instrument velocity response is relatively flat between 3 and 20 Hz (Sutton et al., 1980) where most of the energy in the data is found (Fig. 2.4). The instrument response was computed with the formula in Table IV of Sutton et al. (1981) using $\tau_1 = 0.035$. The Soviet airgun source was modeled using a modified form of the explosive source function presented in Spudich and Orcutt (1980). The spectral content of the airgun source wavelet is a function of the airgun volume, chamber pressure, and depth. The source function parameters that control the bubble pulse decay were estimated by comparing the amplitude spectrum of the source wavelet convolved with the instrument response with the water wave from OBS hydrophone data at about 13 km (Fig. 2.7), where the water wave is not

severely clipped as in the near traces. The peaks in the amplitude spectra of the convolved wavelet and the OBS water wave at about 9 Hz match reasonably well (Fig. 2.7), as does the fall off in the spectral estimates between the first and third peaks. Since the water wave in real data is contaminated by the sediment basement P reflections, as well as by refracted phases and surface waves not included in the convolved wavelet, we can only approximate the shape of its spectrum. To match the water wave spectrum, we need an accurate sediment model and an accurate transfer function between the instrument and the sediments in which it rests.

Spikes or holes in the spectral ratios can be caused by other arrivals in the same time window. Holes in either of the spectra due to time series discretization can also cause the SR curve to be irregular. When the spectral estimate of *PSSS* is greater than that of *PS* at the same frequency, or when the *PS* and *PSSS* spectra are significantly dissimilar in shape, interference with another phase or with noise is the likely cause. The longer the source-receiver wavelet and the more complicated the sediment structure, the greater the chance that interference effects will be encountered. As interference is likely in real data, we smoothed the amplitude spectra using a $\frac{1}{4}, \frac{1}{2}, \frac{1}{4}$ smoothing function before taking the spectral ratios. The degree of acceptable smoothing was established with tests on simple models where apparent attenuation would not be a factor, and we could ensure that the trend of the SR curve was not distorted. We found that five passes through the smoothing function gave minimal distortion of the SR curve. The bandwidth for least-squares estimation was restricted to those frequencies where the general trend of the SR curve was approximately the same as that near the dominant frequency. The difference between the true Q and the estimated Q is the measure of error.

2.6.2 Tests on 1 and 2–Layer Sediment Models

The application of the spectral ratio (SR) method to synthetic seismograms computed using the Constant Q rule for 1-layer sediment models with Q_β of 50, 100 and 150 (Table 2.1) recovered the intrinsic model Q_β with an error less than 5%. The spectral ratio curves for these models are virtually linear and are consequently not shown. Although, as noted above, the source and instrument are not exactly self-canceling in the SR method, our tests of SR for these models with and without the source and instrument functions gave results that were insignificantly different. The peak amplitude ratio (PAR) method Q_β estimates were between 10% and 20% below the model Q. To assess the sensitivity of the PAR method to the frequency parameters in equation (17), we also computed Q_β from (17) by substituting, in turn, $-2f_1$, $-2f_2$, and $\bar{f} = -2[(f_1 + f_2)/2]$, in place of f_3. These substitutions were motivated by the expectation that f_2 would not be too different from f_1.

The most accurate PAR results for both low and high-Q models were obtained with $\bar{f}$ in place of f_3, although $-2f_1$ and $-2f_2$ in place of f_3 gave smaller errors for high and low-Q, respectively. The PAR results using $\bar{f}$ in place of f_3 were within 5% of the model Q. This improvement may result from $\bar{f}$ compensating for the band-limited nature of the source spectrum. We use $\bar{f}$ in place of f_3 for the remainder of the PAR tests unless otherwise stated.

The spectral ratio intercept I_{SR} from equation (10) gives an estimate of the shear-to-shear reflection coefficient at the sediment/basement interface R^d_{SS} as

$$|R^d_{SS}| \approx |\mathcal{R}_\mathrm{r}| = exp(\mathcal{I}_{S\mathcal{R}} - ln|\mathcal{G}|) \tag{26}$$

Note that the PS reflection coefficients in R_1 and R_2, equation (16), essentially cancel because $p_1 \approx p_2$ and because R_3 and R_4 make only small contributions to $\mathcal{R}_\mathrm{r}$. Also, the spreading ratio $\mathcal{G}$ is easily computed if the sediment thickness is known. Equation (26) gives a lower bound for R^d_{SS} since layering within the sediment column and conversion

of S-to-P at the water bottom will make $|\mathcal{R}_{\mathrm{r}}| < |R^d_{SS}|$. In general, R^d_{SS} will be negative since we expect a significant increase in c_α, c_β, and ρ at the sediment/basement interface.

Table 2.1: Input parameters for 1-layer sediment models with velocities c_α, c_β in km/s and density ρ in gm/cm^3.

	c_α	Q_α	c_β	$Q_\beta(a)$	$Q_\beta(b)$	$Q_\beta(c)$	ρ	h(km)
water	1.49	5000	0.0		0		1.0	5.467
sediment	1.77	50	0.198	50	100	150	1.80	0.356
basement	4.25	300	2.25		250		2.75	____

For the 1-layer models in Table 2.1, equation (26) gave R^d_{SS} within 5% of the model value. In addition, increasing the sediment Q_α and the basement Q_α and Q_β had an insignificant effect on the accuracy of the SR and PAR results for these models. This indicates that Q_β determined by these methods is effectively independent of other attenuation parameters.

To test the robustness of SR and PAR for more complicated sediment structures, horizontal component synthetic seismograms were computed, for both low and high Q_β, with a relatively strong impedance boundary within the sediment column. Table 2.2 gives two 2-layer models that differ from each other only in the Q_β of the two sediment layers. The parameters in Table 2.2 serve as the input model parameters to the dispersion relations of the reflectivity code. Table 2.3 gives the actual velocities, at 9 Hz, of the models in Table 2.2, computed by the CQ rule (21), and the actual Q's, at 9 Hz, computed using the O'Connell and Budiansky relation (18). The intrinsic Q_β of the sediment column, given by substituting Table 2.3 values into equation (25), is 50 in case (a) and 200 in case (b). Note that the Table 2.3 values are also obtained from the PLQ rule at 9 Hz, using the input parameters c_∞ and Q_{m} given in Table 2.4. The non-linear nature of the PLQ dispersion relation required adjustment of the

Table 2.2: Input parameters c_{m} and Q_{m} used in computing the synthetic traces in Fig. 2.8. Velocities are in km/s and densities are in gm/cm^3. Actual velocities at 9 Hz are given in Table 2.3.

		c_α	Q_α	c_β	Q_β (a)	Q_β (b)	ρ	h(km)
water		1.5	10000	0.0	0		1.0	5.467
sediments	L1a	1.55	30	0.160	45	190	1.35	0.200
	L1b	1.75	30	0.295	70	225	1.75	0.156
basement		4.25	300	2.25	250		2.65	____

Table 2.3: Computed velocity and Q at 9 Hz determined from the input parameters c_{m} and Q_{m} in Table 2.2 using the Constant Q dispersion relation. The resulting intrinsic Q, given by equation (25), is 50 for sediment column (a) and 200 for sediment column (b), using $\bar{c}_\beta = 0.2$ km/s.

		c_α	Q_α	c_β (a)	c_β (b)	Q_β (a)	$Q_\beta(b)$	ρ	h(km)
water		1.5	10000	0.0		0		1.0	5.467
sediments	L1a	1.62	30	0.165	0.161	45	191	1.35	0.200
	L1b	1.83	30	0.300	0.297	70	226	1.75	0.156
basement		4.27	301	2.26		251		2.65	____

Table 2.4: Input parameters c_∞ and Q_{m} used in computing the Power Law synthetic trace in Fig. 2.8. Velocities are in km/s and densities are in gm/cm^3. Actual values of velocity and Q at 9 Hz, computed by the PLQ dispersion relation, are identical to those of Table 2.3.

		c_α	Q_α	c_β (a)	c_β (b)	Q_β (a)	$Q_\beta(b)$	ρ	h(km)
water		1.5	10000	0.0		0		1.0	5.467
sediments	L1a	1.80	21.5	0.179	0.164	33	150	1.35	0.200
	L1b	2.05	21.5	0.315	0.301	53	178	1.75	0.156
basement		4.31	238	2.29		198		2.65	____

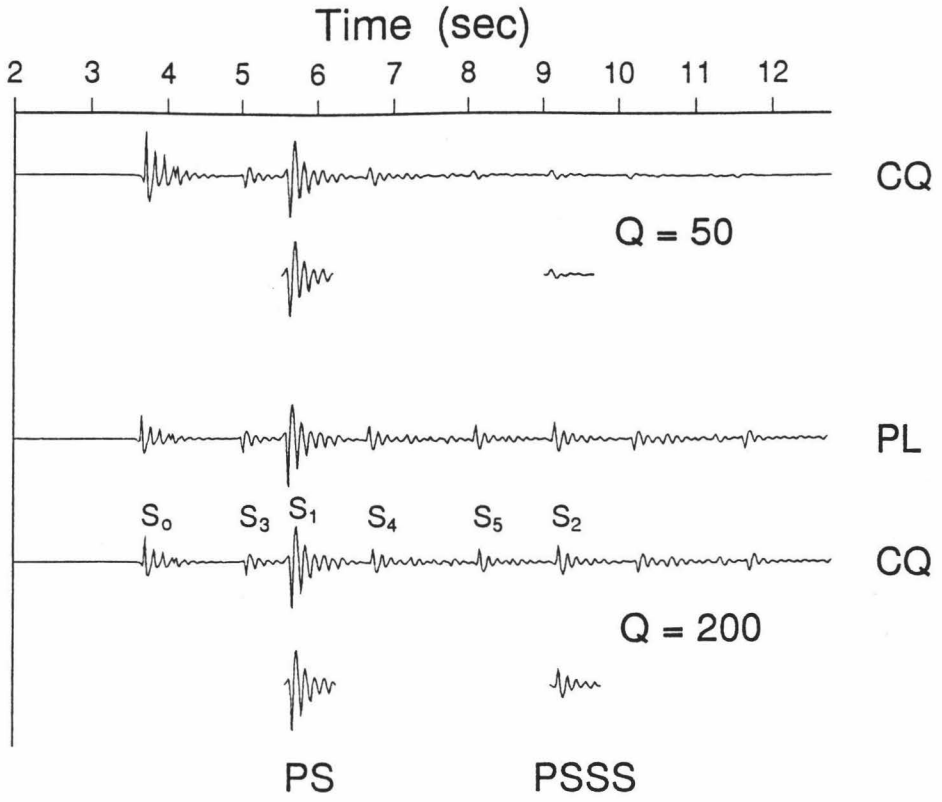

Figure 2.8: Reflectivity synthetic traces for the 2-layer sediment models of Table 2.3 showing the wavelets selected for Q analysis for the CQ models. Raypaths for the arrivals identified on the lower trace are shown in Fig. 2.9. The PL trace for $Q = 50$ is omitted because it indistinguishable from the CQ trace for $Q = 50$.

velocities as well as Q in order to match the sediment Q_β, Q_α, c_β, and c_α in Table 2.3. Using the model parameters in Table 2.4, equation (20) gives velocities and layer Q within 1% of the values in Table 2.3. Note the significant difference between the CQ (Table 2.2) and PLQ (Table 2.4) model Q_β necessary to obtain the same values of Q_I and $\bar{c}$ for the sediment column; this difference was noted earlier in the curves for $Q(\omega)$ and $c(\omega)$ in Fig. 2.6.

Figure 2.8 shows the traces computed for these models at a range of 0.41 km, corresponding to trace 3 in the OBS data (Fig. 2.3). Figure 2.9 shows the raypaths of the major arrivals identified on the bottom trace in Fig. 2.8. In Fig. 2.9, all raypaths not labeled P are S, and phases resulting from reflection/conversion at the intra-

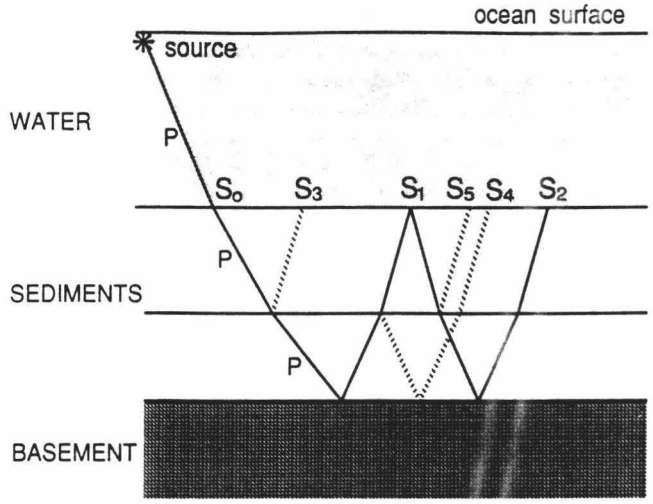

Figure 2.9: Raypaths for the arrivals identified on the bottom trace (CQ, $Q = 200$) in Fig. 2.8. The down-going P-wave legs are labeled P. All other legs are S-waves; the dashed legs result from reflection/conversion at the intrasediment (IPS) boundary.

sediment boundary are dashed. Additional layers significantly increase the multipathing and the complexity of the seismic trace, with the number and amplitude of phases observed depending on the magnitude of the impedance contrast between the layers. The seismogram for the PLQ model with intrinsic $Q_\beta = 200$ is also plotted in Fig. 2.8. As expected, very little difference can be seen between the traces for the CQ and PLQ models. The close similarity of these traces demonstrates that identical synthetic seismograms can be obtained from significantly different input models when different dispersion relations are used. The amplitude spectra for the CQ and PLQ models also show only slight differences (Fig. 2.10a). The PLQ trace for intrinsic $Q_\beta = 50$ is omitted because it is similarly indistinguishable from the corresponding CQ trace and amplitude spectrum (case (a), Table 2.2).

Figure 2.10a shows the smoothed amplitude spectra of the *PS* and *PSSS* wavelets in Fig. 2.8. The resulting spectral ratio curves are shown in Fig. 2.10b. The differences between these models can readily be seen in the relative amplitudes of the *PS* and *PSSS* phases, their amplitude spectra, and the slope of the SR curves. Assuming constant Q_β, a straight line was fitted to each spectral ratio curve and equation (11) was used to estimate Q_β. We obtained $Q_\beta = 52 \pm 1$, in the band [3,15] Hz, and $Q_\beta = 198 \pm 3$, in the band [3,25] Hz, for the low and high-Q CQ models, respectively. The $\pm$ refers to 95% confidence limits for the least-squares fit to the spectral ratios. Recovered Q_β varied less than 10% from the true Q_β for both CQ models in Table 2.2 using bandwidths of at least 10 Hz that included the dominant frequency of 9 Hz. Estimates without tapering the wavelets differed from these results by less than 5%. The error for the high-Q model increases slightly as the bandwidth decreases, with $Q_\beta = 208 \pm 10$, in the band [3,15] Hz. The general trend of the low-Q SR curve in Fig. 2.10b changes at about 15 Hz, restricting the usable bandwidth for the low-Q model. This is because the spectral estimates at frequencies greater than about 15 Hz (lower dotted curve in Fig. 2.10a) approach the numerical noise level, related to a combination of the source function spectral content and the low Q_β. The accuracy of these SR Q_β estimates suggests that layering and S to P conversion do not present problems for the SR method.

We also used the quadratic least-squares procedure, equations (13) and (14), to estimate Q_β from traces computed using the PLQ dispersion relation. The quadratic least-squares Q_β procedure is much more sensitive to bandwidth than the linear least-squares procedure. The most accurate Q_β estimates were obtained for the band where the significance of the second order term in the quadratic least-squares fit was a minimum, as determined by standard F-Test techniques (Hines, W.W. and Montgomery, D.C., 1980). However, the quadratic least-squares results of $Q_\beta =$

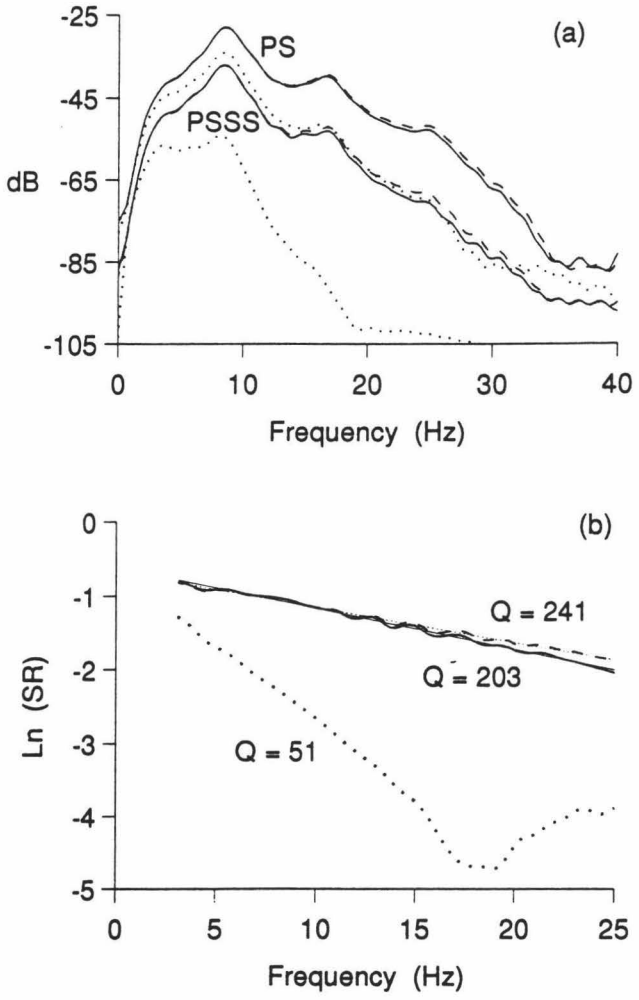

Figure 2.10: *PS* and *PSSS* amplitude spectra (a) and associated spectral ratio (SR) curves and Q_β estimates (b) of the CQ (solid, $Q = 200$; dotted, $Q = 50$) and PLQ (dashed, $Q = 200$) traces in Fig. 2.8. The thin lines in (b) are the least-squares fits for the band in which the SR Q_β estimate was obtained.

54 ± 0.1, in the band [3,15] Hz, and $Q_\beta = 241 \pm 3$, in the band [3,18] Hz, for the low and high-Q PLQ models, respectively, are still within 25% of the true Q_β values. The $\pm$ refers to the average deviation of the high and low estimates obtained from 95% confidence limits for the least-squares coefficients a_1 and a_2 in (14). The Q_β estimates for the high-Q model have greater than 25% error for bands with the upper limit less than 18 Hz, e.g. $Q_\beta = 267$ in the band [3,15] Hz. The error for the high-Q model decreases as the bandwidth increases, with $Q_\beta = 222$, in the band [3,25] Hz.

The quadratic least-squares Q_β estimates from PLQ synthetic seismograms (Fig. 2.10b) do not recover the true Q_β as accurately as the linear least-squares procedure applied to Constant Q synthetics. This is probably due to averaging effects over the band for which the quadratic least-squares estimate is obtained. For some bands, the quadratic least-squares procedure applied to PLQ synthetics gave errors greater than 50% whereas the linear least-squares procedure, applied to the same PLQ synthetics, gave Q_β estimates within 10% of the true Q at 9 Hz. For example, for the low-Q PLQ model in the [3,15] Hz band, we obtained $Q_\beta = 150$ with the quadratic fit and $Q_\beta = 54$ with the linear fit. For the high-Q PLQ synthetics, quadratic fit SR Q_β estimates are generally within 40% of the true Q_β. However, for most bands a linear fit gave Q_β estimates within 25% of the true Q_β at 9 Hz, significantly better than the quadratic fit estimates. These results indicate that any frequency dependence of Q will be very difficult to extract from our OBS data.

To determine the usefulness of the PAR method on real data, where the sediment column is likely to be heterogeneous, we also applied the PAR method to the traces in Fig. 2.8. When estimating Q_β using the peak amplitude ratio (PAR) method for multi-layer sediment structures, the reflection coefficient term, R_r, in equation (17), must be modified to include the S-wave transmission coefficients, T^u_{SS}, and T^d_{SS}. The expression for the *PSSS* reflection-transmission factor R_2, equation (15), then

becomes

$$R_2 = T^d_{PP}\, R^d_{PS}\, T^u_{SS}\, R^u_{SS}\, T^d_{SS}\, R^d_{SS}\, T^u_{SS} \ .$$

For the low-Q 2-layer model, PAR results using both the spectral ratio intercept, I_{SR}, and model parameters to estimate $\mathcal{GR}_{\rm r}$ gave Q_β estimates within 10% of the true Q. However, the estimates for the 2-layer high-Q models are about 30% below the true Q using the model $\mathcal{GR}_{\rm r}$, whereas substituting $exp(I_{SR})$ for $\mathcal{GR}_{\rm r}$ in (17) resulted in less than 5% difference between the estimated and true Q_β. These results suggest that interference between phases resulting from conversion at, and reflections from, the *IPS* boundary causes a reduction in the peak amplitude of the *PSSS* reflection, and that these interference effects are included in the SR intercept. This is surprising in that interference is a frequency-dependent phenomenon while I_{SR} should contain only frequency-independent components. In addition, the interference effect on I_{SR} does not affect the spectral ratio results.

2.6.3 Noise

Real data can be influenced by factors not usually included in synthetic seismograms such as noise and signal "clipping" due to limited recording dynamic range. To determine the sensitivity of the SR and PAR methods to these factors, we applied different levels of signal clipping and noise to the synthetic data.

To determine the accuracy of the SR method in the presence of noise, we added different levels of noise energy to the high-Q_β wavelets. Noise was incorporated in the synthetic wavelets by taking a portion of the corresponding OBS data trace preceding the water wave as the noise estimate and adding it to both the *PS* and *PSSS* wavelets prior to transforming to the frequency domain. Such added noise has a greater affect on the spectral estimates of the lower amplitude *PSSS* wavelet than it does on the higher amplitude *PS*. We also generated random, or white, noise in the frequency

domain by fixing the noise modulus at unity and randomizing the phase, transforming to the time domain, and adding the result to the synthetic trace. We express the percent of noise energy as $100 \log_{10}$ of the ratio of the variance of the noise amplitudes to the variance of the signal+noise amplitudes for the *PSSS* wavelet. When obtaining spectral noise estimates, we windowed the noise with the same taper used on the signal.

Subtracting the noise power from the spectral power estimates steepens the slope of the spectral ratios and consequently has the effect of lowering the Q_β estimate. If noise power is not subtracted from the signal power spectra before the spectral ratio is taken, then the Q_β estimate may be higher than the true value. The high-Q_β models are more sensitive to noise since a slight change in slope can result in a significant error in the Q_β estimate. Accordingly, for our noise analysis, we use the high-Q CQ model in Table 2.2 with $Q_\beta = 200$.

A linear least-squares fit to the spectral ratios was made using the frequency band in which spectral estimates for the *PS* phase were at least 3 dB greater than those of the *PSSS* wavelet and the spectral estimates for both phases were at least 3 dB above the noise level. These acceptance criteria can reduce the usable bandwidth significantly and exclude certain frequencies within that band. Fig. 2.11a shows the wavelet spectra after adding about 5.5% data noise energy to the high-Q CQ model trace in Fig. 2.8. For the *PS* phase, very little difference can be seen between the amplitude spectra with noise added (solid) and without noise for frequencies less than 30 Hz. However, for *PSSS*, near 15 Hz and above 19 Hz there are noticeable differences between the amplitude spectra with noise and without noise. These small differences significantly affect the spectral ratio curve. The SR curve becomes considerably more irregular (solid, Fig. 2.11b). But the Q_β estimate obtained with the noise power subtracted as discussed above, using those frequencies in the [3,25] Hz band that

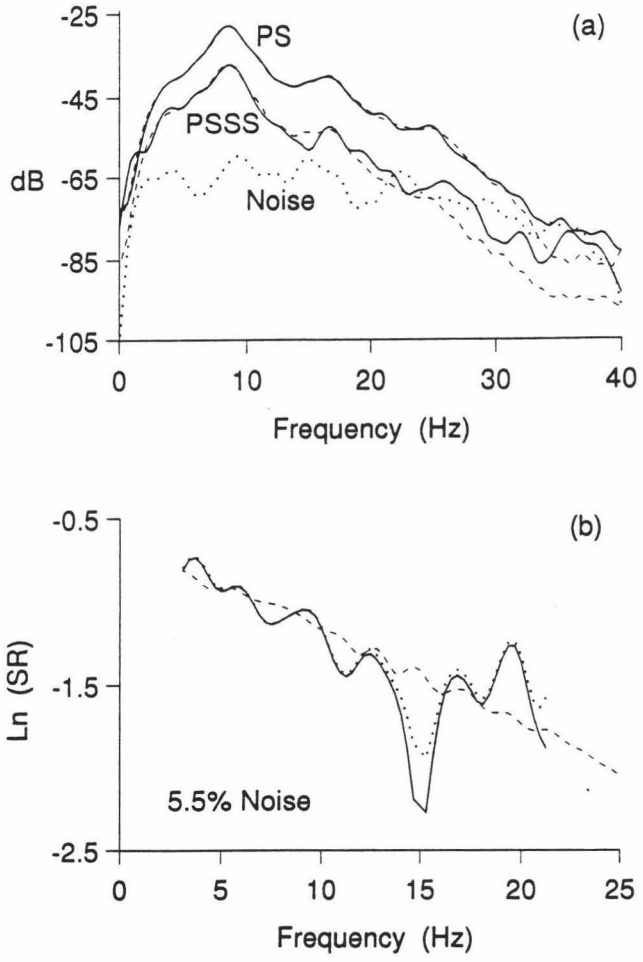

Figure 2.11: (a) Amplitude spectra of the *PS* and *PSSS* wavelets in Fig. 2.8 with about 5.5% noise energy added (solid) for the CQ model with $Q = 200$. Also shown are the noise free spectra (dashed) and the noise estimate (dotted). (b) Spectral ratio (SR) curves for the spectra in (a) with the noise power removed (solid), not removed (dotted) and the noise free case (dashed).

meet our acceptance criteria, was 216 ± 38, still within 10% of Q_I. In Fig. 2.11b, the short linear portion of the SR curve near 15 Hz shows the frequencies not used in the fit. Although not subtracting the noise power does not appear to change the shape of the SR curve significantly (dotted, Fig. 2.11b), it results in a Q_β estimate of 248 ± 40 for the same band; thus the bias in the Q estimate increased from 10% to 25% when noise was not subtracted. Data noise gave larger errors in the Q_β estimates than did random noise, so we used data noise for the remainder of our tests.

As noise levels increase, the usable bandwidth narrows and the portion of the amplitude spectrum above noise level becomes smaller and more distorted. The associated SR curves are more irregular with more frequencies excluded. Subtracting the noise power compensates for both the reduction in slope of the SR curve and the associated downward shift in the spectral ratio intercept. We obtain less than 25% error between measured and true Q_β with the addition of up to 6.5% noise to the synthetic data for the high-Q CQ model. For the 1-layer sediment models in Table 2.1, and for multi-layer sediment models with lower impedance contrast or with Q_β less than 150, we find better than 25% accuracy for as much as 8% noise energy added. These results differ somewhat from those reported by Janssen et al. (1985) and Tonn (1991) who obtained greater than 25% error for the addition of more than 5% noise energy. The improved accuracy we obtained may be be due to the lack of down-going S-waves through the water column, the nearly perfect S-wave reflection at the water/sediment interface, the subtraction of the noise power from the spectral estimates prior to taking the ratios, or a combination of the above.

For the PLQ $Q_\beta = 200$ synthetics, the addition of about 5% noise energy causes Q_β estimates to be more than 25% different from the true Q. We found that the linear least-squares procedure gave much better estimates than the quadratic fit for PLQ models when more than 3% noise energy was added. For example, for the

$Q_\beta = 200$ PLQ model with 5% noise, we obtained Q_β estimates of 144 and 213 using the quadratic and linear least-squares procedures, respectively. These results indicate that, when noise is present in narrow band data, a linear approximation to the spectral ratios gives the most reliable Q_β estimate for both frequency-dependent and frequency-independent Q. We also infer that, from our real data, which undoubtedly include noise and interference effects, it will be very difficult to determine any frequency dependence of Q_β.

The peak amplitude ratio (PAR) method was also tested with noise for the 1-layer $Q_\beta = 150$ model (b) in Table 2.1. The PAR method gave better results than the SR method as the noise levels increased above about 8%, where the SR slope became negative. The PAR estimates of Q_β were within 10% of the model Q of 150 with up to 25% noise energy added using the model $\mathcal{GR}_\mathrm{r}$ in (17). This means that if we are sure the sediment column is nearly homogeneous, if we know the sediment thickness, and if we can make a good estimate of $\mathcal{R}_\mathrm{r}$, then sediment Q_β can be determined accurately even in the presence of considerable noise by comparing peak amplitudes of selected phases.

2.6.4 Clipping

Clipping due to restricted instrument dynamic range affects primarily the *PS* reflection for the near traces. The gain in the OBS record section used in this study was set automatically according to the RMS voltage for the previous minute, resulting in clipping of the highest amplitude signals in each trace. To test the impact of clipping on the SR Q_β results, we applied "hard" and "soft" clipping to CQ synthetic data for the 2-layer model with $Q_\beta = 200$. In both cases the clipping level was set to a percentage of the maximum amplitude of the *PS* wavelet. For hard clipping, all amplitudes greater than the clipping level were set to the clipping level. We limited

clipping of *PS* to levels at which *PSSS* was not clipped. As can be seen in Fig. 2.12a, hard clipping results in a shift of energy to higher frequencies, increasing the centroid frequency of the *PS* spectrum. In Fig. 2.12b, it is clear that increased clipping causes greater distortion of the SR curves between 3 and 20 Hz.

For soft clipping, the wavelets were first scaled by $\sinh(1.0)/(clipping\,level)$. We took the $\sinh^{-1}$ of the scaled amplitudes to obtain the the soft clipped wavelets shown in Fig. 2.13(a). Comparing Figures 2.12a and 2.13a, we see that hard clipping shifts more energy to higher frequencies than does soft clipping. In Fig. 2.13, we see that as the amount of clipping increases, more energy shifts to the higher frequencies, the SR curves become more distorted, and their intercepts become more positive. However, the SR method still yields estimates within 25% of the model Q with up to 50% hard or soft clipping applied to the wavelets.

Application of the PAR method to data with the *PS* phase clipped will give an upper bound for Q_β if we have a reasonably good estimate of $\mathcal{R}_\mathrm{r}$. As expected, the PAR method is sensitive to clipping and gives a much higher Q_β estimate than the true Q. However, using $-2f_1$ and $\exp(I_{SR})$, in place of f_3 and the model $\mathcal{GR}$, respectively, in (17), gave results close to the true Q. In addition, as clipping increases above 35%, the centroid frequency increases; then using twice the dominant frequency for the *PS* reflection, $-2f_{1\mathrm{D}}$, in place of f_3 in (17), gives Q_β estimates closer to the true Q than using either f_3, $\bar{f}$, or $-2f_1$. For the source function employed, the difference between f_1 and $f_{1\mathrm{D}}$ is an indication of the amount of clipping present in the data. These results show that the amplitude spectrum below 20 Hz is not greatly affected by moderate amounts of clipping, and that clipping effects are mostly confined to the SR intercept.

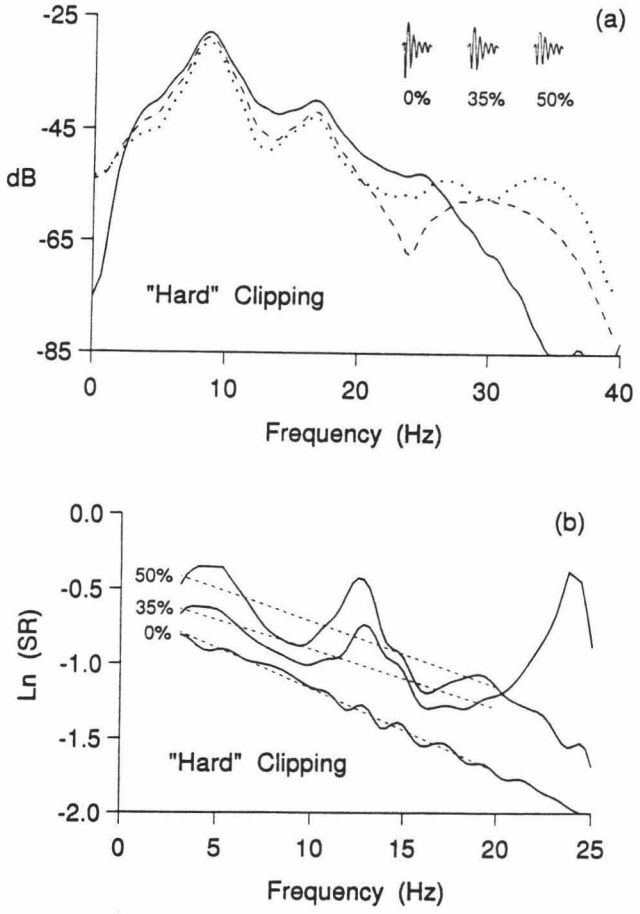

Figure 2.12: (a) Amplitude spectra for the *PS* wavelet in Fig. 2.8 with 0 (solid), 35 (dashed), and 65% (dotted) "hard" clipping applied. (b) Spectral ratio curves for the spectra in (a), with the spectrum of *PSSS* in Fig. 2.10, gave estimates for Q_β of 201 $\pm$ 5.4, 281 $\pm$ 36, and 252 $\pm$ 44 for 0, 35, and 50% clipping, respectively. The dashed lines are the least-squares fits over the band in which the Q_β estimate was obtained.

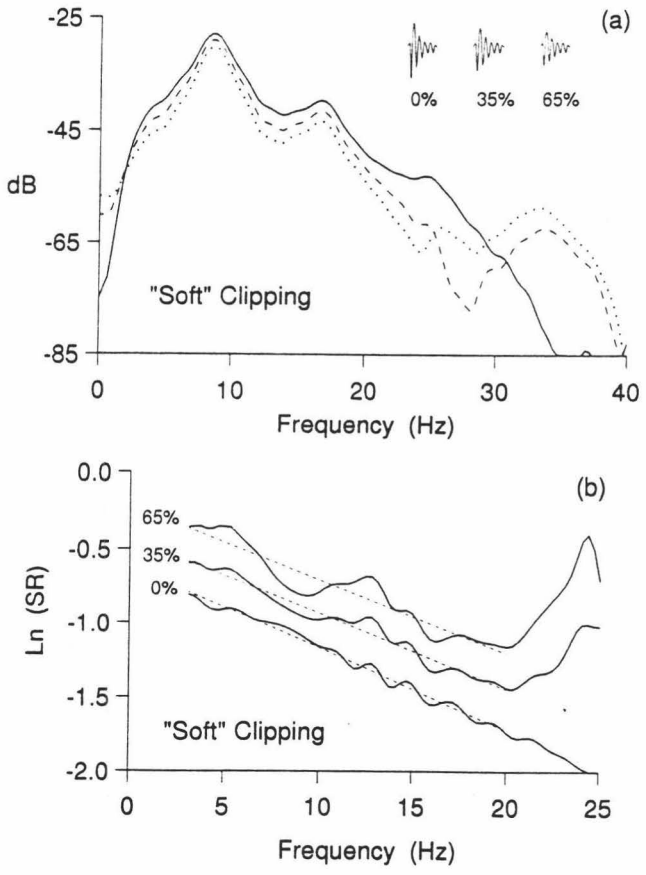

Figure 2.13: (a) Amplitude spectra for the *PS* wavelet in Fig 2.8 with 0 (solid), 35 (dashed), and 65% (dotted) "soft" clipping applied. (b) Spectral ratio curves for the spectra in (a), with the spectrum of *PSSS* in Fig. 2.10, gave estimates for Q_β of 201 $\pm$ 5.4, 216 $\pm$ 10, and 221 $\pm$ 19 for 0, 35, and 65% clipping, respectively. The dashed lines are the least-squares fits over the band in which the Q_β estimate was obtained.

2.6.5 Apparent Attenuation

Here we consider the effects of apparent attenuation on our procedures for estimating Q_β. In particular, for multi-layered models, we wish to know whether our procedures tend to estimate the Q_I given by equation (25), or whether they recover an effective Q containing a strong component of apparent attenuation. First, notice that if Q_A is large, then equation (8) reduces to $Q_E = Q_I$. If Q_A is small, then the Q_E estimated by the SR method will be less than the true Q_I. We decided to hold Q_I fixed at a relatively high value and see how Q_E estimated by the SR and PAR methods differs from the true Q_I.

Synthetic seismograms were computed for sediment models with realistic velocities containing alternating layers with high impedance contrast. These models were designed to maximize the magnitude and frequency of impedance contrasts while maintaining total $P+S$ sediment travel-time of about 2.00 s for a sediment thickness of 356 m. The vertical travel time through each sediment layer was held constant for velocities computed with the Constant Q rule. These sediment models (Table 2.5) have layer thicknesses of $1, \frac{1}{2}, \frac{3}{8}, \frac{1}{4}$ and $\frac{1}{8}\ \lambda_\beta$ at 10 Hz, respectively, while holding shear $Q_I = 150$ fixed. In Table 2.5, the number of sediment layers having the same density, velocity and Q in that layer is in parentheses, e.g. model A5 has 142 sediment layers. Residual fractions of layers were distributed equally between the top and bottom layers. Figure 2.14 shows synthetic traces computed at 0.41 km with the constant Q rule, with the $Q_\beta = 200$ CQ 2-layer model from Table 2.2 at the top included for comparison.

As the synthetics shown in Fig. 2.14 are horizontal motion, virtually all of the energy is in shear. In particular, the energy between *WW* and *PS* consists of intra-sediment P-to-S converted arrivals. Note that the amplitude of the water wave is approximately the same for all models. In model A2 (Fig. 2.14), the amplitude of the

TABLE 2.5. Alternating sequence of sediment model parameters used in computing the synthetic seismograms for models A1 through A5 with sediment layer thickness of $1, \frac{1}{2}, \frac{3}{8}, \frac{1}{4}$, and $\frac{1}{8}\,\lambda_\beta$, respectively, at 10 Hz. In parentheses are the number of sediment layers having the same density (ρ, gm/cm^3), velocity (c_α, c_β, km/s) and Q. Total sediment thickness is approximately 356 m.

	c_α	Q_α	c_β	Q_β	ρ	h (m)				
						A1	A2	A3	A4	A5
water	1.51	10000	0.0	0	1.0	5467				
sediments	1.55	100	0.150	150	1.45	15.0	7.5	5.625	3.75	1.875
	1.85	100	0.250	150	1.75	25.0	12.5	9.395	6.25	3.125
	1.55	100	0.150	150	1.45	15.0	7.5	5.625	3.75	1.875
	1.85	100	0.250	150	1.75	25.0	12.5	9.395	6.25	3.125
	.	.	.	.	.	.	.	.	.	.
	.	.	.	.	.	.	.	.	.	.
	.	.	.	.	.	.	.	.	.	.
	1.55	100	0.150	150	1.45	15.0 (9)	7.5 (17)	5.625 (24)	3.75 (36)	1.875 (71)
	1.85	100	0.250	150	1.75	25.0 (9)	12.5 (17)	9.395 (24)	6.25 (36)	3.125 (71)
basement	4.25	300	2.35	250	2.65	170				
	Gradient - 6 layers					170 m each				
	6.1	500	3.5	300	2.4	10000				

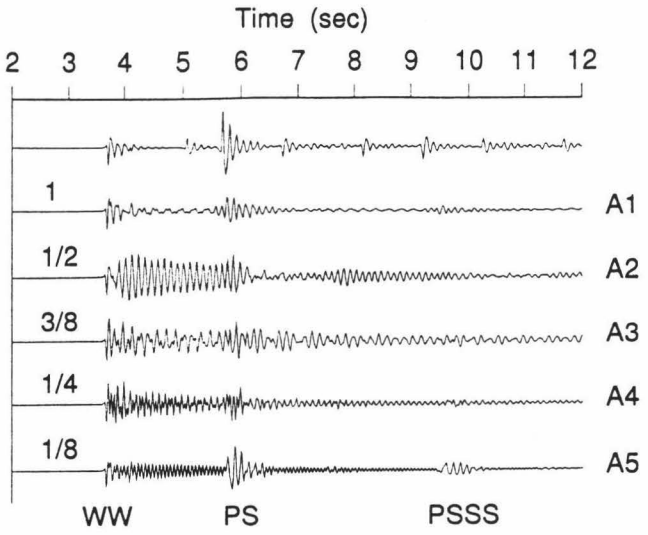

Figure 2.14: Synthetic data traces at 0.41 km for models A1-A5 with alternating sediment layer thicknesses of 1, $\frac{1}{2}$, $\frac{3}{8}$, $\frac{1}{4}$ and $\frac{1}{8}$ λ_β (see Table 2.5). The trace at the top is for the constant Q 2-layer high-Q model.

converted S-phases decreases with time as more energy is removed from the downgoing P-wave. The amplitude reduction is also partly due to the upgoing S-waves losing energy to reverberations, reconversion, and absorption in the sediment column.

Interference of the converted S-phases occurs where the thickness of successive layers sums to an integer multiple of $\frac{1}{4}\lambda_\beta$, giving the characteristic pattern observed for the arrivals between *WW* and *PS*. A resonance condition exists when the sediment thickness is an odd multiple of $\frac{1}{4}\lambda_\beta$. The resonance frequency, f_r, is given by

$$f_r = \frac{c_\beta\, m}{4\, H_{sed}} \qquad (m = 1, 3, 5, ...),$$

where H_{sed} is the thickness of the sediments. Applying this expression to the individual layers in model A4 gives $f_r = 10$ Hz with $m = 1$ for each of the contrasting layers, corresponding to the fundamental resonance frequency for the stack of layers.

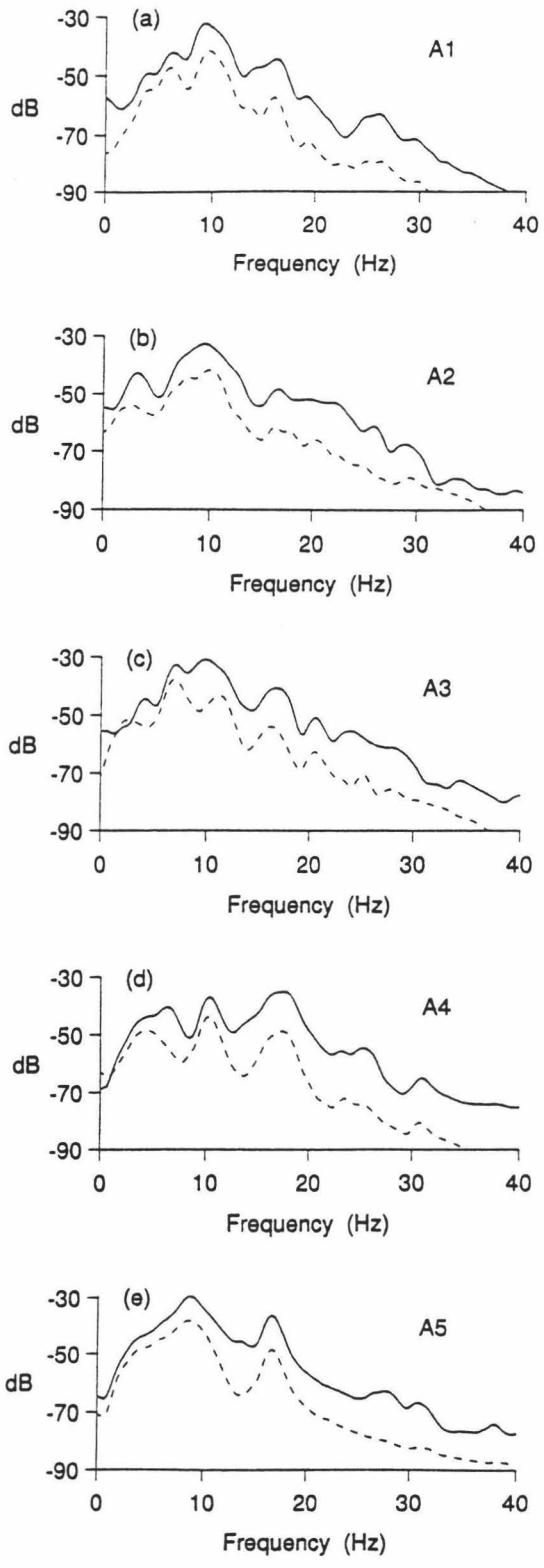

Figure 2.15: Amplitude spectra (a-e) for the *PS* (solid) and *PSSS* (dashed) wavelets from the traces models A1-A5 shown in Fig. 2.14.

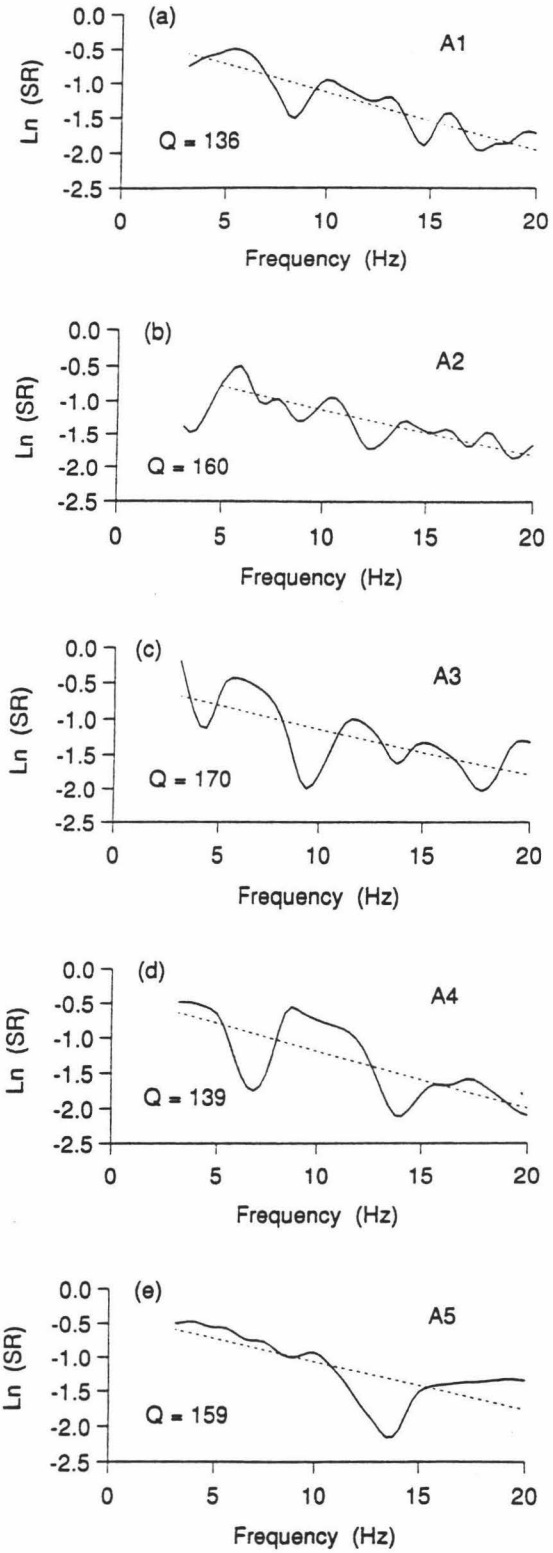

Figure 2.16: Spectral ratio curves for the amplitude spectra in Fig. 2.15 for models A1-A5 (a-e). The dashed lines are the least-squares fits over the band in which the Q_β estimate was obtained.

Consequently, we associate the peak at 10 Hz in models A1-A4 in Fig. 2.15 with the acoustic propagation loss maximum determined by Hughes et al. (1990) for one layer sediment models.

The arrivals between *WW* and *PS* increase in frequency from about 10 Hz for model A2 to about 18 Hz in model A4. As the layer thickness decreases, the layers become increasingly transparent to the downgoing P-wave resulting in less P-to-S conversion. In model A5 (Fig. 2.15e), the $\frac{1}{8}\lambda_\beta$ layer thickness is small enough to allow the 9 Hz peak in the source spectrum (Fig. 2.7) to control the location of the dominant frequency of the *PS* and *PSSS* spectra, as opposed to the 10 Hz dominant frequency in the spectra of models A1-A3. The 10 Hz peak matches the frequency used to determine the layer thicknesses. For model A4, the pronounced peak in the spectrum near 18 Hz is likely due to phases that include odd numbers of multiple raypaths in both layers. In general, the sediment layers act as a strongly peaked bandpass filter whose zeros are related to the thicknesses and velocities of the layers in the sequence.

The wavelet arrival times for models A1-A5 were computed by ray theory. All models have a time-average sediment S-wave velocity of 0.201 km/s with arrival times for *PS* and *PSSS* of 5.61 and 9.14 s. Since thin-bed layering delays the arrival of some of the energy, we used a larger window, 1.0 s, for the spectral ratio analysis compared with the 0.69 s window in the analyses of the 2-layer sediment models above. The phases *PS* and *PSSS* still arrive at the computed times, but their amplitudes can be significantly reduced (Fig. 2.14). The delay of energy is clearest in model A5 where the apparent *PSSS* arrival occurs at about 9.42 s, 0.29 s later than the ray theoretical arrival time. The window positions for spectral estimation were not adjusted to compensate for these delays. To reduce the possible effect of other arrivals near *PS* and *PSSS* within the 1 sec windows, we applied a 10% Hanning taper to the wavelets.

The upper bound of the band in the SR tests was 20 Hz because the spectral estimates approached the numerical noise level above this limit. The lower bound was set at 3 Hz except for model A2 in which it was set to 5 Hz. Below 5 Hz, the SR curve for model A2 was greatly distorted, probably because of interference.

As expected, the *PS* and *PSSS* phases for these models have much more irregular amplitude spectra and SR curves (Figures 2.15 and 2.16) than those of the noise free 2-layer models (Fig. 2.10). The spectrum of model A4 (Fig. 2.15d) clearly shows a significant shift in the dominant frequency of the wavelets to about 18 Hz with a corresponding reduction in the peak at 10 Hz. The linear least-squares SR method for models A1-A5 gives Q_β estimates within 25% of the true Q of 150 with 95% confidence limits between ± 26 and ± 47. These results could have been improved by shifting the time windows to compensate for the layering delay and by increasing the percent of the wavelets tapered. We conclude that spectral ratio estimates of Q_E will not be significantly affected by apparent attenuation due to intrabed multiples resulting from thin, horizontal bedding within the sediment column in the [3,20] Hz band. In our analysis of the OBS data, we expect that the Q_β recovered will be close to the intrinsic Q defined for multi-layer models by equation (25).

In addition to estimating the importance of Q_A, the long codas for these models also test the sensitivity of the SR method source function and window length. Interference may explain why the 95% confidence limits for the Q_β estimates for models A1-A5 are significantly larger than those for the 2-layer models of Table 2.2.

2.7 APPLICATION TO OBS DATA

After the extensive tests on synthetic data discussed above, we applied the SR and PAR methods to the OBS horizontal data from DSDP Hole 581C. The position and

length of each wavelet window was adjusted to obtain as smooth an amplitude spectrum as possible. After the mean was removed from the wavelets, the 10% time-domain Hanning taper and smoothing functions were applied in the same way as for the synthetic data. For noise estimates needed in the SR method, we selected the portion of the data prior to the first arrival starting at 2.0 s after the origin time for the shot, with the same length as the wavelets used for the spectral ratios. The noise power was subtracted from the spectral power estimates after smoothing.

We restricted our analysis to offsets less than 1.0 km. Since the shear-waves take a nearly vertical path, the near traces are least contaminated by scattered energy or by refracted crustal phases. Fig. 2.17a shows the horizontal component OBS data at 0.41 km and the *PS* and *PSSS* wavelets selected for spectral ratio analysis. The intra-sediment converted reflection, *IPS*, and the direct water wave, *WW* are also identified. The phases arriving between *PS* and *PSSS* are shear-waves that probably result from multi-pathing within the sediment column. Noise levels restrict the usable band for the SR method to about 3-18 Hz. The noise energy estimate for this trace is 4.7% of the *PSSS* wavelet, corresponding to a signal-to-noise ratio of 21, well within the 25% SR accuracy range in the presence of noise energy determined from the tests on synthetic data above. We conclude that signal generated noise does not significantly reduce the accuracy in determining Q_β by either the SR or PAR methods from these OBS data. Fig. 2.17b shows that the shapes of the signal spectra are roughly similar to those for the 2-layer synthetic data shown in Fig. 2.11a; thus interference and clipping are probably not significant for this trace.

The horizontal geophone is contained in a cylindrical OBS instrument package. Coupling through soft sediments can modify the instrument response to ground motion, with the coupling resonance frequency related to the shape and mass of the instrument package and the properties of the sediments (Sutton, et al., 1981). Cou-

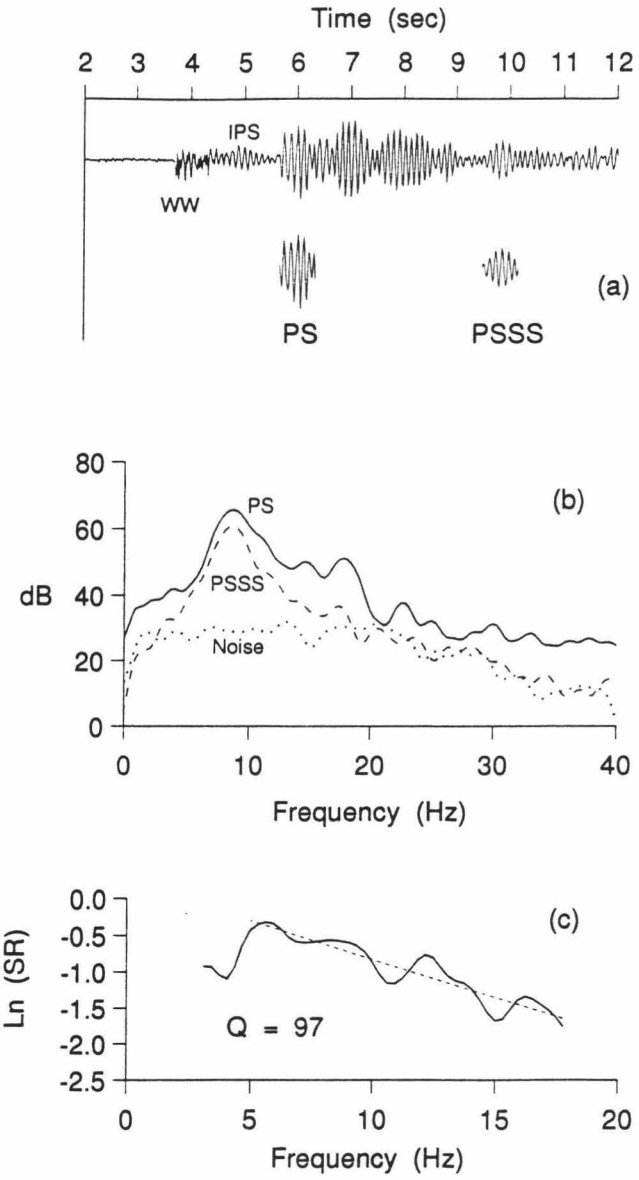

Figure 2.17: (a) Horizontal geophone OBS data at 0.41 km with the *PS* and *PSSS* wavelets for SR and PAR analysis. The water wave, *WW* and the intrasediment reflection *IPS* are also identified; (b) Amplitude spectra of the wavelets in (a) and of the noise estimate; (c) Spectral ratio curve for the spectra in (b).

pling effects include instrument package rocking induced by shear-waves, resulting in enhancement of the spectra near the resonance frequency. To have complete confidence in our estimates of sediment Q_β from horizontal geophone OBS data, we need to know that the effects of coupling resonance are linear for the coda amplitude and spectral content of *PS* and *PSSS*. Linear effects will not bias our estimated Q_β because our numerical experiments showed that the source wavelet is practically self-canceling in both the SR and PAR methods. Cross-coupling from vertical seismic motion to horizontal geophone signals may also affect the Q_β estimates, although Sutton et al. (1981) determined that this is not a problem for this instrument. High amplitude signals will be more strongly affected if the resonance effect is non-linear, with soft clipping of the signal the most likely result. However, the similarity of the spectra of *PS* and *PSSS* noted above leads us to conclude that the coupling effects are linear within the dynamic range of the instrument. In any case, our clipping experiments on synthetic data indicate that soft-clipping effects should not significantly affect the Q_β estimates.

In Fig. 2.17b, the fall-off in energy at frequencies less than 5 Hz may be due to interference by Scholte-waves generated by earlier shots, gradient induced shear-compressional wave coupling (Fryer, 1981), or source characteristics. The divergence of the *PS* and *PSSS* spectra below 5 Hz results in distortion of the spectral ratio curve (Fig. 2.17c); consequently we do not use that portion of the SR curve in our least-squares estimate for this trace. A linear least-squares estimate of Q_β was obtained using frequencies within the [5,18] Hz band that met the 3 dB acceptance criteria discussed above.

In Table 2.6 we list the SR and PAR results for OBS data traces 1-7 from Fig. 2.3. We believe these traces are relatively free of interference and clipping effects. Figure 2.18 shows the wavelet spectra for these traces, and Fig. 2.19 shows their SR

TABLE 2.6. Results of spectral ratio and peak amplitude ratio analysis of OBS data traces 1-7. BW is the bandwidth in which the least-squares spectral ratio Q_β estimate (Q_{SR}), with associated intercept I_{SR}, was obtained; t_{PS} and t_{PSSS} are the arrival times of the respective phases; and $\overline{f}$ is the average of the centroids of their spectra between 3 and 20 Hz used in obtaining the peak amplitude ratio Q_β estimates (Q_{PAR}). At the bottom are results for the spectral average of the nearest five traces.

Range (km)	t_{PS} (s)	t_{PSSS} (s)	Window (s)	BW (Hz)	$\overline{f}$ (Hz)	Q_{PAR}	I_{SR}	Q_{SR}
0.027	5.68	9.59	0.69	3.1,17.8	10.0	163	0.121	110 ± 20
0.238	5.67	9.59	0.56	6.2,17.5	10.7	143	0.332	105 ± 25
0.405	5.67	9.49	0.69	5.0,17.8	9.7	100	0.361	97 ± 10
0.576	5.68	9.49	0.63	3.1,15.0	10.4	141	-0.027	100 ± 17
0.747	5.68	9.50	0.50	5.9,17.8	10.0	136	0.053	102 ± 15
0.906	5.70	9.63	0.50	3.1,13.8	11.3	310	-0.443	135 ± 31
1.077	5.70	9.68	0.50	6.2,17.5	11.4	206	-0.075	133 ± 23
Spectral Average				3.1,17.2	10.0	122	0.245	97 ± 11

curves. Variations in the arrival time of *PSSS* in Fig. 2.3 may be due to slightly different slantpaths for the downward P and upward S, possibly caused by non-horizontal layering within the sediments or basement topography. Interference, clipping, or an increase in signal generated noise energy was inferred wherever the spectral estimates for *PSSS* are greater than for *PS*. These spectral bands (the flat, truncated segments of the SR curves in Fig. 2.19) were excluded from the SR curves and thus from the least-squares estimation of Q_β. Window length and position were adjusted to obtain *PSSS* spectra with approximately the same shape as the *PS* spectra. In the peak amplitude ratio analysis, we estimated $\mathcal{GR}_\tau$ with $\exp[I_{SR}]$, and used $\bar{f}$ for f_3 in equation (17) while neglecting the second term on the r.h.s. of (17).

Some trace-to-trace variation is seen in the linear least-squares SR Q_β estimates of Table 2.6. Although the degree of signal clipping in the data is unknown, the spectral ratio tests on synthetic data above indicate that relatively large amounts of clipping will not affect the SR estimates in the [3,18] Hz band used in this analysis. The efficiency of P-to-S conversion generally increases with range up to the sediment/basement shear-wave critical angle, increasing the amplitude of the *PS* arrival and generally resulting in more severe clipping of that phase as the range increases. Consequently, we reduced the length of the time window at greater offsets in an effort to exclude the most severely clipped pulses in the *PS* coda. Not surprisingly, we still obtained significantly higher Q_β estimates from the two farthest traces in Table 2.6 than from the five nearest traces. The increase in $\bar{f}$ at 0.906 km also suggests greater signal clipping. Holes in the spectra of *PSSS*, such as those seen at about 5 Hz in Figures 2.18b and 2.18f, are probably caused by interference; they result in holes in the SR curves (Figures 2.19b and 2.19f) which we exclude from the least-squares estimates. These interference and clipping effects may account for the variation observed in the spectral ratio results for the five nearest traces in Table 2.6. Also, as the

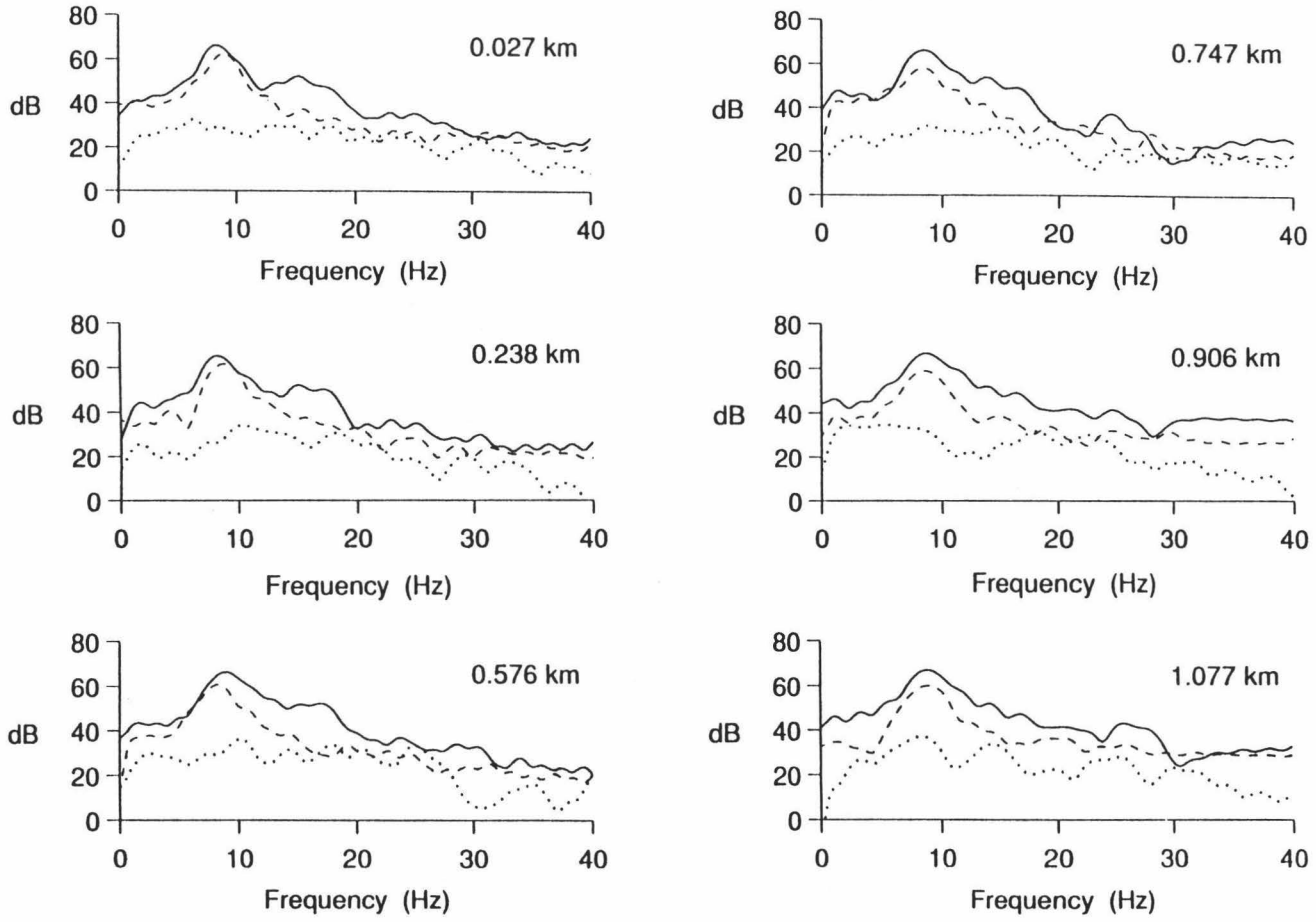

Figure 2.18: Amplitude spectra of the *PS* (solid), *PSSS* (dashed), and noise estimate (dotted) wavelets for the OBS data.

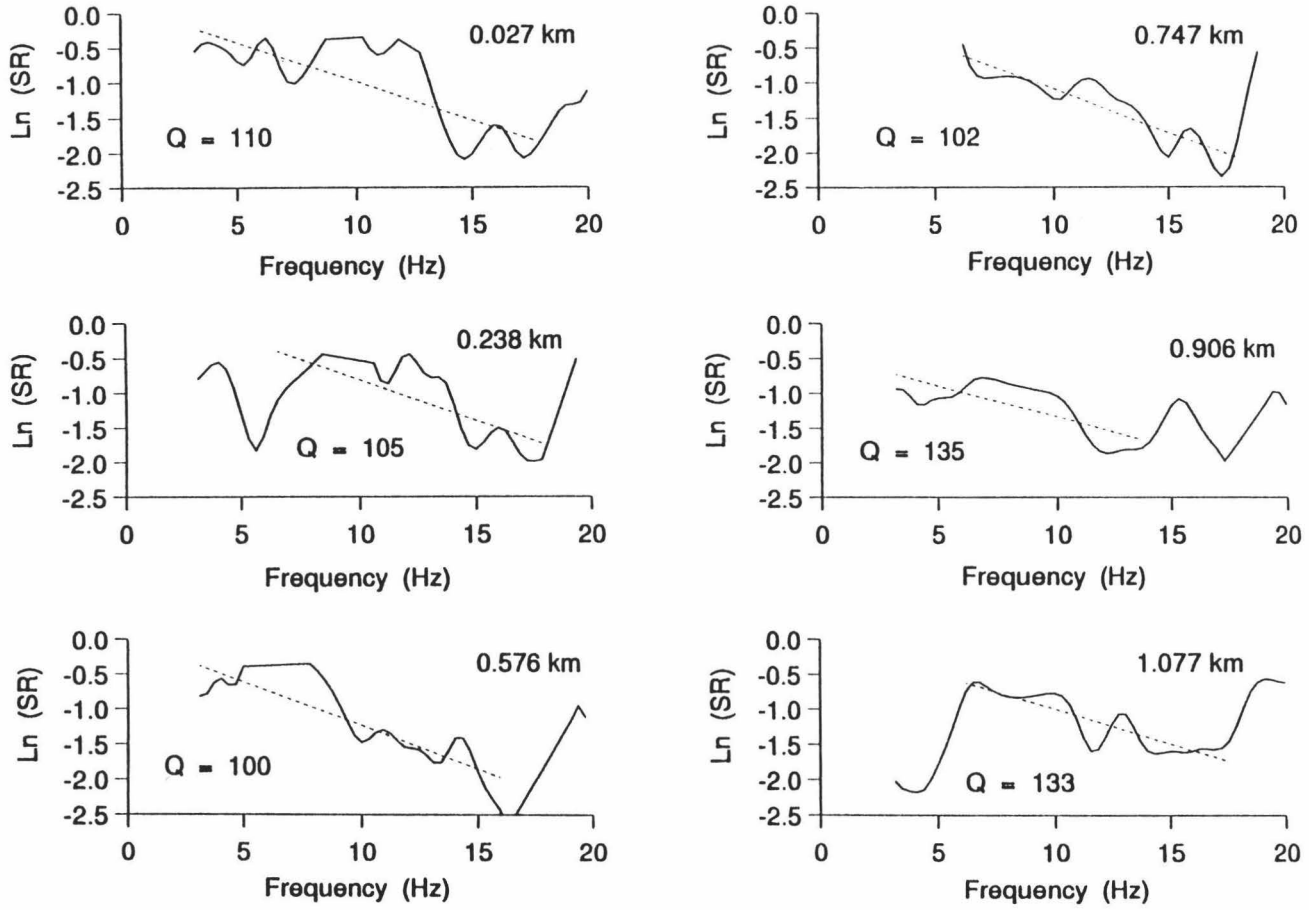

Figure 2.19: Spectral ratio curves for the spectra in Fig. 2.18. The dashed lines are the least-squares fits over the band in which the Q_β estimate was obtained.

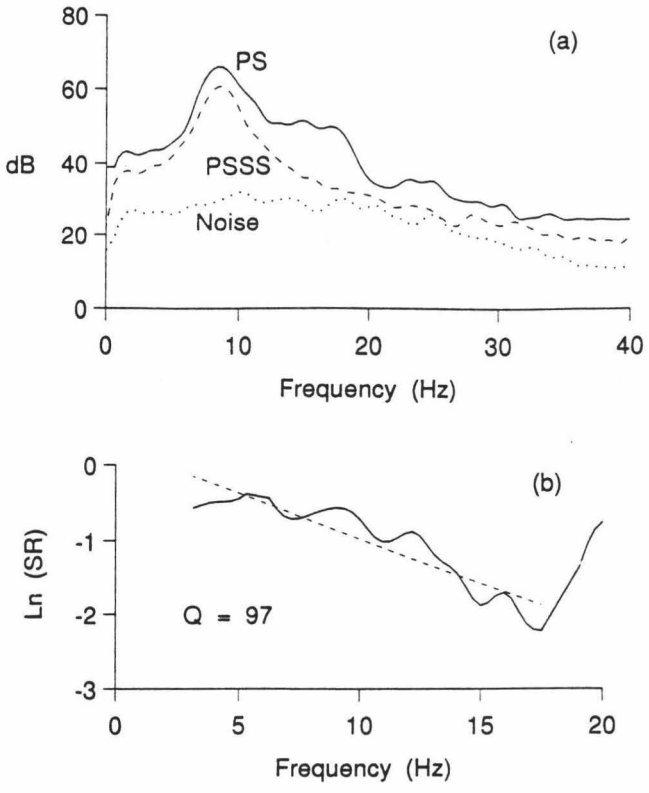

Figure 2.20: (a) Spectral average of the *PS* (solid), *PSSS* (dashed), and noise estimate (dotted) wavelets for the five nearest OBS data traces. (b) Spectral ratio curve for the spectra in (a).

spectra in Fig. 2.18 show, the noise energy varies from trace to trace. If the in-trace noise variability is as great as its trace-to-trace variability, then the noise estimate may not accurately represent the noise level in the windows selected.

To average these effects and thus lower the statistical variance of the spectral estimates, we computed arithmetic (Fig. 2.20a) and median averages of the spectral estimates for the nearest five traces in Table 2.6 prior to taking their ratios. Both averaging methods gave similar results, although the median average spectra and spectral ratios were noticeably less smooth. We obtained $Q_\beta = 97 \pm 11$ over the [3,17.2] Hz band for the arithmetic spectral average in Fig. 2.20b using the linear least-squares procedure.

The peak amplitude ratio results, Q_{PAR} in Table 2.6, are consistently higher than the Q_{SR} estimates, as would be expected if *PS* were clipped. The spectral average Q_{PAR} estimate of $Q_\beta = 122$ can be considered an upper bound. Note that there is little difference between Q_{SR} and Q_{PAR} at 0.405 km, suggesting that clipping for this trace is not as severe as the other traces, and that this trace probably gives the most reliable individual estimate of sediment Q_β.

2.8 CONCLUSIONS

We have shown that spectral ratio and peak amplitude ratio methods can give accurate estimates of sediment Q_β from converted shear-wave reflections on horizontal component synthetic seismograms. Tests on synthetic data suggest that moderate amounts of noise and signal clipping do not introduce significant error in spectral ratio estimates of Q_β. Q_β estimates within 25% of the model can be obtained with the addition of up to 7% noise energy. However, the frequency dependence of sediment Q_β cannot be determined by spectral methods for narrow bandwidth data when a small amount of noise is present.

Our methods were applied to horizontal component OBS data collected over soft sediments at a deep water site in the northwest Pacific. The spectral ratio method gave Q_β estimates between 97 and 110 (corresponding to an attenuation, α, between 0.281 and 0.248 dB/λ) using the linear least-squares procedure. The spectral average of these traces yields a Q_β estimate of 97 ± 11. We suggest that the spectral ratio method can give effective Q_β estimates for the entire sediment column with better than 10% accuracy from converted shear-wave reflections for broadband horizontal component OBS data in areas where *PS* and *PSSS* are observed. This accuracy is not greatly degraded by modest amounts of noise and signal clipping.

2.9 REFERENCES

Aki, K. and Richards, P.G., 1980. *Quantitative Seismology, Vol.* **I**, W. H. Freeman and Company, San Francisco.

Banik, N.C., Lerche, I., and Shuey, R.T., 1985. Stratigraphic filtering, Part I: Derivation of the O'Doherty-Anstey formula, *Geophysics,* **50**, 2768-2774.

Biot, M.A., 1956. Theory of propagation of elastic waves in a fluid-saturated porous solid. I. Low frequency range, *J. Acoust. Soc. Am.,* **28**, 168-178.

Byrne, D.A., Sutton, G.H., Blackinton, J.G., and Duennebier, F.K., 1983. Isolated sensor ocean bottom seismometer, *Mar. Geophys. Res.,* **5**, 437-449.

Duennebier, F.K., Lienert, B., Cessaro, R., Anderson, P., and Mallick, S., 1987. Controlled-source seismic experiment at Hole 581-C, in *Init. Repts. DSDP,* **88**, pp 105-125, eds. Duennebier, F.K., Stephen, R., Gettrust, J.F., et al., Washington (U.S. Govt. Printing Office).

Fryer, G.J., 1981. Compressional-shear wave coupling induced by velocity gradients in marine sediments, *J. Acoust. Soc. Am.,* **69**, 647-660.

Futterman, W.I., 1962. Dispersive body waves, *J. Geophys. Res.,* **67**, 5279-5291.

Hamilton, E.L., 1976a. Sound attenuation as a function of depth in the sea floor, *J. Acoust. Soc. Am.,* **59**, 528-535.

Hamilton, E.L., 1976b. Attenuation of shear waves in marine sediments, *J. Acoust. Soc. Am.,* **60**, 334-338.

Hamilton, E.L., 1980. Geoacoustic modeling of the sea floor, *J. Acoust. Soc. Am.,* **68**, 1313-1340.

Harrison, C.H. and Cousins, P.L., 1985. A study of propagation loss dependence on sediment layer thickness using the Fast Field Program, in *Ocean Seismo-Acoustics: Low Frequency Underwater Acoustics*, pp 139-148, eds. Akal, T. & Berkson, J.M., Plenum Press, New York.

Hines, W.W. and Montgomery, D.C., 1980. *Probability and Statistics in Engineering and Management Science*, John Wiley & Sons, New York.

Hughes, S.J., Ellis, D.D., Chapman, D.M.F., and Staal, P.R., 1990. Low frequency acoustic propagation loss in shallow water over hard-rock seabeds covered by a thin layer of elastic-solid sediment, *J. Acoust. Soc. Am.,* **88**, 283-297.

Jacobson, R.S., 1987. An investigation into the fundamental relationships between attenuation, phase dispersion, and frequency using seismic refraction profiles over sedimentary structures, *Geophysics,* **52**, 72-87.

Jacobson, R.S., Shor, G.G., Jr., and Dorman, L.M., 1981. Linear inversion of body wave data - Part II: Attenuation versus depth using spectral ratios, *Geophysics,* **46**, 152-162.

Jannsen, D., Voss, J. and Theilen, F., 1985. Comparison of methods to determine Q in shallow marine sediments from vertical reflection seismograms, *Geophys. Prosp.,* **33**, 479-497.

Jensen, F.B. and Schmidt, H., 1986. Shear properties of ocean sediments determined from numerical modeling of Scholte-wave data, in *Ocean Seismo-Acoustics: Low Frequency Underwater Acoustics*, pp 683-692, eds. Akal, T. & Berkson, J.M., Plenum Press, New York.

Johnston, D.H. and Toksöz, M.N., 1981. Seismic wave attenuation - definition and terminology, in *Seismic Wave Attenuation*, pp 1-5, eds. Toksöz, M.N. & Johnston, D.H., SEG Geophysics reprint series No. **2**, Tulsa.

Kanamori, H. and Anderson, D.L., 1977. Importance of physical dispersion in surface wave and free oscillation problems: Review, *Rev. Geophys. Space Phys.*, **15**, 105-112.

Kjartansson, E., 1979. Constant Q-wave propagation and attenuation, *J. Geophys. Res.*, **84**, 4737-4748.

Lerche, I. and Menke, W., 1986. An inversion method for separating intrinsic and apparent attenuation in layered media, *Geophys. J. Roy. Ast. Soc.*, **87**, 333-347.

Liu, H.-P., Anderson, D.L., and Kanamori, H., 1976. Velocity dispersion due to anelasticity; Implications for seismology and mantle composition, *Geophys. J. Roy. Astr. Soc.*, **47**, 41-58.

Mallick, S. and Frazer, L. N., 1987. Practical aspects of reflectivity modeling, *Geophysics,* **52**, 1355-1364.

Mallick, S. and Frazer, L. N., 1988. Rapid computation of multi-offset vertical seismic profile synthetic seismograms for layered media, *Geophysics,* **53**, 479-491.

Mavko, G.M. and Nur, A., 1979. Wave attenuation in partially saturated rocks, *Geophysics,* **44**, 161-178.

Menke, W., 1983. A formula for the apparent attenuation of acoustic waves in randomly layered media, *Geophys. J. Roy. Astr. Soc.*, **75**, 541-554.

Menke, W. and Dubendorff, B., 1985. Discriminating intrinsic and apparent attenuation in layered rock, *Geophys. Res. Lett.*, **12**, 721-724.

O'Connell, R.J. and Budiansky, B., 1978. Measures of dissipation in viscoelastic media, *Geophys. Res. Lett.*, **5**, 5-8.

O'Doherty, R.F. and Anstey, N.A., 1971. Reflections on amplitudes, *Geophys. Prosp.*, **19**, 430-458.

Papoulis, A., 1962. *The Fourier Integral and its Applications.* McGraw-Hill, New York.

Richards, P.G. and Menke, W., 1983. The apparent attenuation of a scattering medium, *Bull. Seism. Soc. Am.,* **73**, 1005-1021.

Schoenberger, M. and Levin, F.K., 1974. Apparent attenuation due to intrabed multiples, *Geophysics,* **39**, 298-291.

Schoenberger, M. and Levin, F.K., 1978. Apparent attenuation due to intrabed multiples, II, *Geophysics,* **43**, 730-737.

Spencer, T.W., Edwards, C.M., and Sonnad, J.R., 1977. Seismic wave attenuation in nonresolvable cyclic stratification, *Geophysics,* **42**, 939-949.

Spencer, T.W., Sonnad, J.R., and Butler, T.M., 1982. Seismic Q: Stratigraphy or dissipation?, *Geophysics,* **47**, 16-24.

Spudich, P.K.P. and Orcutt, J.A., 1980. Petrology and porosity of an oceanic crustal site: Results from wave form modeling of seismic refraction data, *J. Geophys. Res.,* **85**, 1409-1433.

Stoll, R.D., 1974. Acoustic waves in saturated sediments, in *Physics of Sound in Marine Sediments*, pp 9-39, ed. Hampton, L., Plenum Press, New York.

Stoll, R.D., 1985. Marine sediment acoustics, *J. Acoust. Soc. Am.,* **77**, 1789-1799.

Stoll, R.D. and Bryan, G.M., 1970. Wave attenuation in saturated sediments, *J. Acoust. Soc. Am.,* **47**, 1440-1447.

Strick, E., 1967. The determination of Q, dynamic viscosity and transient creep curves from wave propagation measurements, *Geophys. J. Roy. Astr. Soc.,* **13**, 197-218.

Strick, E., 1970. A predicted pedestal effect for pulse propagation in constant-Q solids, *Geophysics,* **35**, 387-403.

Sutton, G.H., Lewis, B.T.R., Ewing, J., Duennebier, F.K., Iwataki, B., Tuthill, J.D., et al., 1980. *Lopez Island Ocean Bottom Seismometer Intercomparison Experiment*, Hawaii Inst. of Geophys. Tech. Rep. HIG-80-4, Hawaii Inst. Geophys., Honolulu.

Sutton, G.H., Duennebier, F.K., Iwataki, B., Tuthill, J.D., 1981. An overview and general results of the Lopez Island OBS Experiment, *Mar. Geophys. Res.* **5**, 3-34.

Sutton, G.H. and Duennebier, F.K., 1987. Optimum design of ocean bottom seismometers, *Mar. Geophys. Res.* **9**, 47-65.

Toksöz, M.N. and Johnston, D.H., eds., 1981. *Seismic Wave Attenuation*, SEG Geophysics reprint series No. **2**, Tulsa.

Tonn, R., 1991. The determination of seismic quality factor Q from VSP data: A comparison of different computational methods, *Geophys. Prospect.*, **39**, 1-27.

Vidmar, P.J., 1980a. The effect of sediment rigidity on bottom reflection loss in a typical deep sea sediment, *J. Acoust. Soc. Am.,* **68**, 634-638.

Vidmar, P.J., 1980b. Ray path analysis of sediment shear wave effects on bottom reflection loss, *J. Acoust. Soc. Am.,* **68**, 639-648.

Walsh, J.B., 1966. Seismic attenuation in rock due to friction, *J. Geophys. Res.,* **71**, 2591-2599.

White, R.S. and Stephen, R.A., 1980. Compressional to shear wave conversion in oceanic crust, *Geophys. J. Roy. Astr. Soc.,* **63**, 547-565.

Chapter 3

SEDIMENT SHEAR Q FROM INSTANTANEOUS PHASE: THE Q–GRAM METHOD

3.1 SUMMARY

The width of a seismic pulse increases monotonically with distance and with Q^{-1}. Estimates of Q from pulse width measurements are often not robust for oscillatory arrivals or for impulsive arrivals in the presence of noise. We present a method to estimate Q from two arrivals using measurements of any signal attribute, $\overline{\xi}$, that is sensitive to propagation loss. The propagation loss is defined as the change in $\overline{\xi}$ divided by the difference in traveltime between the arrivals. The first data arrival is used as the reference wavelet. The Q–gram method is based on propagating the reference wavelet with a plane-wave Q–propagator for various values of Q^{-1}. The Q–propagator includes a dispersion relation and the measured difference in traveltime between the data arrivals. The plot of synthetic propagation loss between the reference and propagated wavelets, versus Q^{-1}, is called a Q–gram. The Q-gram, together with the measured propagation loss of the data, gives the Q of the data.

The averaged instantaneous frequency $\overline{f}$ and the averaged instantaneous pulse width $\overline{\tau}$ make good signal attributes. Tests on synthetic seismograms show that

the Q–gram method, using either $\overline{f}$ or $\overline{\tau}$ for $\overline{\xi}$, is applicable to both impulsive and oscillatory arrivals and is relatively robust with regard to noise, phase changes, and signal clipping.

We apply the Q–gram method to horizontal component airgun ocean bottom seismometer (OBS) data using the basement converted shear-wave reflection, *PS*, as the first arrival and *PSSS* as the second arrival. We estimate Q_β, the effective sediment shear-wave Q, with an $\overline{f}$–type Q–gram and a $\overline{\tau}$–type Q–gram for the *PS* and *PSSS* sediment shear-wave reflections. The data indicate $Q_\beta \approx 75 \pm 15$, in agreement with results from the application of the spectral ratio method using windows that exclude interfering arrivals identified by means of the instantaneous frequency.

Key words: Attenuation, instantaneous phase, instantaneous frequency, sediment shear-wave Q, airgun horizontal OBS data

3.1.1 Introduction

Anelasticity in earth materials results in the attenuation and dispersion of seismic waves. Attenuation, characterized by the dimensionless intrinsic quality factor Q, causes a propagating wavelet to broaden and decrease in amplitude. Reliable estimates of attenuation are necessary for accurate interpretation of seismograms. When corrected for geometric spreading and reflection coefficients, seismic waves decay in amplitude like $e^{-\alpha x}$ in which x is the source-receiver distance and α is the attenuation. Attenuation is thus an intrinsic property of the material through which the waves propagate. Attenuation measured from field data, however, includes apparent losses resulting from scattering in addition to intrinsic losses due to anelasticity.

To estimate Q from data, a change in amplitude, spectral content, or pulse width must be measured between two arrivals of the same seismic signal. The magnitudes

of the change in these signal attributes depend on traveltime, path characteristics (including scattering), and intrinsic Q. As Q increases, the change in a signal attribute for a particular path decreases. Estimates of Q are sensitive to noise both for very low Q, where the second arrival drops into the noise, and for very high Q, where the change in waveform between the two arrivals is slight. Since α is generally small, only the first two terms in the series expansion of $e^{-\alpha x}$ are significant, and the amplitude decay is effectively linear in α. However, since $\alpha \propto Q^{-1}$, the amplitude decay is nonlinear in Q. Consequently, α or Q^{-1} is a more useful parameter for inversion.

A variety of methods are available for Q estimation. These include the spectral ratio (e.g. *Bath*, 1974), rise time (*Gladwin and Stacey*, 1974), analytic signal (*Engelhard et al.*, 1986), and waveform modeling (*Jannsen et al.*, 1985) methods. The presence of noise severely limits the reliability of all methods (see e.g. *Tonn*, 1991). However, both Jannsen et al. (1985) and *Tonn* (1991) found that waveform modeling methods are superior in the presence of noise.

Here we use as signal attributes the averaged instantaneous frequency $\overline{f}$ and the averaged instantaneous pulse width $\overline{\tau}$, where the averaging is over the duration of the signal. It can be seen that $\overline{\tau}$ and $\overline{f}$ are just sophisticated definitions of pulse width and reciprocal pulse width, respectively. The Q–gram method can also be used with conventional definitions of pulse width, but, as we show later, $\overline{f}$ and $\overline{\tau}$ are more robust measures of pulse width for oscillatory signals. The quantities $\overline{\tau}$ and $\overline{f}$ are obtained from the instantaneous phase using complex trace analysis (e.g. *Kanasewich*, 1981; Chapter 21). Propagation loss reference curves, called Q–grams, are constructed by propagating the reference data wavelet with a Q–propagator for a time equal to the traveltime difference between the data arrivals, and then measuring the propagation loss between the reference and propagated wavelets. The Q–propagator is a plane-wave operator that includes an appropriate dispersion relation.

The Q–gram method is best shown in the context of actual data. We first present the theory. Then we test the method on reflectivity synthetic seismograms modeled from horizontal component OBS data collected in the northwest Pacific at DSDP Hole 581C (*Duennebier et al.*, 1987). Then we apply the procedure to the actual OBS data to estimate Q_β, the effective sediment shear-wave Q, from *PS* and *PSSS* shear reflections, comparing the results with those obtained by *Bromirski et al.* (1992a) using spectral ratios. Revised spectral ratio estimates, using shorter windows to reject interfering phases identified by means of the instantaneous frequency, agree well with our Q–gram result.

3.2 THEORY

To estimate Q, the propagation loss between two arrivals must be measured. Signal attributes, $\overline{\xi}$, that are sensitive to propagation loss can be obtained from the instantaneous phase. The instantaneous phase $\phi(t)$ of a real signal $s(t)$ is obtained from its analytical signal $\sigma(t)$. The signal $s(t)$ can be either a field record or a synthetic seismogram. From complex trace analysis, $\sigma(t)$ is defined as

$$\sigma(t) \;=\; a(t)\, e^{i\phi(t)} \;=\; s(t) \;+\; i\,\hat{s}(t) \tag{1}$$

where $\hat{s}(t)$ is the Hilbert transform of $s(t)$ and $a(t)$ is the instantaneous amplitude (*Taner et al.*, 1979). We obtain $\hat{s}(t)$ from the inverse Fourier transform of $+\,i\,sgn(\omega)\overline{s}(\omega)$, with $\overline{s}(\omega) = \int dt\; s(t)e^{i\omega t}$. We choose the positive sign for the Hilbert transform so that $\phi(t)$, which usually must be unwrapped, increases with time. Then

$$\phi(t) \;=\; tan^{-1}\left[\hat{s}(t)/s(t)\right] \tag{2}$$

and

$$a(t) \;=\; |\sigma(t)| \;=\; \left[s(t)^2 \;+\; \hat{s}(t)^2\right]^{1/2} \;, \tag{3}$$

the amplitude envelope of the real signal $s(t)$. From $\phi(t)$, the instantaneous frequency $f(t)$ and instantaneous pulse width $\tau(t)$ are given by

$$f(t) \;=\; \frac{1}{2\pi}\,\frac{d\phi(t)}{dt} \;=\; \frac{1}{\tau(t)} \quad . \tag{4}$$

Here $d\phi/dt$ is obtained from equation (2) either by numerical differentiation of $\phi(t)$ or from

$$\frac{d\phi}{dt} \;=\; \frac{s\dot{\hat{s}} \;-\; \hat{s}\dot{s}}{s^2 \;+\; \hat{s}^2} \quad , \tag{5}$$

in which the *dot* indicates a time derivative obtained by either numerical differentiation of $s(t)$, or from the inverse Fourier transform of $-i\omega\ \overline{s}(\omega)$. Note that phase unwrapping is not required if $d\phi/dt$ is computed with equation (5).

Let $\xi(t)$ be either of the quantities $-f(t)$ or $\tau(t)$. (The minus sign on $f(t)$ is needed to obtain an $\overline{f}$-type Q-gram with a positive slope.) We define $\overline{\xi} = \overline{\xi}(T)$ for the signal with arrival time T by

$$\overline{\xi}(T) \;=\; \frac{1}{\int_{t_a}^{t_b} dt\ [a(t)]^n}\int_{t_a}^{t_b} dt\ \xi(t)\ [a(t)]^n \quad . \tag{6}$$

When $n = 2$, $\xi(t)$ is modulated by the instantaneous energy in the signal. We define the arrival time T by a similar weighted average,

$$T \;=\; \frac{1}{\int_{t_a}^{t_b} dt\ [a(t)]^n}\int_{t_a}^{t_b} dt\ t\ [a(t)]^n \quad , \tag{7}$$

in which t_a and t_b are the beginning and end of the signal and n is a constant (*Bromirski et al.*, 1993).

Suppose we record an arrival $P(x,t)$ at distances x_1 and x_2. Let $P_1(t)$ and $P_2(t)$ be the two recordings, with arrival times T_1 and T_2 and signal attributes $\overline{\xi}_1$ and $\overline{\xi}_2$, respectively. The propagation loss Ψ over the path from x_1 to x_2 is then defined by

$$\Psi(\overline{\xi}_1, \overline{\xi}_2) \;=\; \frac{\overline{\xi}_2 \;-\; \overline{\xi}_1}{\Delta T} \tag{8}$$

in which $\Delta T = T_2 - T_1$ is the observed traveltime difference between locations x_1 and x_2. Note that Ψ is dimensionless when using $\overline{\xi} = \overline{\tau}$, but Ψ has units of s^{-2} when $\overline{\xi} = \overline{f}$. Also, since $\dot{\phi}$ does not depend on the amplitude of the signal, the Q–gram method using signal attributes $\overline{f}$ and $\overline{\tau}$ is independent of signal amplitude.

The definitions of $\overline{\xi}$ and T given by equations (6) and (7) are robust for both impulsive and oscillatory signals. Although the numerator in equation (8) may be evaluated in a single integration, separate computation of the $\overline{\xi}_1$ and $\overline{\xi}_2$ integrals eliminates the problem of time synchronization between P_1 and P_2, and also allows modulation by their respective $a(t)$.

Clearly, Ψ depends on the unknown Q of the medium and the propagation path between locations x_1 and x_2. To estimate this Q, we propagate P_1 from x_1 to x_2 using a plane-wave propagator $\mathcal{Q}$. We derive $\mathcal{Q}$ using *Kjartansson's* (1979) constant–Q complex velocity, $c(\omega)$, given by

$$c(\omega) \;=\; c_0 \left(\frac{-i\omega}{\omega_0}\right)^{\gamma} \quad . \tag{9}$$

The minus sign in the definition is needed for consistency with our Fourier transform convention. Note that c_0 is the phase velocity at $Q = \infty$. Also $c_{\rm m}$, the seismic phase velocity at ω_0, is given by $\quad c_{\rm m} = c_0 / \cos\left(\frac{\pi\gamma}{2}\right)$, and ω_0 is given by $\quad \omega_0 = 2\pi f_0$ with f_0 the reference frequency. The Q dependence appears in γ defined by $\quad \gamma = \frac{1}{\pi}\tan^{-1}\left(\frac{1}{Q_{\rm m}}\right)$, so that $\gamma \ll 1$ for $Q > 20$. Then $c_{\rm m}$, f_0 and $Q_{\rm m}$ are the input model parameters in synthetic seismogram computations. The traveltime $T(\omega)$ can then be written in terms of slowness $S(\omega)$, obtained from the reciprocal of equation (9), as

$$T(\omega) \;=\; X\, S(\omega) \;=\; X\, S_0 \left(\frac{i\omega_0}{\omega}\right)^{\gamma} \;=\; X\, S_0 \left(\frac{\omega_0}{\omega}\right)^{\gamma} \left[cos(\frac{\pi\gamma}{2}) + i\, sin(\frac{\pi\gamma}{2})\right]$$

where X is the unknown path length and $S_0 = 1/c_0$. This gives

$$T(\omega) \;=\; XS_0\, cos\left(\frac{\pi\gamma}{2}\right) \left|\frac{\omega_0}{\omega}\right|^{\gamma} \left[1 \;+\; i\, tan\left(\frac{\pi\gamma}{2}\right)\right] \quad . \tag{10}$$

Taking $T_m = Re(T(\omega_0)) = XS_0 \cos(\pi\gamma/2)$ to be the measurable traveltime, the plane-wave propagator $\mathcal{Q}(\omega)$ is given as

$$\mathcal{Q}(\omega) = \exp\left\{i\omega\Delta T\left|\frac{\omega_0}{\omega}\right|^{\gamma}\left[1 + i\tan\left(\frac{\pi\gamma}{2}\right)\right]\right\} \tag{11}$$

where ΔT is the traveltime difference between data arrivals P_1 and P_2 obtained using equation (7). Defining $\mathcal{Q}$ in terms of ΔT eliminates the need to estimate both the path length and seismic phase velocity when computing the quantity $\overline{\xi}_2'$ for the propagated wavelet below. Different plane-wave propagators may be obtained using other dispersion relations.

To construct the Q–gram, we first compute $\overline{\xi}_1$ for the reference wavelet P_1 with equation (6), and the traveltimes T_1 and T_2 using equation (7). We then use $\mathcal{Q}$ to propagate P_1 a time $\Delta T = T_2 - T_1$, obtaining a synthetic P_2 called P_2'. The *primes* designate quantities that use the propagated wavelet. Thus in the frequency domain

$$P_2' = \mathcal{Q}P_1 \ .$$

From P_2' we calculate $\overline{\xi}_2'$ and the arrival time T_2'. Then using $\overline{\xi}_2'$ and $\overline{\xi}_1$ in equation (8) gives the predicted propagation loss $\Psi'(Q^{-1}) = [\overline{\xi}_2'(Q^{-1}) - \overline{\xi}_1]/\Delta T$. The plot of Ψ' versus Q^{-1} is the Q-gram.

Once the Q-gram is constructed, we measure $\overline{\xi}_2$ for the later arrival P_2 from the data and obtain Ψ for the data. The corresponding Q estimate is then obtained from the Q-gram by linear interpolation between the nearest values of Ψ' on the Q–gram.

Other definitions of $\overline{\xi}$ and T that give different measures of propagation loss may be used to construct other types of Q-gram. For example, $\overline{\xi}$ could be defined as the rise-time (*Gladwin and Stacey*, 1974) and T could be defined as the arrival time of maximum slope. This type of Q–gram is examined below in section **4**. The most appropriate definitions of $\overline{\xi}$ and T depend on the characteristics of the wavelets, and

should be determined by tests on the data wavelet P_1. The best definitions give a Q–gram that is smooth and steep.

The Q–gram method is a generalization of the procedure given by *Bromirski et al.* (1992b) to determine the pulse width constant, $C(Q)$. The Q–gram method has the advantage over the analytic signal method (*Engelhard et al.*, 1986) in that the problem of time synchronization between the arrivals is eliminated. Although the construction of a Q–gram may be replaced by an optimization procedure to find Q (e.g. *Jannsen et al.*, 1985), the smoothness and slope of the Q–gram in the neighborhood of Ψ give a visual indication of the reliability of the Q estimate. Poor definitions of $\overline{\xi}$ or T are often obvious from the resulting Q–gram.

While the Q–gram method could be demonstrated using plane-wave synthetics computed with equation (9), it is more useful and less circular to demonstrate the method on actual data. As an intermediate step, we verify the method on exact synthetic seismograms generated for a velocity structure similar to that of our data area.

3.3 APPLICATION

Seismic arrivals can be broadly classified into two groups: impulsive arrivals associated with explosive sources and oscillatory arrivals associated with airgun bubble-pulse oscillations, earthquake sources or multipathing. We demonstrate the Q–gram method on reflectivity synthetic seismograms that model horizontal component OBS data. To illustrate the applicability of the method to both types of sources, we test it on impulse response synthetics and on synthetics filtered with an oscillatory wavelet from the OBS data. The goal is to estimate Q_β, the effective shear–wave Q of the sediments.

The OBS data were obtained in conjunction with the Ocean Sub-bottom Seismometer IV Experiment on DSDP Leg 88 from a 30-liter airgun (*Duennebier et al.*, 1987). The experiment site (Hole 581C) is located in $\sim$ 110 Ma crust about 40 km south of the Hokkaido Trough in the northwest Pacific basin at $43°55.44'N$, $159°47.84'E$. Typical water depth in the area is 5500 m. Single-channel reflection data show pelagic sediments smoothly draped over basaltic crust. Holes drilled at Site 581 on Legs 86 and 88 encountered about 350 m of continuous pelagic siliceous clays; chert bands beginning about 70 m above basement become numerous near the base of the sediments. The analog OBS data were digitized at 80 samples/s, giving a Nyquist frequency of 40 Hz. Navigation, gain, and $R^{0.66}$ spreading corrections were applied.

The horizontal component data from traces at less than 20 km horizontal range, with each trace normalized to the same maximum amplitude, are shown in Fig. 3.1. From the P+S sediment traveltime of about 2.0 s and the sediment thickness of 356 m from drilling, we estimate an average sediment shear–wave velocity, $\bar{c}_\beta$, between 0.185 and 0.205 km/s, assuming the average sediment compressional–wave velocity, $\bar{c}_\alpha$, is between 2.0 and 1.5 km/s. The water wave, W, and the *PS* and *PSSS* converted basement reflections are identified by traveltime curves derived from geometrical ray tracing for a 1–layer sediment model with $c_\alpha = 1.55$ km/s, $c_\beta = 0.198$ km/s. The *PS* arrival travels down through the sediment column as P and converts to S at the sediment/basement interface. The *PSSS* arrival transits the sediment column four times, once as P and three times as S. The trace at 0.41 km, with *PS* and *PSSS* selected for Q estimation, is shown in Fig. 3.2. This is the best trace for analysis as will be shown below. The amplitude spectra (Fig. 3.3), with a $\frac{1}{4}, \frac{1}{2}, \frac{1}{4}$ smoothing function applied, have a dominant frequency of about 9 Hz. Also shown in Fig. 3.3 is the amplitude spectrum for a noise sample with the same length as the wavelets

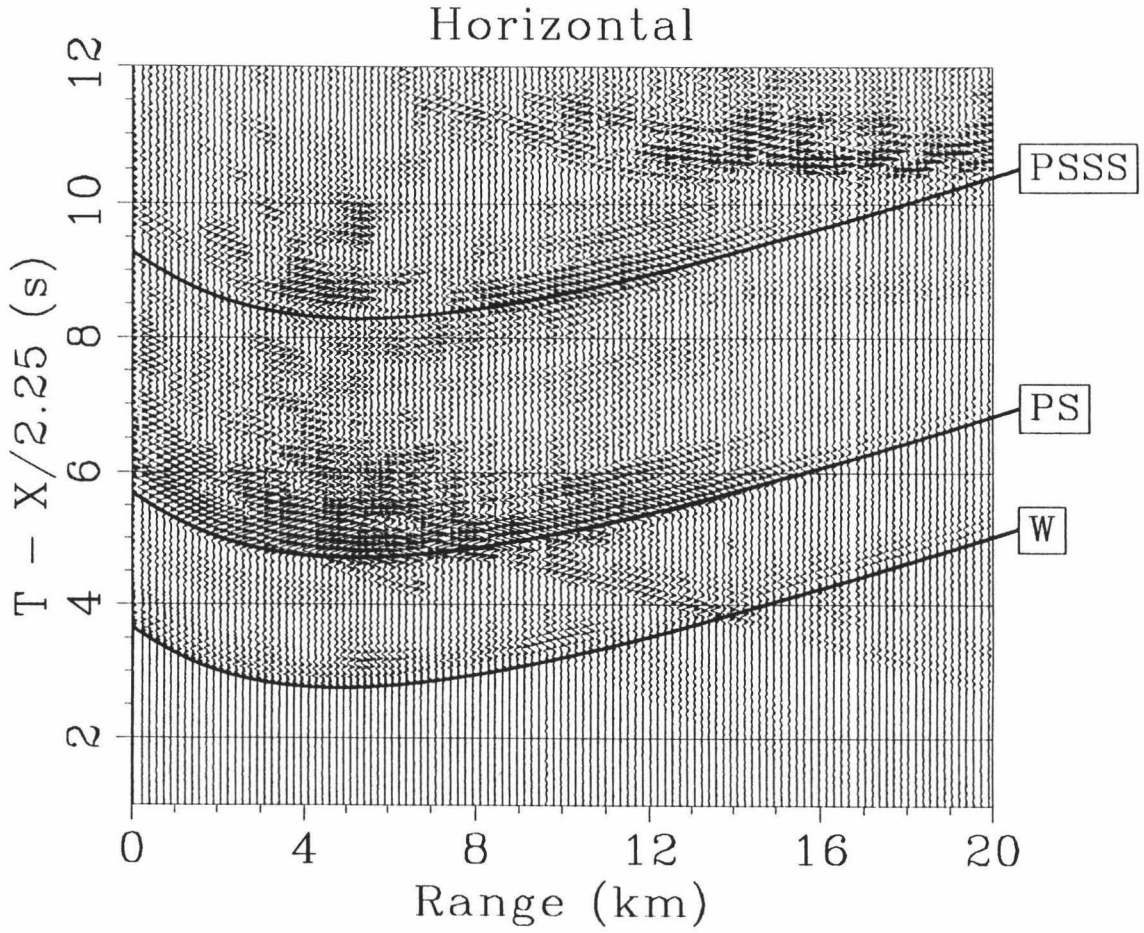

Figure 3.1: Horizontal component OBS data reduced by 2.25 km/s. Traveltime curves identify the water wave W and the converted shear reflections PS and $PSSS$.

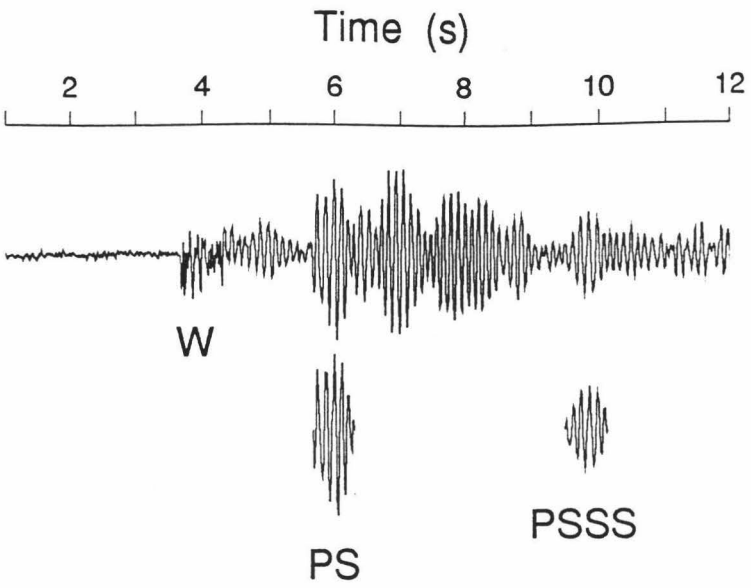

Figure 3.2: Horizontal geophone OBS data at 0.41 km with the *PS* and *PSSS* wavelets extracted.

preceding W. We use *PS* as the reference wavelet in our tests of the Q–gram method.

Basement compressional and shear-wave velocities of 2.25 and 4.25 km/s, respectively, were obtained from the slopes of the *PSS* and *PPS* refraction branches. The high sediment to basement velocity contrast results in near vertical travel of the converted sediment shear reflections. The sediment and basement time–distance and velocity constraints were used to construct a 2–layer sediment model to compute reflectivity synthetic seismograms for our numerical tests below. The synthetics were computed using the reflectivity code of *Mallick and Frazer* (1987). The average intrinsic $Q_\beta \approx 100$ (Table 3.1) for the two sediment layers was determined using the definition of intrinsic Q for an n-layer profile given by *Bromirski et al.* (1992a) as

$$Q_I = \frac{H}{\bar{c}} \left[\sum_{j=1}^{n} \frac{h_j}{c_j Q_j} \right]^{-1} \tag{12}$$

where h_j and c_j are the thickness and seismic phase velocity of the j^{th} layer and H

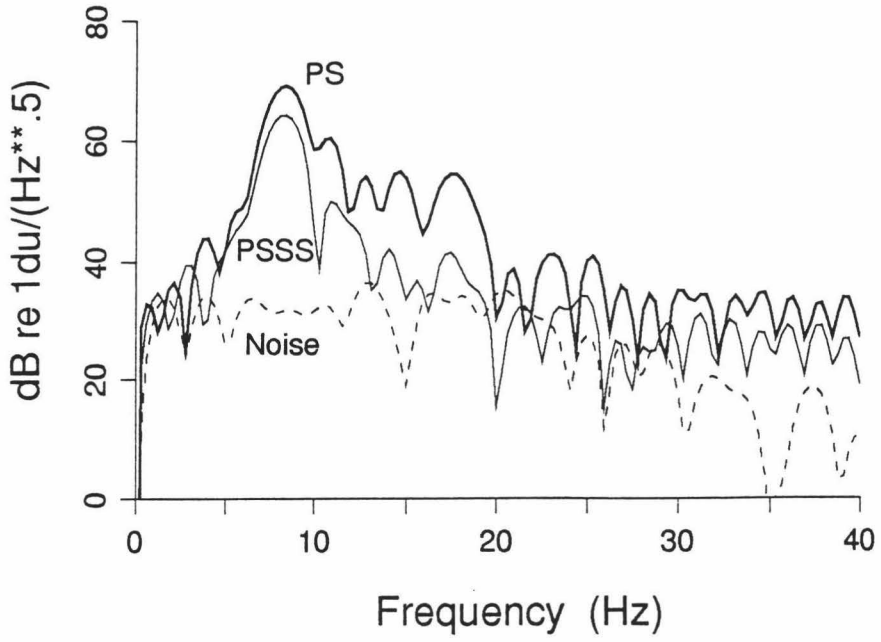

Figure 3.3: Amplitude spectra for *PS* (heavy) and *PSSS* (light) wavelets, and the noise estimate (dashed) for the OBS data trace in Fig. 3.2.

is the total sediment thickness. The average velocity $\bar{c}$ is given by

$$\bar{c} \;=\; H \left[\sum_{j=1}^{n} \frac{h_j}{c_j} \right]^{-1} \quad . \tag{13}$$

The c_j are frequency-dependent velocities computed using equation (9). In discussing our tests on synthetic data, we will say that the error of the Q estimate is the difference between the Q recovered by the method and Q_I given by (12). Note that the low Q_β sediment layer L1a (Table 3.1) dominates the intrinsic Q_β for the sediment column.

To give the wavelets in our Q–gram tests the same reverberative character as the OBS data, we filter the impulse response synthetics with $G(\omega)$ given by

$$G(\omega) \;=\; \frac{W_d(\omega)}{W_i(\omega)}$$

where W_d is the spectrum of the *PS* arrival in the OBS data and W_i is the spectrum of the *PS* arrival in the impulse response synthetics. Synthetics filtered with G will

Table 3.1: Input parameters c_m and Q_m used in computing the synthetic traces in Fig. 3.4a. Velocities are in km/s and densities are in gm/cm^3.

		c_α	Q_α	c_β	Q_β	ρ	h(km)
water		1.5	10000	0.0	0	1.0	5.467
sediments	L1a	1.55	30	0.160	80	1.35	0.200
	L1b	1.75	30	0.295	185	1.75	0.156
basement		4.25	300	2.25	250	2.65	___

be referred to below as *PS*–filtered synthetics. The impulse response and *PS*–filtered synthetic traces are shown in Fig. 3.4a, with the wavelets selected for Q measurements identified. All synthetics were computed with the same sampling interval as the OBS data, 0.0125 s.

3.3.1 Windowing and numerical considerations

The windows selected for signal analysis can significantly affect the Q estimate. For low Q, or when the number of wavelengths between the signals is large, the leading and trailing ends of the later arrival may fall into the noise. Note the amplitude loss from *PS* to *PSSS* in Fig. 3.4a. To reduce the chance of including portions of the arrivals with low signal–to–noise ratio, we set the integration limits t_a and t_b in equations (6) and (7) as the first and last points of $a(t)$ above a certain percentage of the maximum of $a(t)$. This selection criterion allows the integration window to stretch, accommodating the increase in wavelet length with Q^{-1} when constructing the Q-gram. Too low an acceptance level will include undesirable noise. An improperly chosen acceptance level will give a Q-gram with jumps, indicating that the number of cycles included in the integration window has changed.

For our data the difference $\overline{\tau}_2 - \overline{\tau}_1$ for $\tau(t)$ is on the order of 10^{-3} s, and the measurement precision needed for a smooth Q–gram requires interpolation of the wavelets to an effective sampling interval of about 10^{-4} s. Figure 3.4b shows the

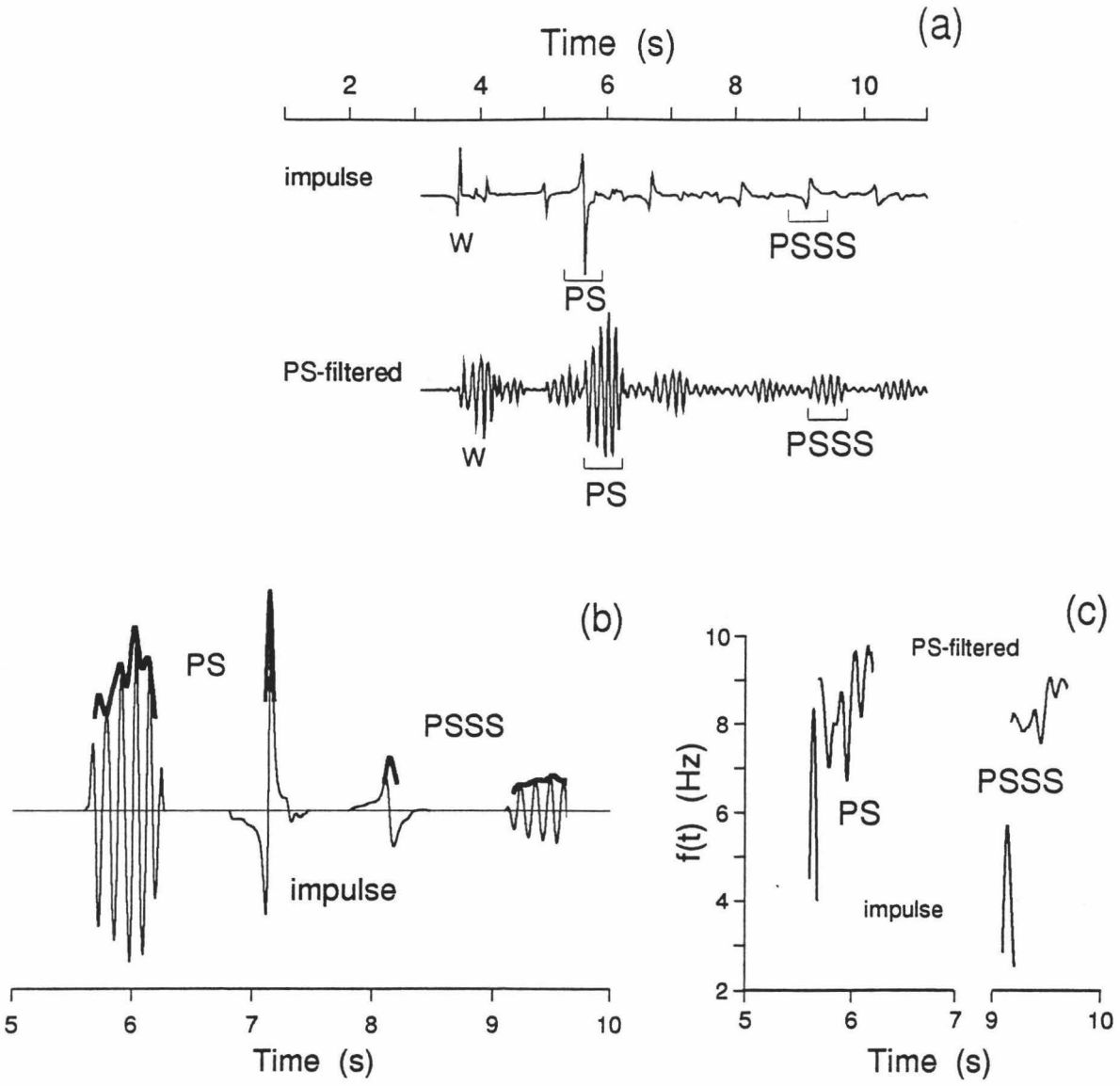

Figure 3.4: (a) Impulse response and *PS*–filtered reflectivity synthetic traces for the model in Table 3.1 with sediment $Q_\beta = 100$. (b) *PS* and *PSSS* wavelets from (a) after FFT interpolation. The impulse response wavelets (center) are offset from their actual arrival times. The instantaneous amplitude (dark line) shows the portions of the wavelets used to obtain the Q_β estimates. (c) Instantaneous frequency $f(t)$ for the *PS* and *PSSS* wavelets shown in (b).

FFT-interpolated wavelets and their associated amplitude envelopes for the impulse response and *PS*–filtered synthetic wavelets selected in Fig. 3.4a. A 5% Hanning taper was applied to both ends of the wavelets to reduce FFT interpolation artifacts at the edges of the windows. The sections of $a(t)$ displayed indicate the integration limits for these wavelets, selected as $0.5 * [a(t)]_{\text{MAX}}$. Using the higher amplitude portion of the signal reduces the impact of noise on the results. Selecting the integration limits in this way also makes the Q estimates less sensitive to wavelet windowing. A slightly larger window than that containing the arrivals is used for intermediate calculations to reduce edge effects, although it is important not to include higher amplitudes that may affect the integration limits. The corresponding plots of instantaneous frequency $f(t)$ (Figure 3.4c) show a general decrease between *PS* and *PSSS*, most clearly observed for the impulse response (lower pair). The instantaneous pulse width $\tau(t)$, not shown, is merely the reciprocal of $f(t)$.

To generate the Q–gram, we center the reference wavelet, (*PS* in Fig. 3.4b) in a 128 point time window (1.6 s), with zeros padded on both ends. First we compute the signal attribute $\overline{\xi}_1$ for the unpropagated reference wavelet and the arrival time T_1, using equations (6) and (7), respectively. The propagation time ΔT for the Q–propagator is obtained from the arrival time difference between the windowed wavelets for the synthetic traces in Fig. 3.4a using equation (7). The propagated wavelet is then computed in the frequency domain using equation (11) with a 256 point FFT box, giving a propagated pulse trace length of 6.4 s. We use $f_0 = 9$ Hz, corresponding to the dominant frequency of *PS* (Fig. 3.3). After transformation to the time domain, a 128 point section of this trace, approximately centered about the known propagation time, is selected for FFT interpolation and computation of $\overline{\xi}_2'$, T_2' and Ψ'. Using the windowed section of the propagation trace reduces computation time and memory requirements, while using the longer time series to compute the propagated pulse

gives necessary spectral resolution. We increment Q^{-1} and repeat the propagation procedure, using a sufficiently wide Q^{-1} band to include any reasonable Q estimate for the data. Using $f(t)$ and $\tau(t)$ for ξ in equation (6) gives Q–grams designated $\overline{f}$–type and $\overline{\tau}$–type, respectively.

Figures 3.5a and 3.5b show $\overline{f}$–type and $\overline{\tau}$–type Q-grams, respectively, for the synthetic traces in Fig. 3.4a. The vertical axis on the right is the Ψ–axis for the *PS*–filtered synthetics. For the impulse response synthetics, using equations (7)–(8), with $n = 0$ for $\overline{f}$ and $n = 1$ for $\overline{\tau}$, we obtain $\Psi = 4.42$ s^{-2} and $\Psi = 0.0256$ for the $\overline{f}$–type and $\overline{\tau}$–type Q-grams, respectively, as indicated by the thin horizontal lines. These give Q^{-1} values of 1.01×10^{-2} and 1.00032×10^{-2}, respectively, as indicated by thin vertical lines. These correspond to estimates for sediment Q_β of 98.9 and 100.0, respectively, both of which are very close to the true $Q_\beta = 100$. For the *PS*–filtered synthetics, equation (8) gives $\Psi = 0.288$ s^{-2} and $\Psi = 0.000686$ for the $\overline{f}$–type and $\overline{\tau}$–type Q-grams, respectively, giving corresponding Q_β estimates of 103.0 and 98.4.

For both the impulse response and the *PS*–filtered synthetics, the error in the Q_β estimate was less than 10% for $n = 0, 1$, or 2 with both $\overline{f}$–type and $\overline{\tau}$–type Q-grams. The smallest error with $\overline{f}$ was obtained using $n = 0$ for the exponent in equations (6) and (7), while using $n = 1$ gave the best results with $\tau(t)$ for both impulse response and *PS*–filtered noise free synthetics. Figures 3.5a and 3.5b show much greater propagation loss for the impulse response, giving a Q_β estimate with a slightly smaller error than that from the *PS*–filtered synthetics. This is to be expected because *PS*–filtering removes most of the high frequency energy from the impulse response, reducing the difference $\overline{\xi}_2 - \overline{\xi}_1$. Also, close examination of the impulse response in Fig. 3.4a indicates that other arrivals are present in the larger windows needed for the *PS*–filtered synthetics. Interference from other arrivals reduces the reliability of any method of Q estimation.

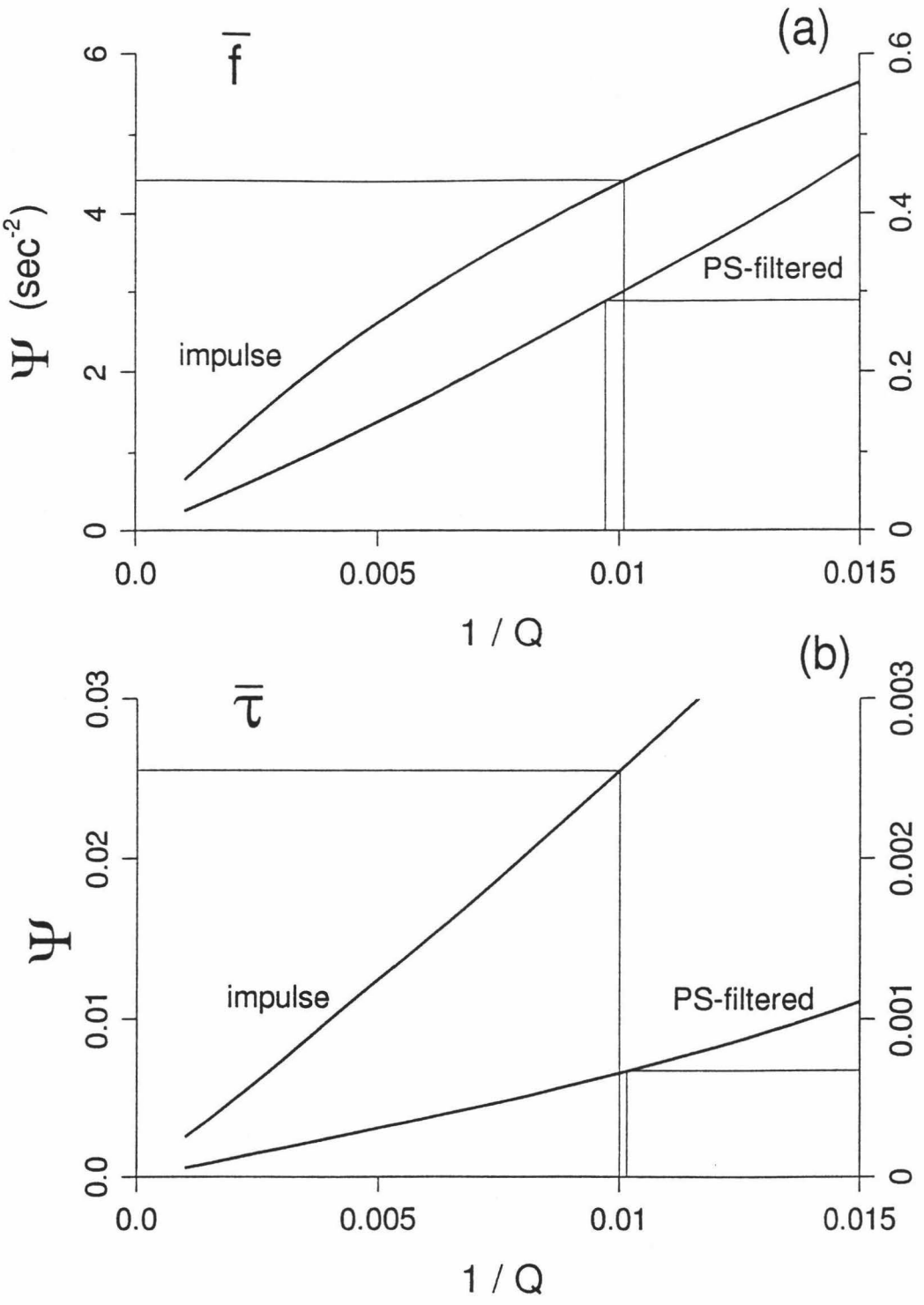

Figure 3.5: Q-grams for the *PS* wavelets of Fig. 3.4b. Left vertical axes are for the impulse synthetics and right vertical axes are for the *PS*–filtered synthetics. The value of true Q_β^{-1} used to make the synthetics was 0.01. (a) $\overline{f}$–type Q-grams giving Q_β estimates within 3% of the model Q_β. (b) $\overline{\tau}$–type Q-grams giving Q_β estimates within 2% of the model Q_β.

3.3.2 Error analysis

The difference between $\overline{\xi}_2$ for the data and $\overline{\xi}'_2$ for the propagated pulse with the true Q is the chief source of error in the Q estimate. Noise of any kind will affect the $\overline{\xi}$ of the lower amplitude later arrival much more than the $\overline{\xi}$ of the higher amplitude first arrival. Interference in the reference wavelet or in the later arrival will give an incorrect propagation time ΔT. Below we investigate the potential errors in the Q–gram method by including noise, traveltime error, and signal clipping in Q–gram computations for the synthetic traces in Fig. 3.4a.

3.3.2.1 *Noise and interference*

Noise in the OBS data includes background noise and signal generated noise from earlier shots. To determine the accuracy of the Q–gram method in the presence of noise, we added different levels of noise energy to the synthetic traces in Fig. 3.4a. We selected a portion of the OBS data trace prior to the water-wave (i.e. prior to W, Figure 3.2) as the noise estimate. We extended the noise estimate to the same length as the synthetic trace by transforming to the frequency domain, interpolating between spectral amplitude estimates so that the number of frequencies matched the number used to compute the synthetic trace, and then randomizing the phase. After transforming back to the time domain, the result was then added to the synthetic trace prior to wavelet windowing. Such noise affects the lower amplitude *PSSS* wavelet much more than the higher amplitude *PS*, and it reduces the accuracy of Q_β estimates more than white noise does.

To quantify the noise level in our noisy traces, we use 2 s of the trace preceding the W arrival to compute the rms noise amplitude $N_{\rm rms}$. The percent noise N is then defined as $N = 100 * N_{\rm rms}/|A_{max}|$, with $|A_{max}|$ the maximum amplitude in the signal

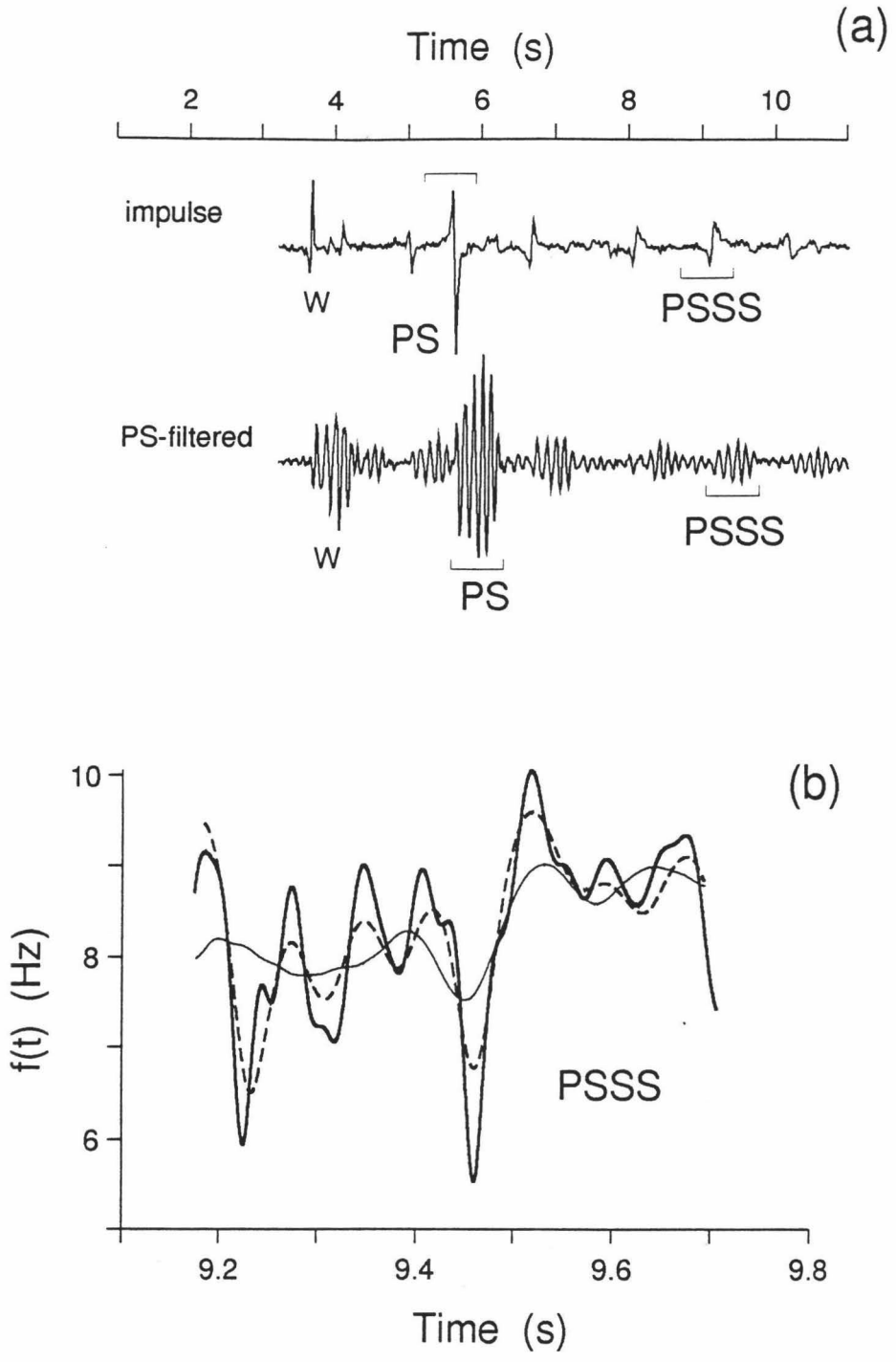

Figure 3.6: (a) Impulse response and *PS*–filtered synthetic traces shown in Fig. 3.4 with 7.5% added noise relative to *PSSS*. (b) Instantaneous frequency $f(t)$ for the *PS*–filtered *PSSS*: noise free (thin line); with added noise (thick line); with added noise and with subsequent 5–20 Hz zero–phase bandpass filtering (dashed).

of interest, either *PS* or *PSSS*. The traces with added noise (Fig. 3.6a) have about $N_{\mathrm{PS}} = 1.5\%$ and $N_{\mathrm{PSSS}} = 7.5\%$ noise energy relative to *PS* and *PSSS*, respectively. This compares with $N_{\mathrm{PS}} = 2.3\%$ and $N_{\mathrm{PSSS}} = 4.7\%$ noise energy for the OBS data trace in Fig. 3.2. Only small differences in *PSSS* are apparent when the synthetics in Figures 3.4a and 3.6a are compared. However, the relatively large amount of noise added to *PSSS* distorts the instantaneous phase, changing $f(t)$ from the thin solid line to the thick solid line in Fig. 3.6b.

Bandpass filtering the noisy seismograms prior to windowing the arrivals for Q estimation can improve the estimate of $f(t)$. The $f(t)$ shown dashed in Fig. 3.6b was obtained by *PS*–filtering the seismogram in Fig. 3.6a with a zero–phase 5–20 Hz bandpass filter, corresponding to that portion of the amplitude spectrum for *PS* and *PSSS* above the noise (Fig. 3.3). The difference between $f(t)$ with bandpass filtering and $f(t)$ for the noise free case (thin line) is less than without bandpass filtering (thick line). Subsequent tests showed that bandpass filtering the noisy *PS*–filtered synthetics reduced the scatter in the Q_β estimates. However, as expected, bandpass filtering had an adverse effect on the $f(t)$ of the noisy impulse response, increasing the scatter in both Ψ and Q.

Additional tests showed that using $n = 2$ for the exponent in equations (6) and (7), i.e. modulating $\xi(t)$ by the instantaneous energy in the signal, gave the most consistent results for both the impulse response and *PS*–filtered synthetics with added noise. In this way, the higher amplitude portion of the signal, where the signal–to–noise ratio is greatest, is given more weight in the Q estimate. We use $n = 2$ for all Q–grams of signals with noise.

Figure 3.7 shows $\overline{f}$– and $\overline{\tau}$–type Q–grams made from noisy impulse response synthetics for ten different realizations of the added noise. All Q_β estimates for both $\overline{f}$– and $\overline{\tau}$–type Q–grams in Fig. 3.7 were within 25% of the true Q_β. Figure 3.8

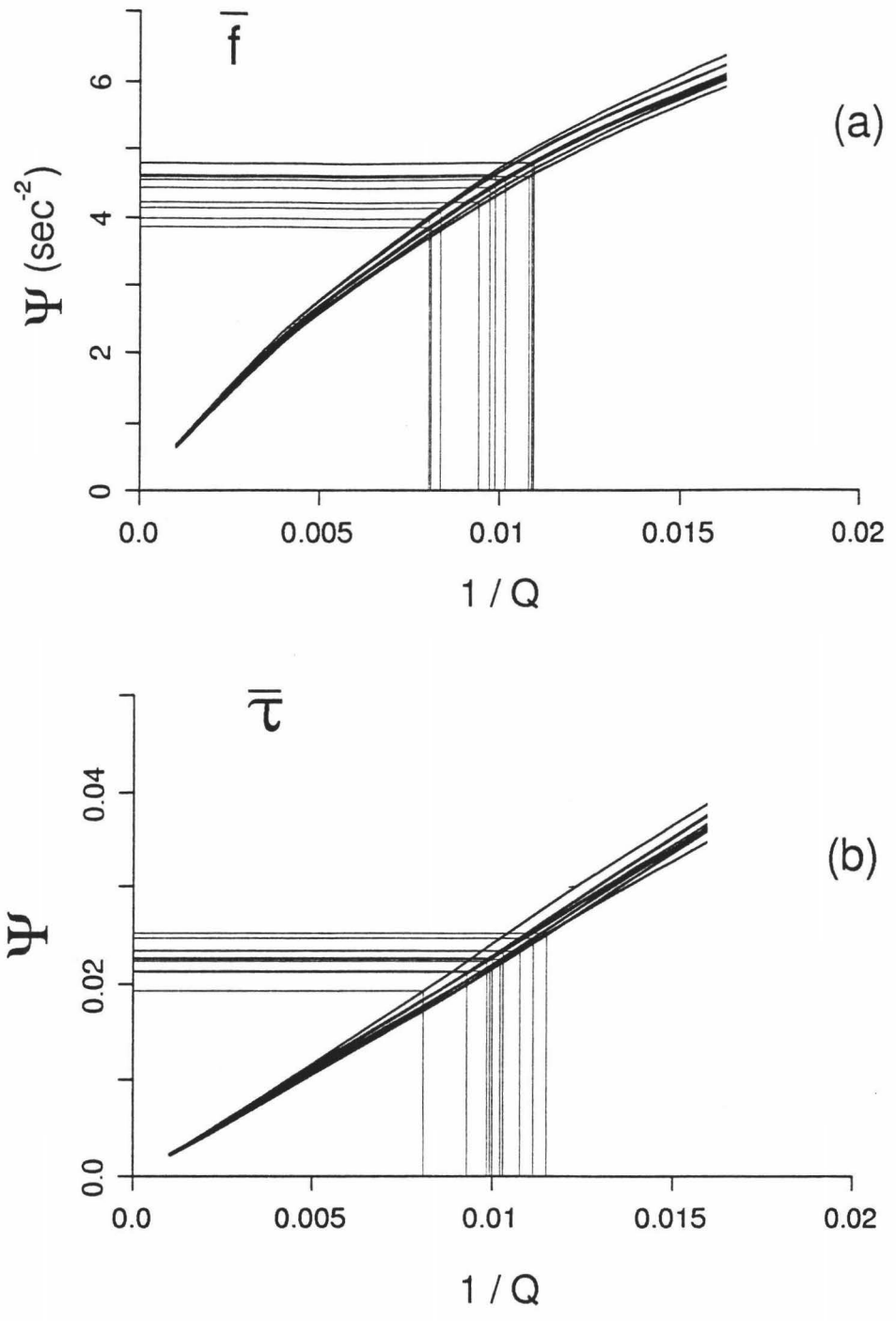

Figure 3.7: Q–grams for the impulse response synthetics with $N_{\text{PSSS}} \approx 7.5\%$ for ten noise realizations. (a) $\overline{f}$–type Q–grams. (b) $\overline{\tau}$–type Q–grams. The true $Q_\beta^{-1} = 0.01$.

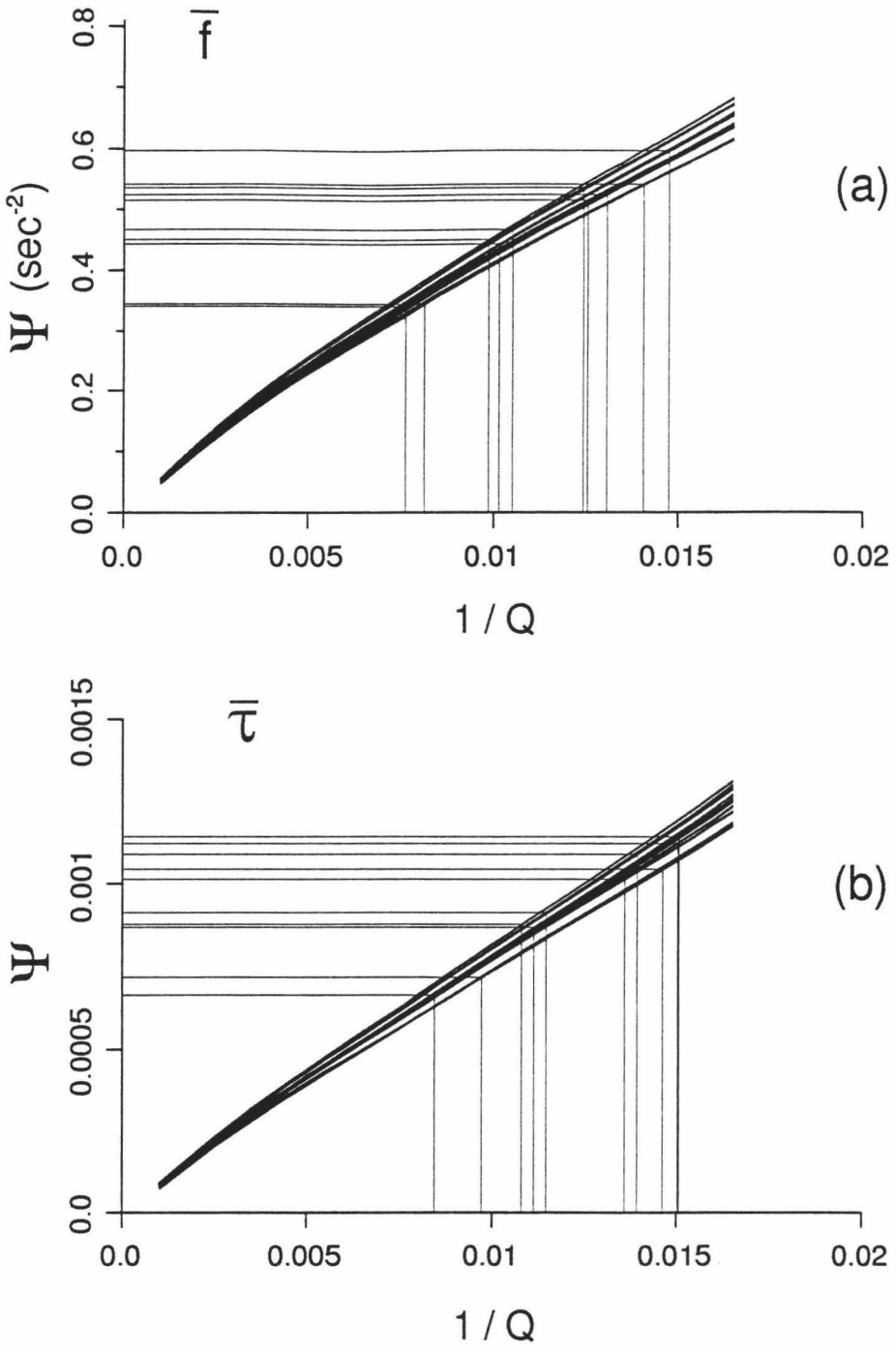

Figure 3.8: Q–grams for the *PS*–filtered synthetics with $N_{\text{PSSS}} \approx 7.5\%$ for ten noise realizations. (a) $\overline{f}$–type Q–grams. (b) $\overline{\tau}$–type Q–grams. The true $Q_\beta^{-1} = 0.01$.

is similar to Fig. 3.7 except that noisy *PS*–filtered, bandpass filtered seismograms were used. For the *PS*–filtered synthetic $\overline{f}$–type Q–grams in Figure 3.8a, 7 out of 10 noise realizations gave corresponding Q_β estimates having less than 25% error. The Q_β estimates with $\overline{\tau}$–type Q–grams (Fig. 3.8b) gave similar results, with 6 out of 10 realizations having less than 25% error but with a slightly greater tendency to underestimate the true Q than with $f(t)$. All Q_β estimates were within 35% of the true Q for both $\overline{f}$– and $\overline{\tau}$–type Q–grams for the ten noise realizations for the *PS*–filtered synthetics.

It is important to note that in the noise tests described above, N_{PSSS} was 60% larger than the N_{PSSS} of the actual OBS data. This relatively high noise level was used as a worst case test to study the manner in which the Q–gram method deteriorated with noise. When these same noise tests were repeated using a lower level of added noise, so that N_{PSSS} of the synthetics was the same as N_{PSSS} of the actual OBS data, all ten Q_β estimates were within 15% of the input Q_β. These tests demonstrate that the Q–gram method gives reliable Q estimates in the presence of moderate amounts of noise. They also suggest that in the actual OBS data neither the noise level relative to *PS* nor the noise level relative to *PSSS* are high enough to significantly affect the reliability of the sediment Q_β estimate.

3.3.2.2 *Traveltime, clipping and phase shift*

Equation (8) shows that any traveltime error will be more important as ΔT and Q^{-1} decrease, since the difference $\overline{\xi}_1 - \overline{\xi}'_2$ is then smaller. Using the average velocity $\bar{c}$ determined with equation (13), the two–way, vertical S–wave traveltime through the sediment column for the model in Table 3.1 is 3.536 s. The traveltime differences ΔT between *PS* and *PSSS* on the traces in Fig. 3.4a, measured using equation (7) with modulation exponent $n = 2$, are 3.498 s and 3.475 s for the impulse and *PS*–

filtered synthetics, respectively. Adding noise (Fig. 3.6a) changes the measured ΔT by less than 0.01 s for both the impulse and *PS*–filtered synthetics. To estimate the potential error in Q^{-1} due to traveltime measurement error, we computed Q–grams for the noisy synthetics using $\Delta T = \Delta T \pm 0.1 * \Delta T$ in equation (11) and obtained Q_β within 2% of the initial estimates from both $\tau(t)$ and $f(t)$. These results show that traveltime measurement error will not adversely affect the accuracy of Q_β estimates from our OBS data.

Limited instrument dynamic range causes soft–clipping of the highest amplitude arrivals on almost every trace of our OBS data, affecting primarily *PS*. To test the effect of soft–clipping on the Q–gram method, we soft–clipped the *PS*–filtered noisy synthetic so that the apparent noise level of *PS* increased from $N_{\mathrm{PS}} = 1.5\%$ to $N_{\mathrm{PS}} = 2.3\%$, matching that of *PS* in the OBS data. In our soft–clipping, the seismic trace is first scaled by $\sinh(1.0)/(\textit{clipping level})$. We then take the $\sinh^{-1}$ of the scaled trace to obtain the soft–clipped trace. Figure 3.9a shows the soft-clipped (solid) and unclipped (dashed) *PS* wavelets and their associated $a(t)$ for the *PS*–filtered synthetics. This amount of clipping gives a relative amplitude ratio for *PS*/*PSSS* of about 3:1 compared with a 2:1 ratio for the actual OBS data. Clipping the synthetics to a 2:1 ratio removes all the amplitude variation in the synthetic *PS*. The obvious amplitude variation seen in the OBS data *PS* suggests that the *PS*/*PSSS* amplitude ratio difference between synthetic and data is due to a reflection coefficient, not to clipping.

Clipping causes $a(t)$ (Fig. 3.9a, solid) to vary appreciably from the unclipped $a(t)$ (dashed) and gives a characteristic scalloped appearance. In Fig. 9b, a considerable difference is apparent between the $f(t)$ of the clipped (thick solid) and unclipped (dashed) wavelets. However, Fig. 3.9c shows that the corresponding Q–grams for these wavelets, computed with modulation exponent $n = 2$, have only small differ-

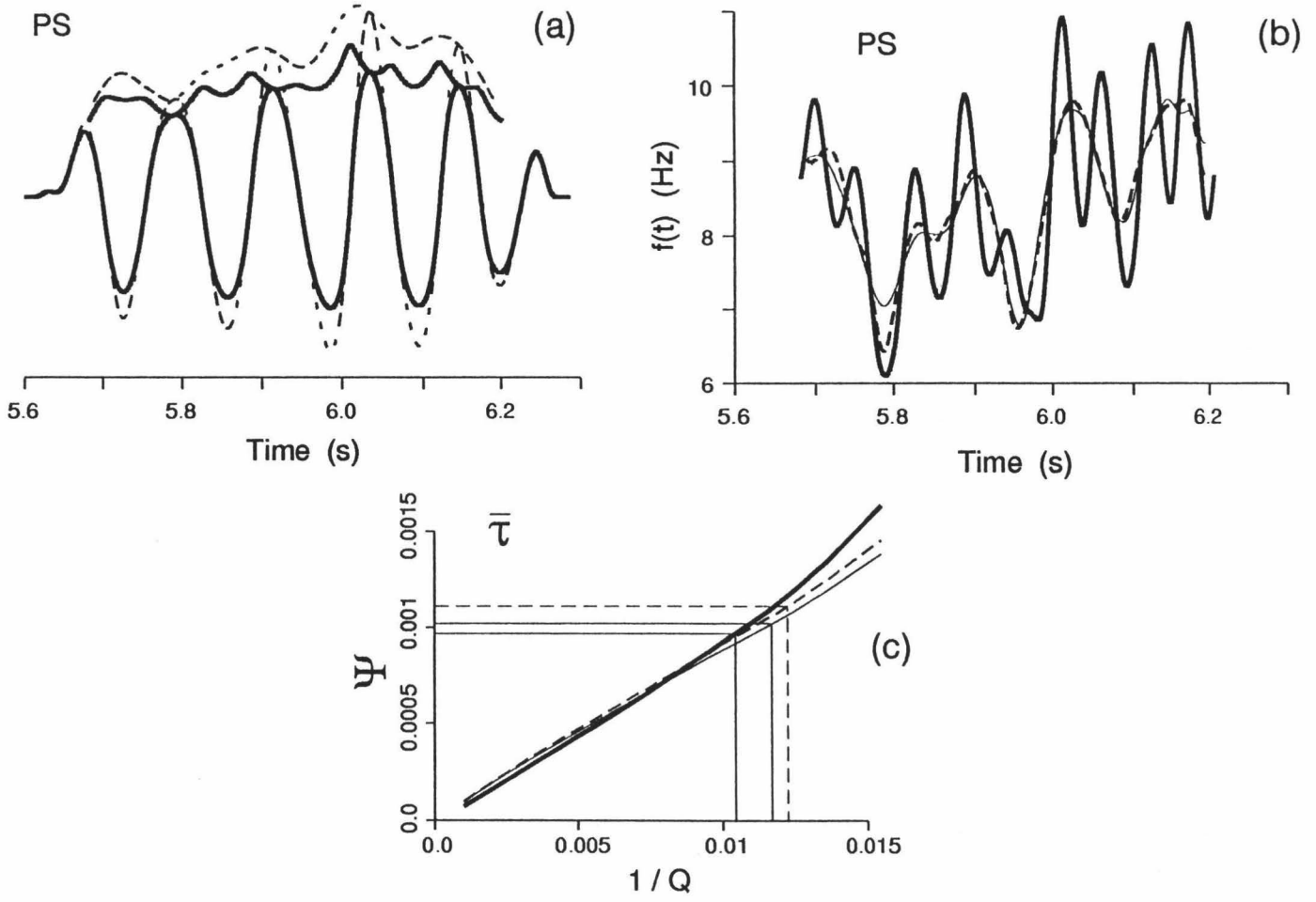

Figure 3.9: (a) The soft-clipped (thick solid) and unclipped (dashed) synthetic *PS* wavelets with added noise and their associated $a(t)$. (b) $f(t)$ for the wavelets in (a). The thin solid line shows $f(t)$ for the unclipped *PS* wavelet without noise. (c) Q-grams computed using the $f(t)$ from (b). Differences between the clipped (thick solid) and the unclipped (dashed) Q-grams are small even though their corresponding $f(t)$ differ significantly. The thin, solid Q-gram is the Q-gram for the noise free case. It differs from the $\overline{\tau}$-type Q-gram in Fig. 3.5b because here $n = 2$ instead of $n = 1$.

ences. Adding noise increases both the slope of the Q–gram and Ψ from the unclipped noise free case (light line). The most significant effect of clipping the noisy synthetic is the reduction in Ψ, causing the Q_β estimate to increase about 15% from 82 to 96. *Bromirski et al.* (1992a) found that moderate soft–clipping also tends to increase spectral ratio Q estimates. As the amplitude variation of our clipped synthetic *PS* is much less than that of our data *PS*, we conclude that the tests shown here represent a worst case and that Q_β estimates obtained below for the OBS data are unaffected by clipping.

We also tested the effect of phase shifts by taking the Hilbert transform of the second arrival, giving a $\pi/2$ phase shift. Tests on both the impulse response and *PS*–filtered synthetics gave less than a 2% change in Q_β for both $\overline{f}$– and $\overline{\tau}$–type Q–grams, showing that the Q–gram method using equation (6) is insensitive to phase shift distortion.

3.3.3 Comparison with spectral ratios

To compare the accuracy of Q estimates from $\overline{\xi}$– and $\overline{\tau}$–type Q–grams with those from the spectral ratio method, we computed spectral ratios for both the impulse response and *PS*–filtered synthetics for the same ten noise realizations ($N_{\mathrm{PSSS}} \approx 7.5\%$) used in the Q–gram tests. More careful arrival selection using a smaller window than with the Q–gram method was necessary to exclude other arrivals in the spectral ratios. We follow the spectral ratio procedure given by *Bromirski et al.* (1992a), but we applied no taper and did not subtract the noise estimate. The spectral ratios for the impulse response and *PS*–filtered synthetics are shown in Figures 3.10a and 3.10b, respectively. The dashed lines in these figures are spectral ratios for the noise free synthetics.

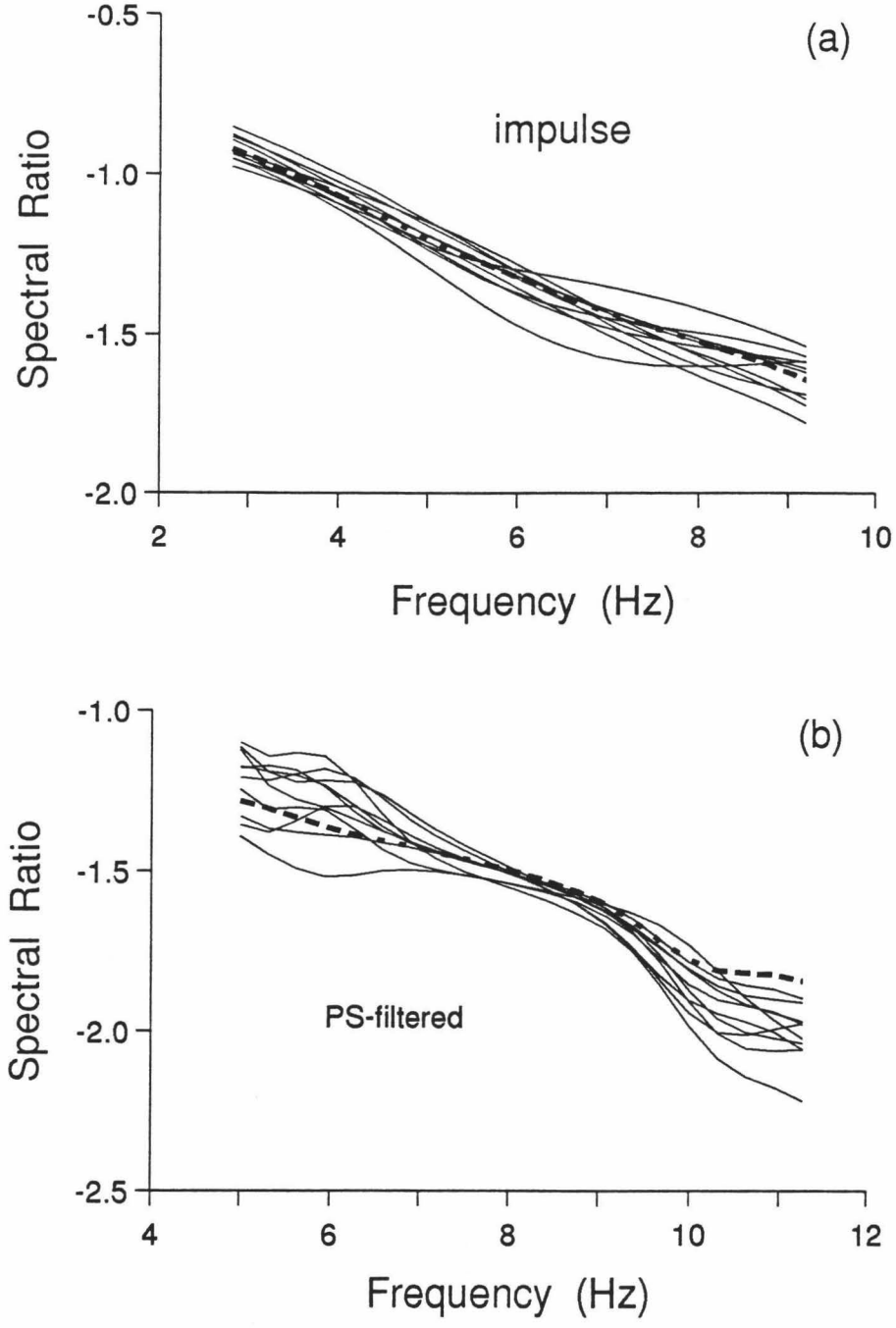

Figure 3.10: (a) Spectral ratios of *PS* and *PSSS* for the ten noisy impulse response synthetics in Figures 3.7. (b) As in (a) except that the noisy *PS*–filtered synthetics were used. The thick dashed lines in these figures are spectral ratios for the noise free synthetics.

Least squares estimates of the slopes of these spectral ratios were obtained in the 2–10 Hz band for the impulse response and in the 5–12 Hz band for the *PS*–filtered synthetics. The spectral ratios become extremely irregular outside these narrow bands. The spectral ratios in Fig. 3.10 give Q_β estimates with an error distribution very similar to that obtained from the $\overline{\tau}$–type Q–grams in Figures 3.7b and 3.8b, respectively. Interestingly, the spectral ratio method gave $Q_\beta = 114$ for the noise free *PS*–filtered synthetics, not as accurate as the Q–gram Q_β estimates of 103 and 98 using the $f(t)$ and $\tau(t)$ signal attributes, respectively.

3.3.4 Application to OBS data

We apply the Q–gram method to the OBS data wavelets shown in Fig. 3.2. We use $a(t) > 0.5 * [a(t)]_{\text{MAX}}$ to select the integration limits in equations (6) and (7) as in the synthetic tests. The FFT-interpolated wavelets are shown in Fig. 3.11a, and their corresponding $f(t)$ are shown in Fig. 3.11b. The *PS* and *PSSS* $f(t)$ are far less similar for the data than they are for the *PS*–filtered synthetics (Fig. 3.4c), but their similarity is still recognizable and there is a decrease in $\overline{f}$ from *PS* to *PSSS*.

In Fig. 11b, the much more irregular character of $f(t)$ at the front of *PSSS* compared with *PS* suggests interference from other arrivals. To reduce the irregularity in $f(t)$ and the impact of noise and interference on the Q_β estimate, we bandpass filter the data trace, as in the tests on the noisy *PS*–filtered synthetics, using a 5–20 Hz zero–phase filter. Comparison of Fig. 3.11c with Fig. 3.6b shows that bandpass filtering changes the $f(t)$ of the data *PSSS* much less than it changes the $f(t)$ of the synthetic *PSSS*. This is because the noise level in the data is much lower than the noise level in the synthetics.

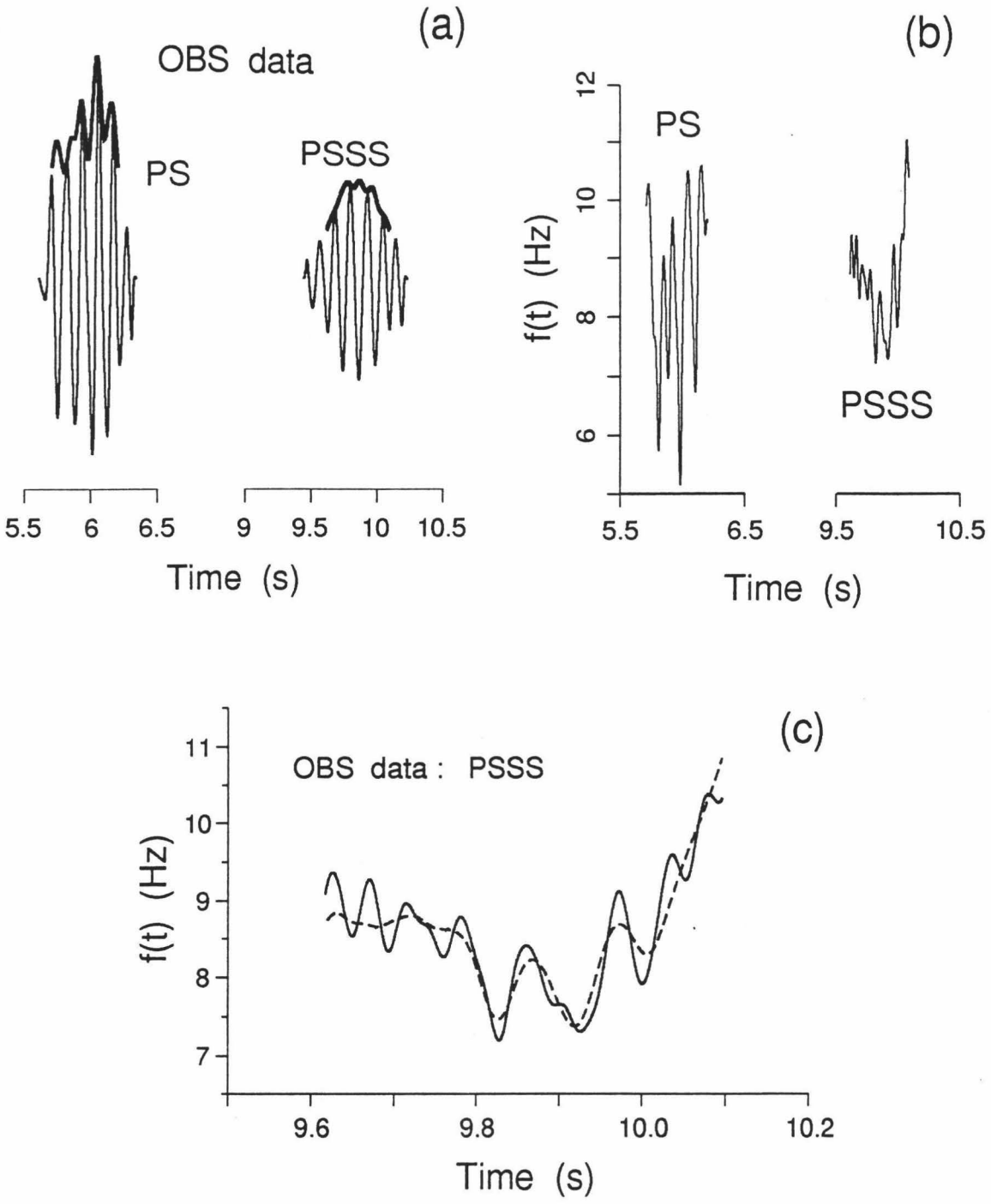

Figure 3.11: (a) OBS data wavelets after 5–20 Hz bandpass filtering and FFT interpolation. Very little difference can be seen between these wavelets and the unfiltered wavelets in Fig. 2. The instantaneous amplitude $a(t)$ (thick lines) indicate the portions of the wavelets selected for Q_β estimation. (b) The instantaneous frequency $f(t)$ for the wavelets in (a). (c) Instantaneous frequency for the bandpass filtered *PSSS* (dashed) and for the unfiltered *PSSS* (solid).

Figure 3.12a shows $\overline{f}$-type Q–grams for the OBS data, computed using $n = 2$ in equations (7)–(8). The dashed Q–gram was made from the unfiltered data trace, and the thick solid Q–gram was made from the same trace after zero–phase bandpass filtering similar to the synthetic tests above. The Q–gram for the unfiltered trace gave $Q_\beta = 102$ while the Q–gram for the bandpass filtered trace gave $Q_\beta = 90$. Figure 3.12b shows corresponding $\overline{\tau}$-type Q–grams where the raw trace gave $Q_\beta = 106$ and the filtered trace gave $Q_\beta = 93$. Bandpass filtering causes the difference $\overline{\xi}'_2 - \overline{\xi}_1$ to be smaller, giving a Q–gram with a reduced slope. Although filtering the OBS data causes only a small change in Ψ, the Q_β estimate is reduced.

Since $f(t)$ should decrease from *PS* to *PSSS* for corresponding times, the jump in $f(t)$ at the end of the data *PSSS* is attributable to interference. To test the effect of excluding the trailing end of the integration window, we recomputed all the Q–grams in Figures 3.8b and 3.8a but with the trailing 5% of the windows excluded. In general, the Q_β estimate was within 5% of the full window estimate for both $\overline{\tau}$ and $\overline{f}$. This means that the accuracy of the Q_β estimate from the OBS data will not be changed appreciably by excluding the margins of the integration windows, unless the margins contain interfering arrivals. In fact, the Q–grams computed from the data using the slightly shorter windows (Figures 3.12a and 3.12b, light lines) show a relatively large change, giving Q_β estimates of 72 and 78 with $\overline{f}$ and $\overline{\tau}$, respectively, showing that significant interference has been excluded.

In an attempt to corroborate the Q_β estimate from the trace at 0.41 km, we also analyzed the other traces at less than 1 km offset, shown in Fig. 3.13. We attribute the considerable trace to trace variation of *PSSS* to interference resulting from complexity of the local shear-wave velocity structure. The reverberative character of *PS* and *PSSS* probably results from a combination of airgun bubble-pulse oscillations, effects of coupling of the instrument package with the soft sediments and multi-pathing

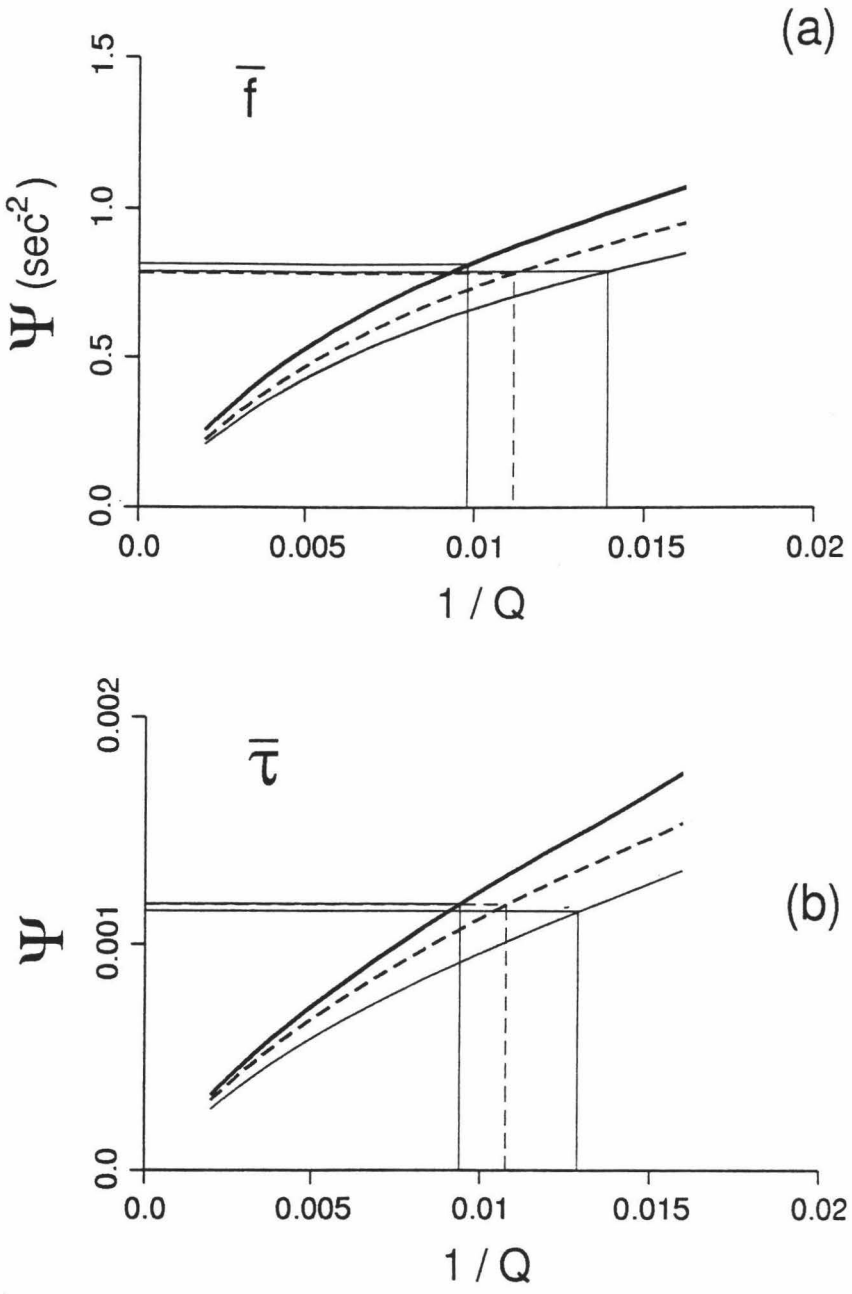

Figure 3.12: Q–grams for the OBS data trace at 0.41 km. Solid curves are for the unfiltered trace and dashed curves are for the bandpass filtered trace. Thin solid lines are the Q–gram computed with the trailing 5% of the integration window excluded. (a) $\overline{f}$–type Q–gram: Q_β estimates are 102, 90 and 72 for the unfiltered, filtered and short-window Q–grams, respectively. (b) $\overline{\tau}$–type Q–gram: the Q_β estimates are 106, 93 and 78, respectively.

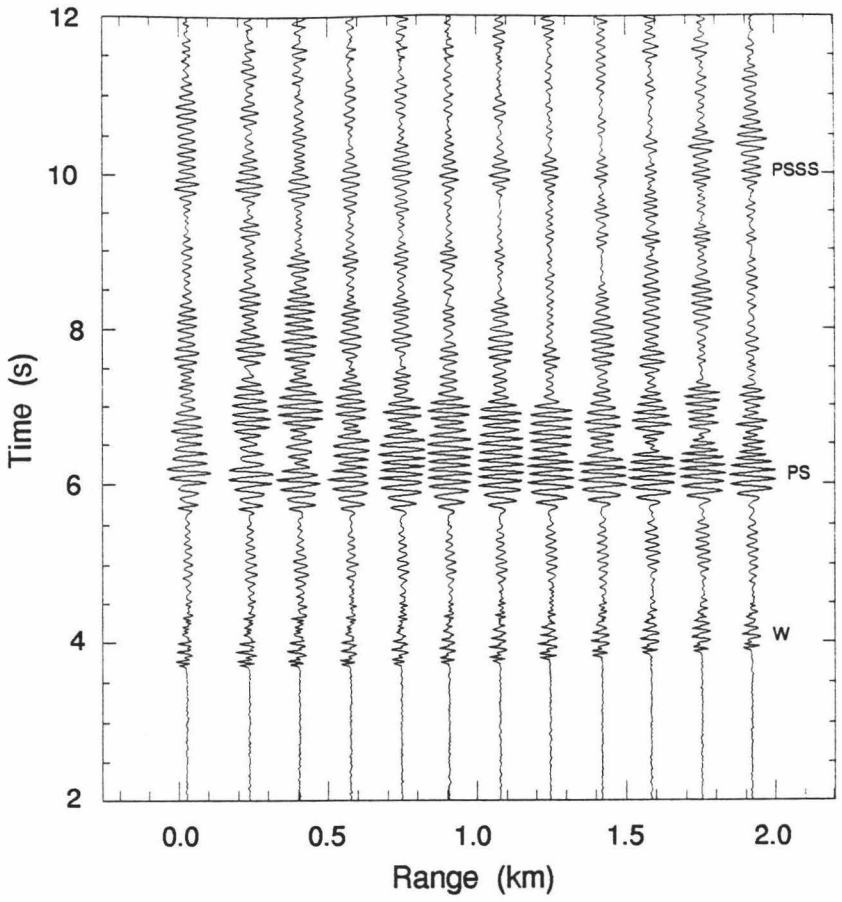

Figure 3.13: Trace-normalized horizontal OBS data at distances to 2 km. The water-wave, W, and the *PS* and *PSSS* converted shear reflections are identified (same data as in Fig. 3.1).

within the chert layers at the base of the sediments. Significant clipping of *PS* is apparent for offsets greater than 0.58 km. In addition, *PS* is subject to interference with crustal refraction phases between 3 and 12 km (Fig. 3.1). At offsets greater than 12 km, the water-wave surface multiple interferes with *PSSS*. Consequently, only for the near offset traces is a Q_β estimate possible.

Differences between $f(t)$ for *PS* and *PSSS* in OBS data traces other than at 0.41 km also suggest significant interference. For the two nearest offset OBS data traces, $\overline{f}$ increased from *PS* to *PSSS*. To test the effect of offset on the Q–gram Q_β

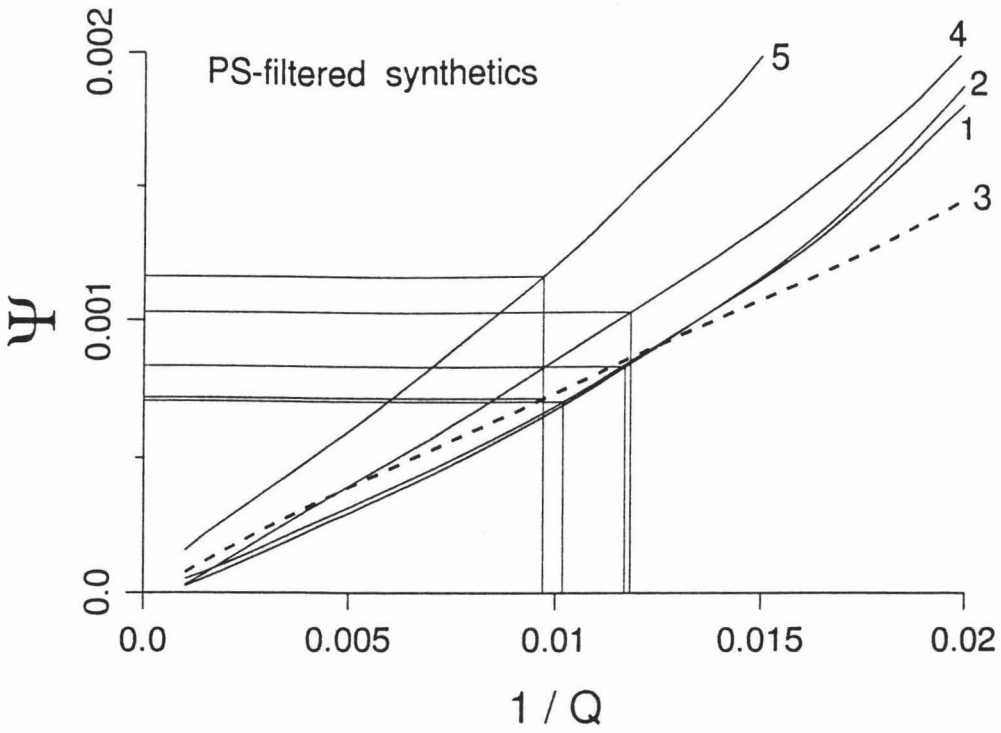

Figure 3.14: $\overline{\tau}$–type Q–grams for near offset, noisy, *PS*–filtered reflectivity synthetics with bandpass filtering. The traces were computed using the model in Table 1 at offsets of 0.03, 0.24, 0.41, 0.58 and 0.75 km, corresponding to the Q–grams numbered 1–5, respectively. Note the variation in Ψ and the slope of the Q–grams with offset. All the resulting Q_β estimates are within 20% of the model Q_β. Q–gram number 3 (dashed) is discussed above in detail, as the 0.41 km offset is the one least affected by interference and clipping. The true $Q_\beta^{-1} = 0.01$.

estimates, we applied the Q–gram method to *PS*–filtered reflectivity synthetics computed using the model in Table 3.1 for the same offsets as the OBS data. Figure 3.14 shows the $\overline{\tau}$–type Q-grams for synthetic traces at 0.03, 0.24, 0.41, 0.58 and 0.75 km, numbered 1-5, respectively. Only small differences were observed among corresponding arrivals on the five traces. Although a general increase in Ψ and a steepening of the slope of the Q–grams with offset are observed, the Q_β estimates are within 20% of the sediment shear $Q_I = 100$ for the model. The anomalous behavior of $\overline{f}$ for the two nearest data traces cannot be due to reduced P–to–S conversion because our

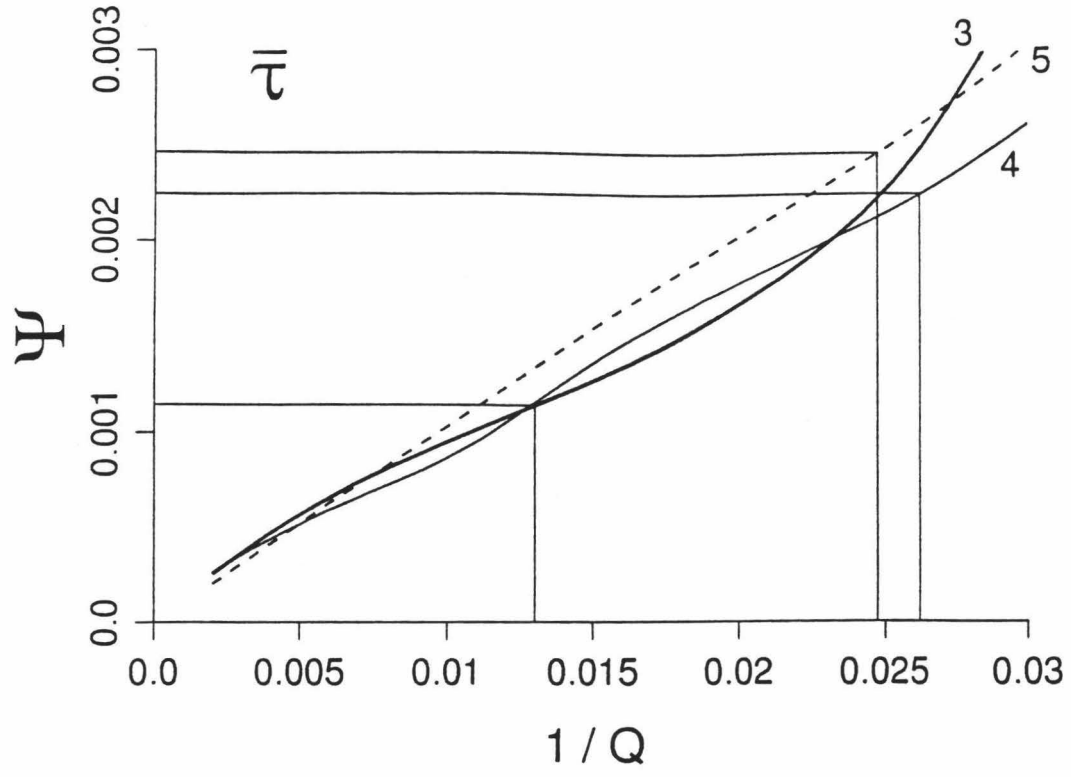

Figure 3.15: $\overline{\tau}$–type Q–grams for the bandpass filtered OBS data at 0.41, 0.58 and 0.75 km offset, corresponding to Q–grams numbered 3–5, respectively. These give sediment Q_β estimates of 72, 38 and 40, respectively.

methods are amplitude independent.

Inspection of $f(t)$ for *PS* and *PSSS* for the OBS data trace at 0.58 km indicated that more interference is present there than in the trace at 0.41 km. The trace at 0.58 km gives a significantly lower estimate, $Q_\beta = 38$, using the $\overline{\tau}$–type Q–gram (Fig. 3.15). Examination of $a(t)$ for *PS* in the trace at 0.75 km offset indicated significant clipping of the higher amplitude pulses in the arrival, inferred from the scalloped character of $a(t)$ similar to that exhibited by the clipped synthetic $a(t)$ in Fig. 3.9a. The $\overline{\tau}$–type Q–gram together with Ψ for this trace (Fig. 3.15) gives $Q_\beta \approx 40$. Note that there is a general increase both in Ψ and in the steepness of the Q–gram with offset, similar to that observed for the synthetics in Fig. 3.14.

In view of the poor data quality at offsets away from 0.41 km, it is desirable to have an error estimation method for a single trace. Accordingly, we devised a procedure called "noise doubling". In noise doubling we generate many realizations of the noise process, each with power equal to the noise power in the data. For each noise realization, we add that realization to the (already noisy) data trace, construct a Q–gram, and estimate Q^{-1}. The complete set of Q^{-1} is then binned to make a histogram. The histogram (not shown) is just a plot of the density of thin vertical lines in a figure similar to Fig. 3.8a. The peak of the histogram is not an unbiased estimator of the true Q, because of the noise already present in the raw data trace. However, the halfwidth of the histogram is an unbiased estimator of the error in our Q^{-1} estimate. Use of this procedure on the trace at 0.41 km gives a Q^{-1} estimate error of 15%. Excluding results from other offsets, our best estimate of Q_β is therefore 75 ± 15.

Bromirski et al. (1992a) obtained an average sediment Q_β estimate of 97 from the spectral ratio of *PS* and *PSSS* for the five nearest traces in Fig. 3.1, but they did not take into account interference effects identified here using $f(t)$. Consequently, their Q_β estimate may be in error. As noted above, applying the spectral ratio method to the OBS data trace at 0.41 km with the trailing ends of *PS* and *PSSS* excluded gives an estimate of $Q_\beta = 75$ for the band from 5–15 Hz, in agreement with our Q–gram results for the same trace.

3.4 DISCUSSION

Our use of $\overline{\tau}$ and $\overline{f}$ as signal attributes was arrived at only after a long series of unsuccessful attempts to extend earlier definitions of pulse width for use on our rather

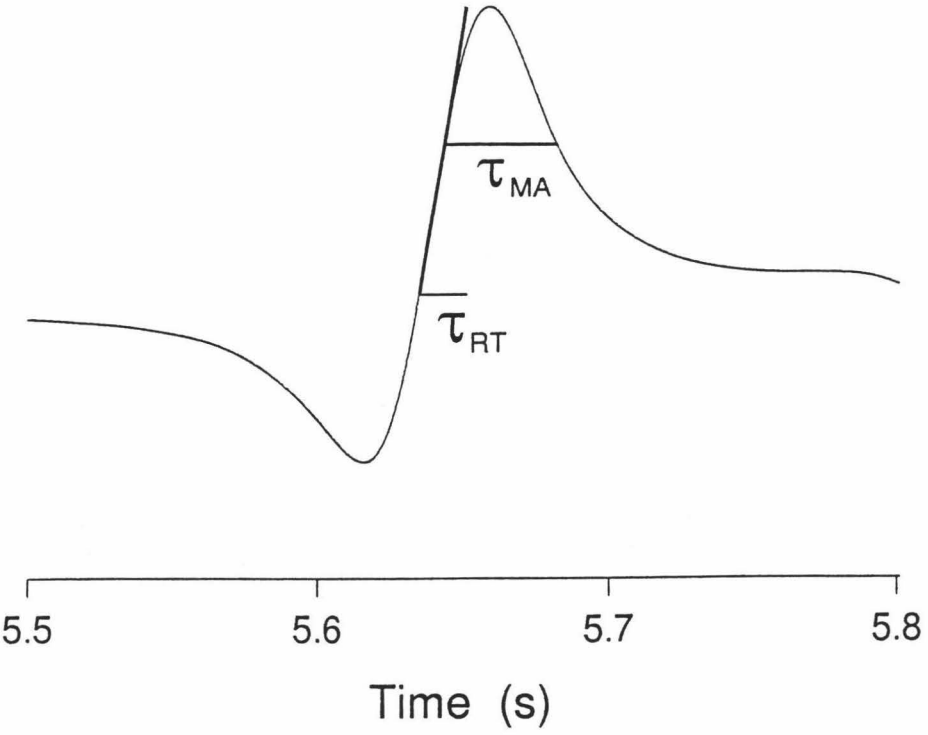

Figure 3.16: The impulse response *PS* showing the rise time τ_{RT} and mid–amplitude τ_{MA} pulse width measures (horizontal lines). The thick, nearly vertical line indicates the maximum slope and peak amplitude that determine τ_{RT}.

oscillatory signals. However, any consistent definitions of ξ and T can be used to construct a Q–gram. To demonstrate the flexibility of the Q–gram method, and to show why $\overline{\tau}$ and $\overline{f}$ make good signal attributes, we briefly consider two somewhat more natural choices for $\overline{\xi}$, the pulse width defined by rise time, τ_{RT}, and the mid–amplitude pulse width, τ_{MA}.

The rise time pulse width τ_{RT} is defined as the peak pulse amplitude divided by the maximum slope on the rising limb of the pulse (*Gladwin and Stacey*, 1974). For this example, we define arrival time T as the time of maximum slope. The rise time τ_{RT} for the impulse response *PS* is shown in Fig. 3.16, where the thick line indicates both the maximum slope and peak amplitude. In previous applications of the rise time method (e.g. *Gladwin and Stacey*, 1974; *Jannsen et al.*, 1985; *Tonn*, 1991),

a linear relationship between τ_{RT} and T is assumed. Q is then estimated from two arrivals as

$$Q = C(Q)\,\frac{(T_2 - T_1)}{(\tau_2 - \tau_1)} \tag{14}$$

where τ_1 and τ_2 are the pulse widths, T_1 and T_2 are the arrival times of maximum slope, and the proportionality constant $C(Q)$ depends on the source and the receiver. Note that equation (14) is the reciprocal of equation (8) except for $C(Q)$. The value of $C(Q)$ is generally assumed to be close to 0.50 for sufficiently impulsive sources recorded on broadband instruments. However, $C(Q)$ must be determined separately to obtain an accurate Q estimate (e.g. *Bromirski et al.*, 1992b). The Q–gram method using τ_{RT} for $\overline{\xi}$ has two clear advantages over the conventional rise time method: (1) the "constant" $C(Q)$ does not have to be either determined or assumed and (2) the assumption of a linear relationship between τ_{RT} and T is unnecessary.

Another natural choice for $\overline{\xi}$ is τ_{MA}, the mid–amplitude width of the peak pulse in the signal (also shown in Fig. 3.16), with traveltime T defined as the midpoint of the measured pulse width (*Bromirski et al.*, 1992b). Figure 3.17 shows the Q–grams for the impulse response synthetic in Fig. 3.4a using the τ_{RT} and τ_{MA} signal attributes for $\overline{\xi}$, with (dashed) and without (solid) noise. The Ψ–axis on the right is for the τ_{RT}–type Q–grams. Also included in Fig. 3.17 are the $\overline{\tau}$–type Q–grams from Figures 3.5b and 3.7b. Although the τ_{RT} measurements gave Q_β estimates within 15% of the model $Q_I = 100$, the $\overline{\tau}$–type Q–gram is clearly more accurate. The τ_{MA}–type Q–gram gives a Q_β estimate with less than 20% error for the noise free impulse response, but about a 100% error with noise added. The jump in the τ_{MA}–type Q–gram with noise at $Q^{-1} \approx 0.0085$ indicates a change in the pulse shape, and is also an indication that the Q estimate is unreliable.

For oscillatory arrivals such as *PS* and *PSSS* in the OBS data, it is unclear where to measure τ_{RT} or τ_{MA}, motivating the definitions of $\overline{\xi}$ and T given in equations

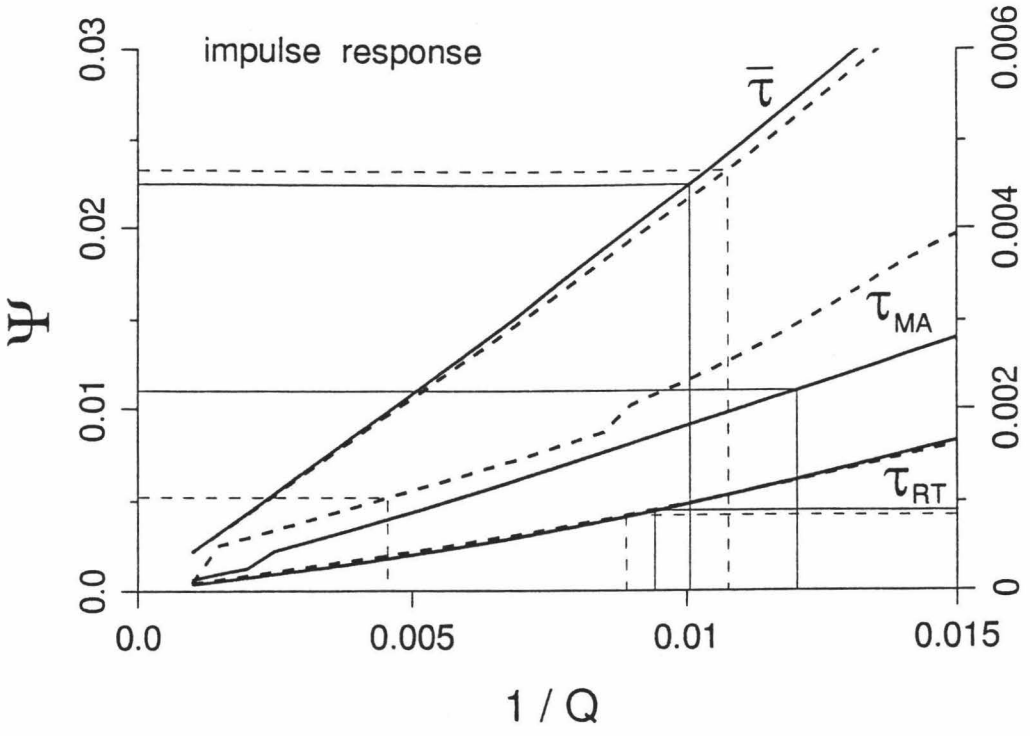

Figure 3.17: Q–grams for the impulse response using τ_{RT} and τ_{MA} with (dashed) and without (solid) added noise. The Ψ–axis on the right is for the τ_{RT}–type Q–grams. The $\overline{\tau}$–type Q–grams are included for comparison. The true $Q_\beta^{-1} = 0.01$.

(6) and (7). Any difference between seismic group velocity and phase velocity would bias Q estimates from measurement of single half-cycles. Consequently, we use for $\overline{\xi}$ the quantity $\overline{\tau}_{RT}$, an average of τ_{RT} over successive half-cycles. In Fig. 3.18, we show $\overline{\tau}_{RT}$–type Q–grams without noise (thick, solid), with added noise (dashed) and band-pass filtered with noise (dotted). The $\overline{\tau}$–type Q–gram from Fig. 3.8b (light, solid) is included for comparison. The number in parentheses gives the number of successive half-cycles for which τ_{RT} was averaged, starting with the first half-cycle whose amplitude is greater than 25% of the peak amplitude. The Q estimates obtained with $\overline{\tau}_{RT}$–type Q–grams were more than double the true Q. With the addition of the same

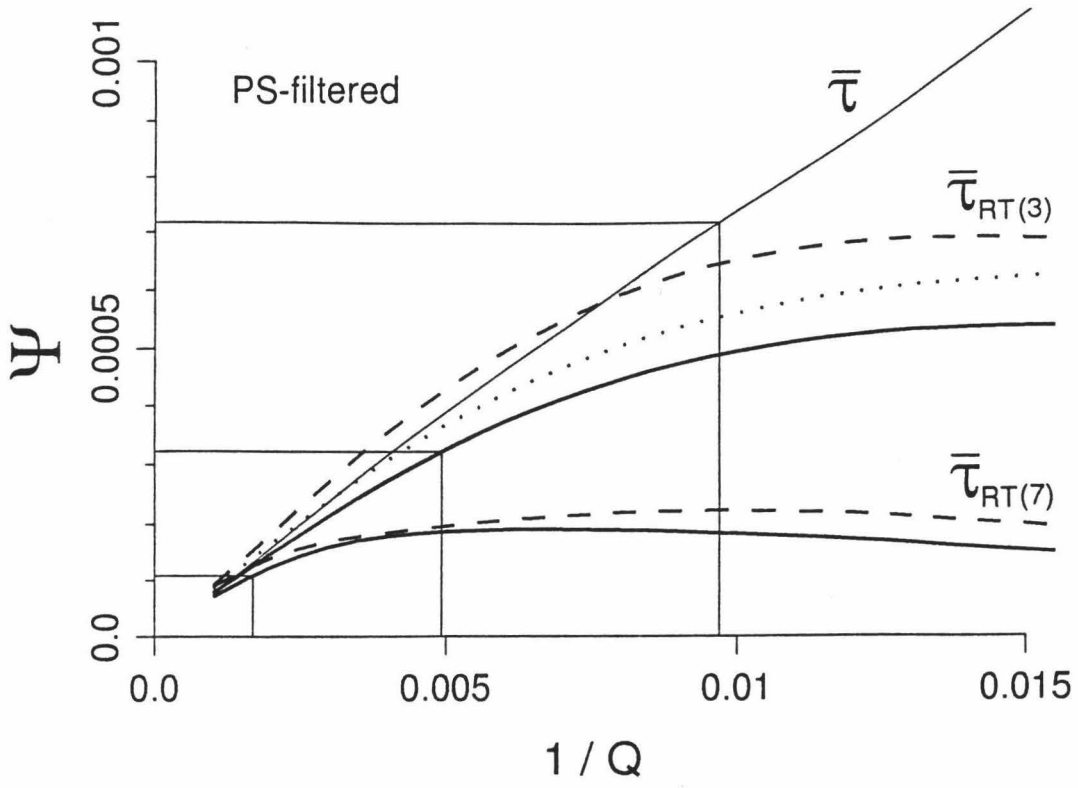

Figure 3.18: Q–grams computed for the *PS*–filtered synthetic using average rise time, $\overline{\tau}_{RT}$, for ξ. Shown are Q–grams without noise (thick, solid), with added noise (dashed) and bandpass filtered with noise (dotted). The $\overline{\tau}$–type Q–gram (light, solid) from Fig. 5b is included for comparison. The numbers in parentheses give the number of successive half cycles that were averaged to obtain $\overline{\tau}_{RT}$.

amount of noise as in Fig. 3.6a, the $\overline{\tau}_{RT}$ measure gives negative values for Ψ. These results demonstrate the inapplicability of the rise time method to oscillatory arrivals. They also show that a smooth Q–gram does not guarantee an accurate Q estimate. The usefulness of a particular signal attribute depends on the characteristics of the wavelets and should be determined by tests on the reference data wavelet.

3.5 CONCLUSIONS

We have shown that the Q–gram method gives reliable Q estimates for both impulsive and oscillatory arrivals in the presence of moderate amounts of noise. Both the averaged instantaneous frequency and the averaged instantaneous pulse width are good signal attributes to measure propagation loss. For noisy synthetic data, the $\overline{f}$–type Q–gram gave a slightly more accurate estimate of Q than did the $\overline{\tau}$–type Q–gram. Graphical display of $f(t)$ is also useful in detecting the presence of interfering arrivals. Signal clipping can be identified by a characteristic scalloped shape of the instantaneous amplitude $a(t)$. For noisy data, these useful diagnostic properties of $f(t)$ and $a(t)$ confer an advantage on the Q–gram method over the spectral ratio method.

The Q–gram method was applied to horizontal component OBS data collected over soft sediments in the northwest Pacific. The Q-gram method gave an estimate of $Q_\beta \approx 75 \pm 15$, taking into account apparent interference at the trailing end of the later arrival. The spectral ratio Q_β estimate for the OBS data, using the smaller windows that exclude the apparent interference, agrees well with the Q–gram result.

3.6 REFERENCES

Bath, M., 1974. Spectral analysis in geophysics, *in* Bath, M. (ed.), *Developments in Solid Earth Geophysics*, Vol. **7**, Elsevier Science Publishing Co.

Bromirski, P. D., L. N. Frazer, and F. K. Duennebier, 1992a. Sediment shear Q from airgun OBS data, *Geophys. J. Int.*, **110**, 465–485.

Bromirski, P. D., L. N. Frazer, and F. K. Duennebier, 1992b. Sediment shear Q from pulse width measurements: Estimating the pulse width constant, *EOS, Trans., Am. Geophys. Un.*, **73**, 593, abs.

Bromirski, P. D., L. N. Frazer, and F. K. Duennebier, 1993. Q from pulse width of dispersed arrivals, *63rd Ann. Internat. Mtg., Soc. Expl. Geophys., Expanded Abstracts*, 646–648.

Duennebier, F. K., B. Lienert, R. Cessaro, P. Anderson, and S. Mallick, 1987. Controlled–source seismic experiment at Hole 581–C, *in* Duennebier, F.K., Stephen, R., Gettrust, J.F., et al. (eds.), *Init. Repts. DSDP,* **88**, 105–125, Washington (U.S. Govt. Printing Office).

Engelhard, L., D. Doan, G. Dohr, P. Drews, T. Gross, F. Neupert, J. Sattlegger, and U. Schonfeld, 1986. Determination of the attenuation of seismic waves from actual field data, as well as considerations to fundamental questions from model and laboratory measurements, *DGMK Report* **254**, 83–119.

Gladwin, M. T. and F. D. Stacey, 1974. Anenelastic degradation of acoustic pulses in rock, *Physics of the Earth and Planetary Interiors,* **8**, 332–336.

Jannsen, D., J. Voss and F. Theilen, 1985. Comparison of methods to determine Q in shallow marine sediments from vertical reflection seismograms, *Geophys. Prosp.*, **33**, 479–497.

Kanasewich, E. R., 1981. *Time Sequence Analysis in Geophysics*, University of Alberta Press, Edmonton, Alberta, Canada.

Kjartansson, E., 1979. Constant Q-wave propagation and attenuation, *J. Geophys. Res.,* **84**, 4737-4748.

Mallick, S. and L. N. Frazer, 1987. Practical aspects of reflectivity modeling, *Geophysics,* **52**, 1355-1364.

Taner, M. T., F. Koehler and R. E. Sheriff, 1979. Complex trace analysis, *Geophysics*, **44**, 1041–1063.

Tonn, R., 1991. The determination of seismic quality factor Q from VSP data: A comparison of different computational methods, *Geophys. Prospect.*, **39**, 1–27.